University of Nottingham
UK | CHINA | MALAYSIA

Development and control of vortices over a very low aspect-ratio wing

Thesis submitted to the University of Nottingham for the degree of
Doctor of Philosophy, October 2022.

Lei Dong

4316754

Supervised by

Prof Kwing-So Choi
Dr Yaxing Wang
Dr Xuerui Mao

Signature ________________

Date _____ / _____ / _____

Abstract

The vortical structures over a thin rectangular wing with a very low aspect ratio (AR) of 0.277 are investigated in a wind tunnel at an effective Reynolds number of 3×10^6. The maximum lift of this thin wing is found at an angle of attack of 42°. The flow separates at the leading-edge and reattaches to the wing surface, forming a strong leading-edge vortex (LEV) which plays an important role on the total lift. The results show that the induced velocity of the tip vortex (TV) increases with the angle of attack, which helps reattach the separated flow and maintains the LEV. Turbulent mixing indicated by the high Reynolds stress can be observed near the leading-edge due to an intense interaction between the LEV and the TV. The reattachment point of the LEV moves upstream closer to the wing tip, however.

When applying pitch-up motion, with pivots at mid-chord, the maximum lift angle is increased with an increase in the pitch rate, but the maximum lift coefficient is slightly reduced. The pitching motion also causes delay in the vortical development over the wing, which is increased with an increase in the pitch rate. The delay in the LEV development due to the pitching motion is nearly identical to that in the TV development, indicating that the dynamics of the LEV is strongly influenced by the TV, which is confirmed by particle image velocimetry measurements.

Flow control of the tip vortices over a very low aspect-ratio wing is carried out using the dielectric-barrier-discharge plasma actuators. The results indicate a large change in the aerodynamic forces by plasma flow control, where the lift coefficient is increased by the blowing plasma actuator by 23%, and is reduced by the suction plasma actuator by 30%. The change of the drag coefficient is less than 10%. The blowing plasma moves the tip vortex outboard away from the wing tip, increasing the streamwise vorticity as well as the turbulence intensities and the Reynolds stress. With the suction plasma, the tip vortex is shifted inboard closer to the wing tip. Co-flowing with the tip vortex, the blowing plasma increases the tip vortex circulation, while it is reduced by the counter-flowing suction plasma.

List of Publications

Journal articles:

Dong, L., Choi, K-S. and Mao, X. R. (2020). Interplay of the leading-edge vortex and the tip vortex of a low-aspect-ratio thin wing. *Exp. Fluids*, 61(9):1-15.

Dong, L., Choi, K-S., Mao, X. R. and Wang, Y. X. (2022). Development and interaction of vortices over a very low aspect-ratio wing under pitch-up motion. *J. Fluid Mech.*, 943, A42.

Dong, L., Choi, K-S., and Wang, Y. X. Plasma flow control of the tip vortices over a very low aspect-ratio wing. *Phys. Fluids*, 34, 087101.

Dong, L., Choi, K-S., and Wang, Y. X. Leapfrogging formation using the dielectric barrier discharge plasma actuator. *Phys. Fluids.* (under preparation)

Proceedings:

Dong, L., Choi, K-S. and Mao, X. R. (2019). Vortical structures over a stationary low AR wing. *Proceedings of UKFN Joint SIG Meeting*, Cambridge, UK.

Dong, L., Choi, K-S. and Mao, X. R. (2020). Vortical structures over a pitching low AR wing. *Proceedings of UKFN Joint SIG Meeting*, London, UK.

Dong, L., Choi, K-S. and Wang, Y. X. (2022). Plasma flow control of the tip vortices over a very low aspect-ratio wing. *Proceedings of EDRFCM Meeting*, Paris, France.

Acknowledgements

I would like to express my deepest appreciation to my supervisors Prof. Kwing-So Choi, Dr. Xuerui Mao and Dr. Yaxing Wang, for their guidance and support. A special thanks must go to Prof. Kwing-So Choi not only for his academic advice and encouragement during my Ph.D. studies, but also for his patience and assistance in my personal life. Also, thanks must extend to the China Scholarship Council, which funded my studies at the University of Nottingham. This research project has also received funding from the Clean Sky 2 Joint Undertaking (JU) under grant agreement number 864290.

My sincere thanks also go to Dr. Jung-Hoon Kim, Dr. Guanghui Ding, Dr. Qiangqiang Sun and Sikai Geng for their useful suggestions and discussions.

Thanks are given to Prof. Lihao Feng and Dr. Zhenyao Li for their help during my visit to Beihang University.

I would especially like to thank Wenjing for her support and patience in my Ph.D. study, and to my family. I dedicate this thesis to all of them.

Contents

List of Tables

List of Figures

Nomenclature

Acronyms

2D Two dimensional

3D Three dimensional

AoA Angle of attack

AR Aspect ratio

DBD Dielectric barrier discharge

LEV Leading edge vortex

MAV Micro air vehicle

PIV Particle image velocimetry

SDBD Surface dielectric barrier discharge

SL Separation length

TEV Trailing edge vortex

TV Tip vortex

VI Virtual instrument

Symbols

A Surface area

c Chord length

C_μ Momentum coefficient

C_A, C_N Axial and normal force coefficients

C_L, C_D Lift and drag force coefficients

C_{Lmax} Maximum lift coefficient

C_{Lp}, C_{Dp} Lift and drag force coefficients with plasma control

D TV diameter

D_e Shift distance uncertainty

D_s Shift distance of particles

E_{pp} Peak-to-peak value of voltage

f Modulation frequency

f^+ Non-dimensional modulation frequency

F_A, F_N Axial and normal forces

F_L, F_D Lift and drag forces

K Non-dimensional pitch rate, $\frac{\dot{\alpha}c}{2U_\infty}$

M Momentum flux

r_c Radius of vortex core

Re Reynolds number

Re_p Reynolds number based on the thickness of the plasma actuator

s Half span length

S_{TV} TV area

t Time

T_e Interval time uncertainty

T_i Interval time of image pairs

U, V, W Laboratory-based velocities

u, v, w Laboratory-based velocity fluctuations

U_∞ Freestream velocity

U_e Velocity uncertainty

U_m, V_m, W_m Wing-based velocities

V_d Downwash velocity

V_{davg} Averaged downwash

x, y, z Laboratory-based coordinates

x_m, y_m, z_m Wing-based coordinates

x_p Pitching pivot

y_c Distance from vortex centroid to wing surface

z_c Distance from vortex centroid to mid-span

Greek symbols

α Angle of attack

α^* Angle of attack removing the phase lag

α_r Angle of attack in radian

α_{Lmax} Maximum lift angle

α_{max}	Maximum pitch angle
β	Phase lag
$\dot{\alpha}$	Angular velocity
Γ_L	LEV circulation
Γ_T	TV circulation
Ω	Vorticity flux
ω_x	Streamwise vorticity
ω_z	Spanwise vorticity
ρ	Air density
σ	Smoothing parameter; standard deviation
τ	Non-dimensional convective time

Chapter 1

Introduction

1.1 Aim and objectives

Many efforts have been spent on the investigation of the aerodynamics of the carefully designed aerofoils to find out the optimised body shape, whose flow separation angle is postponed and the lift-to-drag ratio is improved. The aerofoil in research is treated as one which has the same flow field along the span, e.g,. two-dimensional flow. The aerodynamic results of the various aerofoils give us a better understanding of the flow separation and its associated adverse impact. Specifically, flow separation makes a sudden reduction in the lift and an increase in the pressure drag, which could result in losing control.

The flow structures around the aeroplane, however, are quite different from that over the aerofoil. A number of vortices can be generated during the flight and the interaction between those vortices makes the situation much more complicated. One of the most significant vortices is formed at the wing tip, known as the tip vortex (TV). The formation of the TV is generally attributed to the pressure difference between two sides of the wing, which accelerates the flow to wrap around the wing tip (Green, 1995). The TV initiates at the tip of the leading edge and grows in size and strength along the chord, which can be found even several hundred chords downstream. The large circulation generated by the TV may cause potential safety problems for other aircraft. This promotes scholars and engineers to obtain an accurate understanding of the TV either in the very early wake (less than 2 chords from the trailing edge of the wing) or far-field (several hundred chords away from the trailing edge). The TV can induce low pressure on the suction side of the wing, which in turn improves the lift coefficient, called the vortex lift (Mueller and DeLaurier, 2003). The performance of the vortex lift has been exhibited on the delta wing. Application of the unmanned aerial vehicles (UAV) has been developed recently to meet some special missions, which usually owe a low aspect ratio (AR), having strong three-dimensional (3D) features. As the angle of attack (AoA) increases, the flow separates at the leading edge, trailing edge and tip edge of the wing, interacting with each other (Taira and Colonius, 2009).

Considering the amazing aerodynamics and manoeuvrability of natural creatures, like birds and insects, mimicking the flying pattern of these animals is one of the effective ways to improve the performance of the wing. Three kinds of kinematic motions, pitching, plunging and sweeping motions, can be applied on the wing separately or jointly to simulate an unsteady wing. A large leading-edge vortical structure is observed on a pitching aerofoil, which is responsible for an enhanced lift coefficient (Ellington et al., 1996). Downstream convection of this leading-edge vortex (LEV), however, causes only a transient boost on the lift. To maintain the LEV over the wing and enjoy its benefit, the additional sweeping motion must be combined together with the pitching motion. It is observed that the

TV can keep the LEV on the suction side of the wing during the unsteady motion.

Flow control can be used to modify the flow structures to achieve the desired influence. In the past two decades, plasma aerodynamics using the dielectric-barrier-discharge (DBD) has received much more attention due to its technological advancements that allow the ionised air jet to be generated in the wall boundary layer with quick responses. The construction of the plasma actuator is extremely simple, which is usually composed of two electrodes separated by a dielectric sheet. There are many advantages of the plasma actuator: it can be placed onto the model surface to avoid drag penalty due to the protrusion of the controller, covers a wide bandwidth to dozens kHz and consumes low power less than 100 W. Generated plasma jet can be used to either form longitudinal vortices or modify existing flow fields. The effectiveness of plasma control has been investigated and demonstrated on numerous objectives, including delaying stall, enhancing load performance, mitigating shock waves, delaying or promoting laminar-to-turbulent transition, etc (Moreau, 2007; Corke et al., 2010).

Due to the influence of the TV on the vortical structures, the aerodynamics of a very low AR wing is significantly different from the large AR or 2D wings. In this thesis, the characteristics of a very low AR wing, therefore, are carefully investigated to obtain an understanding of its aerodynamics. The influence of the pitching motion on the vortical structures (LEV and TV) of this very low AR wing is also studied. The aerodynamics of a very low AR pitching wing and conventional pitching wings are compared to point out their different performance. Furthermore, plasma actuators are used to alter the flow over the thin wing to discover benefits to the wing aerodynamics as outlined above. The results of this research are expected to have guidance on designing the aircraft with a very high stall angle, improving the lift coefficient of the low AR wing at small AoAs, avoiding the hazards of the wind gust on the vehicles and controlling vortices, such as the TV control on the finite-span wing and LEV control on the delta wing.

1.2 Outline of the thesis

The remainder of this thesis is organised as follows:

In Chapter 2, the knowledge of the wing and the plasma actuator is reviewed. Aerodynamic differences between a conventional aerofoil and a finite-span wing are introduced, especially the importance of the TV. Following that, the investigations of improving the wing performance, like applying unsteady motion and flow control, are covered.

In Chapter 3, the experimental arrangement is introduced, including the design of a low AR wing model, conduction of aerodynamic force measurements, applying smoothed pitching kinematic, three-components velocity measurements and generation of the plasma jet. Some relevant techniques, like vortex identification, are also described.

In Chapter 4, the aerodynamics and quasi-3D vortical structures of a stationary very low AR wing are investigated over a wide range of AoAs. The reattachment of leading-edge-separated flow is obtained at a large AoA under the influence of the TV, forming a large separation bubble. Characteristics of the LEV and TV are presented according to compute their circulation, vortex centroid, etc. The interplay between these two vortices is also studied.

In Chapter 5, the investigation is focused on the unsteady wing which is applied with the pitch motion. The influence of the pitching motion on aerodynamics and vortex developments is studied at different pitch rates with an increase in the AoA. Phase lags of the TV and the LEV between the pitching and baseline cases are pointed out. The impact of the TV on the behaviour of the LEV is discussed.

In Chapter 6, two types of plasma actuators are bonded on the wing to control the TV. Obvious changes in lift and drag forces of the wing are observed at the small AoAs. The influence of plasma actuators on the TV is examined by considering its shape, strength and locus. The underlying mechanism for the plasma control on the TV is explained in detail based on the vorticity field and vorticity flux.

In Chapter 7, the conclusions of this thesis are given.

Chapter 2

Literature review

2.1 Introduction

This chapter summarises some of the research on infinite-span, finite-span and unsteady wings, as well as plasma flow control, which is relevant to our current study. The cited papers are meant to provide a foundational grasp of some of the key problems and mechanisms. Further references can be found within the cited paper for a deeper understanding. A significant aerodynamic problem, namely the flow separation, of an aerofoil is highlighted in Sec. 2.2, followed by the introduction of the finite-span wing in Sec. 2.3, where the reason for differing aerodynamics between the infinite- and finite-span wings is explained and the importance of the TV is reviewed. Biological-inspired methods, notably the pitching wing, for improving the lift coefficient are given in Sec. 2.4. The last section introduces a revolutionary active flow control using the plasma actuator. We concentrate on the surface dielectric barrier discharge (SDBD) plasma actuator and its application on the wing due to its relevance to our work.

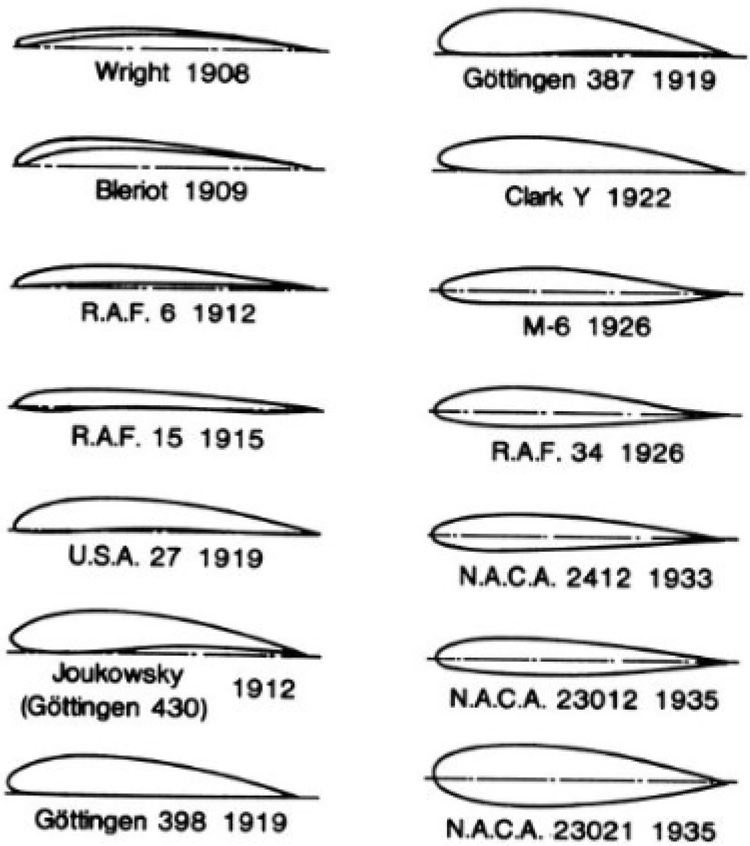

Figure 2.1: Evolution of the aerofoil in early times 1908 - 1935 (Eppler, 1990).

2.2 Aerofoil aerodynamics

The first research of an aerofoil is considered to be conducted by Wright brothers who found that a lift force can be generated in the opposite direction to the weight of the aeroplane. Aerodynamicists later recognised the importance of aerofoil shape, such as the camber and thickness, on the load performance, which promoted the optimisation of the aerofoil. Figure 2.1 shows the historic evolution of the aerofoil in early times. The generation of the lift force is due to the turning of the flow around the wing body. Changed flow direction and velocity magnitude can produce a net force on the wing.

Over the last 100 years, numerous investigations have been conducted on

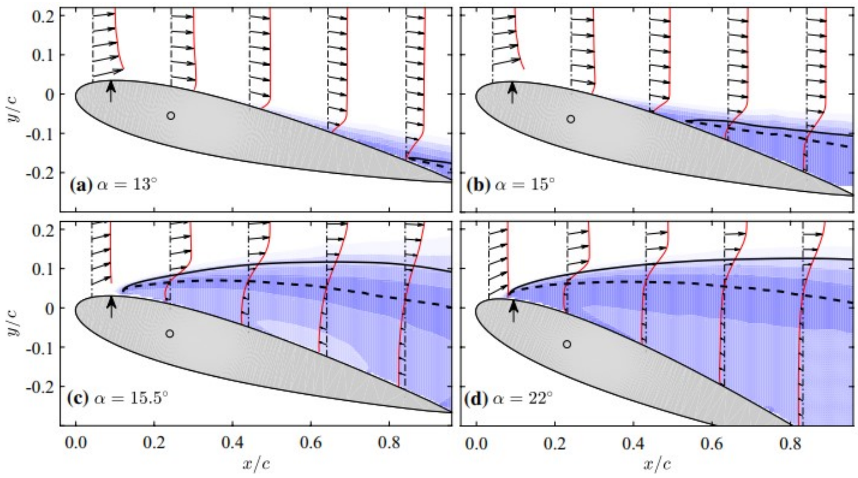

Figure 2.2: Flow fields of the NACA 0015 aerofoil at different AoAs (Zong et al., 2018).

aerofoils to obtain a better understanding of their aerodynamics. It is well known that the lift coefficient of the aerofoil is profoundly dependent upon the AoA. Figure 2.2 depicts the development of the flow field over a NACA 0015 aerofoil with an increase in the AoA. The flow at small AoAs attaches to the wing surface and the separation point is observed in the vicinity of the trailing edge, where the lift coefficient increases linearly at a slope of approximately 2π as a function of the AoA based on the linear thin aerofoil theory for incompressible potential flow. Thereafter, the lift gradually reaches a peak value at a certain AoA depending on the aerofoil design. This critical angle is called stall angle, followed by a rapid drop of the lift which is caused by flow separation. Separation is a process of breakdown or detachment of the shear layer, accompanied by thickening of the wake region and a significant increase in the wall-normal velocity to interact with the freestream (Simpson, 1989; Greenblatt and Wygnanski, 2000). This results in the collapse of the lift force and an increase in the drag force.

The formation of flow separation bubble over the aerofoil has attracted many researchers' attention. Classical laminar separation bubble (LSB) theory was proposed by Gaster (1967) who investigated the influence of the LSB on the pressure gradient. He observed that the pressure on the suction side was increased and the constant pressure region was extended by the LSB. The formation of the LSB over the wing leads to an aberration of the streamlined shape of the aerofoil, which subsequently impacts the stability and performance of the aerofoil. It is, therefore, essential to comprehensively understand the underlying physical mechanism for the LSB formation in order to mitigate its influence.

It has been shown that the process of laminar-to-turbulent transition of the shear layer accounts for the reattachment of leading-edge separated flow (Marxen et al., 2003; Jones et al., 2010). Small perturbations originating from the environmental flow enter into the separated shear layer via a receptivity process (Saric et al., 2002), which are amplified exponentially in the early stage of transition (Tollmien-Schlichting waves). Due to the rapid growth of perturbation, the nonlinear interactions occur in the separated region, producing periodic shedding of coherent vortical structures (Hosseinverdi and Fasel, 2019). High momentum transported by these structures to the aerofoil surface suppresses the flow separation and enables the flow reattachment. Given the importance of the perturbation from the freestream on the separated shear layer transition, turbulence intensity of freestream becomes one of the key parameters for the formation of the LSB, which has been specifically studied (Olson et al., 2013; Simoni et al., 2017; Istvan and Yarusevych, 2018; Hosseinverdi and Fasel, 2019). Their results presented that the length of the LSB was decreased with increasing the turbulence intensity. The controversy here is that the shortening of the LSB could be attributed to the rearward movement of the separation point or forward movement of the reattachment point. The influence of other important parameters, such as local pressure gradient and boundary

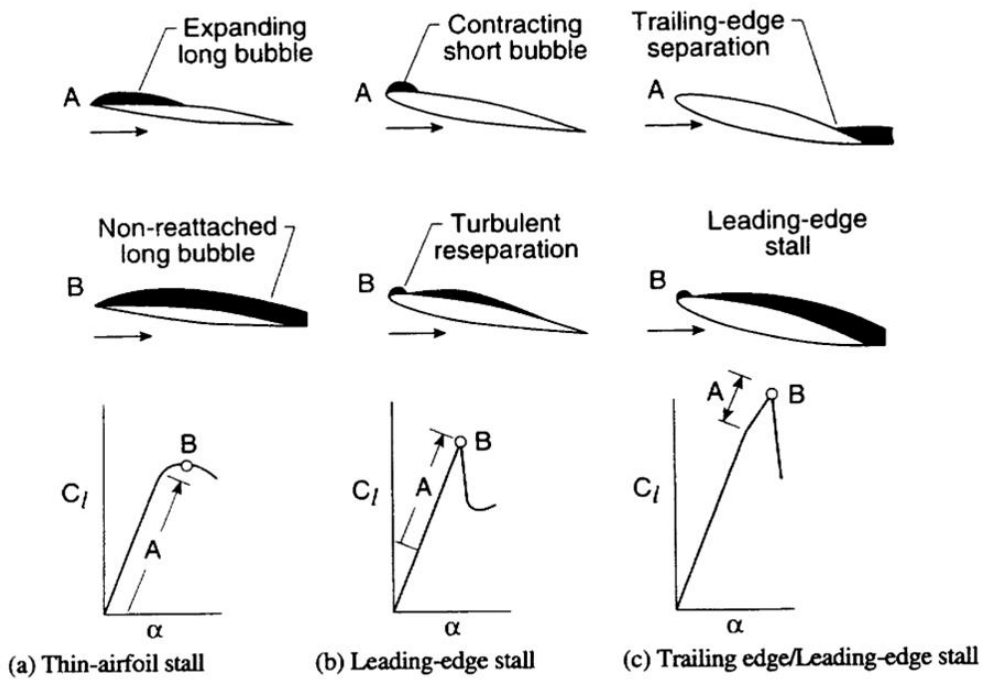

Figure 2.3: Classification of the flow separation over an aerofoil (Gault, 1957).

layer displacement thickness, on the transition can be found in Boiko et al. (2011).

Gault (1957) classified three types of flow separation over an aerofoil, as shown in Fig. 2.3. Thin-aerofoil stall illustrated in Fig. 2.3a is observed on an aerofoil with a sharp leading edge, where the flow separates at the leading edge surface, forming a separation bubble. As the AoA increases, the laminar separation bubble extends towards the trailing edge, leading to a gentle stall indicated by a slow decrease of the lift after the stall angle.

The second type of flow separation is called the leading-edge stall, as shown in Fig. 2.3b. A small LSB is observed in the vicinity of the leading edge, which has the same formation mechanism as the LSB observed from the thin-aerofoil stall case. The flow, however, separates again downstream the turbulent reattachment point at the stall angle, associated with a collapse of lift coefficient. Here, the term "flow reseparation" is used to represent this type of stall for convenience. There are two proposed mechanisms for the formation of flow reseparation. One is that the shear layer after the transition is still not strong enough to eliminate the flow separation, leading to a bursting of the LSB (Owen and Klanfer, 1953; Gaster, 1967). The other explanation considers the separation of the turbulent shear layer after the reattachment point (Van den Berg, 1981).

Yet another stall behaviour can be observed on a streamlined aerofoil, where the flow is able to attach to the wing surface at small AoAs. Increasing the AoA makes the detachment of the flow starting from the trailing edge while the attachment of the flow close to the leading edge is maintained, see Fig. 2.3c. It is noted that the flow separation at the trailing edge does not lead to the decrease of the lift immediately (Polhamus, 1996). In fact, an aerofoil with the third type stall can obtain a higher lift as compared to that of thin-aerofoil stall and leading-edge stall. As the AoA is further increased, the adverse pressure gradient is sufficient to detach the turbulent shear layer. Then the drop of the lift is about to come.

2.3 Finite-span wings

Investigations of an aerofoil in a two-dimensional flow field give us a comprehensive understanding of physical mechanisms for lift generation and flow separation, which are fundamental to design and improve the flight capability. The flow on a finite-span wing, however, not only detaches at the leading edge but at the tip edge. These edge separations generally accompany the formation of vortices. The interaction of these vortices influences the flow field over the rest of the wing body, creating a 3D, complex wake region. An accurate understanding of the flow structure around the

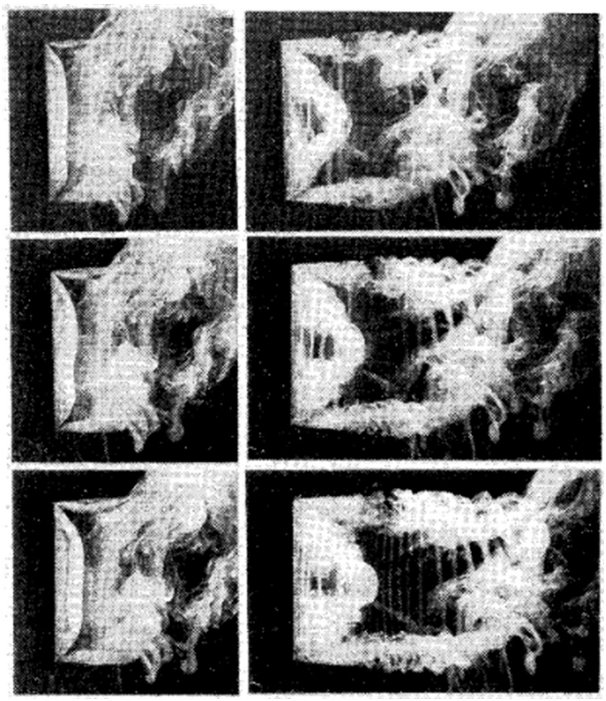

Figure 2.4: A sequence of flow fields for a rectangle wing at AR = 2 (Freymuth et al., 1987).

wing is essential before proposing an optimised geometry of the wing.

Flow separation over a finite-span wing was visualised using oil and smoke (Winkelman and Barlow, 1980; Freymuth et al., 1987), as shown in Fig. 2.4. At a moderate AoA, the flow separates at the leading and tip edges of the wing, forming a LEV along the span and a pair of TVs along the chord. In the early time, both LEV and TV are relatively small. With time, the LEV turns into an Ω-shaped structure along the span. The leading-edge flow anchors at the tip corner but leaves off the wing surface close to the mid-span, which is ascribed to be the influence of the TV. This 3D vortical structure produces a distinct lift curve for the finite-span wing, revealed by Pelletier and Mueller (2000) in Fig. 2.5. It is observed that the lift-curve slope of a finite-span flat plate is reduced while the stall angle is delayed as compared to that of a 2D plate. It is plausible to deduce that the formation of the TV should be responsible for these results since the fundamental difference between 2D and finite-span wings is whether the

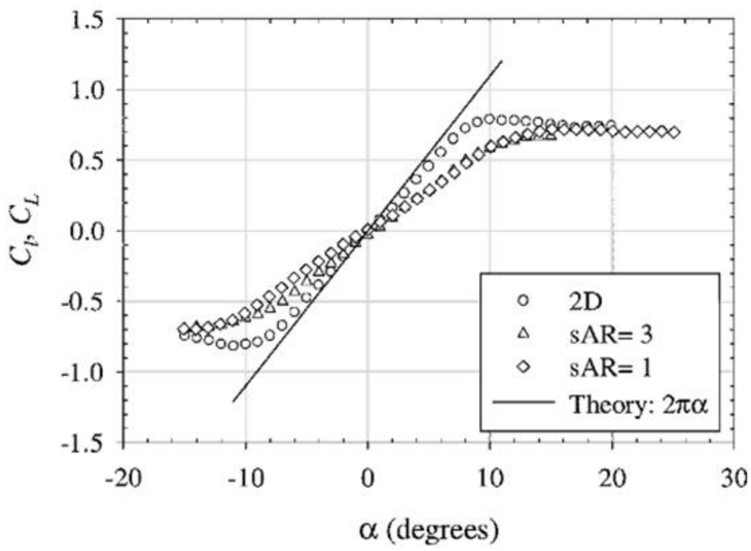

Figure 2.5: Comparison of the lift coefficient of infinite- and finite-span flat plates (Pelletier and Mueller, 2000), where sAR indicates the semi-span aspect ratio.

tip effect is included.

Before looking into the influence of the TV, the origin of the TV needs to be explored. Three different explanations were outlined by Green (1995). His explanation is attributed to the pressure unbalance between two sides of the wing. When the lift is generated, the pressure on the upper surface is much lower than that of the lower surface. The flow at the pressure surface close to the wing tip is pulled outboard and warps up towards the suction surface, forming a rotating flow as so-called the TV. Another explanation considers the velocity distribution around the wing tip. It is expected that the fluid outboard of the tip edge has the same velocity vector as the freestream while the inboard fluid has a different direction due to the existence of the wing body. Non-parallel movement of these fluids produces the vorticity orientation. The final mechanism is based on Helmholtz vortex law. In order to maintain the net circulation to zero, a starting vortex must shed from the wing when the wing impulsively starts (Kutta-Joukowski Law). However, vortex lines of the bound vortex and starting vortex can never terminate in fluid, two additional vortices must be formed to connect them to form a close vortex loop, see Fig. 2.4. The TV, therefore, is generated.

Considering the importance of the tip effect, Torres and Mueller (2004) measured the aerodynamic forces of the finite-span flat plate with various ARs ranging from AR = 0.5 to 2. Their lift curves are quite different from that of the 2D aerofoil, particularly at low ARs (AR < 1.25), whose slope can be estimated by $2\pi/(1+2/e\mathrm{AR})$, where e is Oswald efficiency number depending on the wing shape. They also noticed that the peak lift and stall angle of the wing were increased with a decrease in the AR, which was believed to be due to the formation of the TVs. Further investigations were conducted by Taira and Colonius (2009) who numerically studied the vortical structures and corresponding aerodynamic forces of different AR wings at a Reynolds number of $Re = 300$. Depending on the AR and AoA, three different wake profiles are found, as shown in Fig. 2.6. In early times, similar flow fields are observed for different AR cases, consisting of a LEV, two counter-rotating TVs and a starting vortex. With time, the TVs for the wing with AR = 1 occupy the entire span of the wing while the LEV attaches to the wing surface, reaching a steady state. At a moderate AR (AR = 2), the TVs are not strong enough to maintain the attachment of the LEV on the wing surface, which in turn sheds downstream and interacts with the TV. Nonlinear interaction between the TV and the shedding LEV eventually leads to an unsteady aperiodic wake. On a large AR wing (AR = 4), the TV is rather weaker than the LEV, suggesting a limited influence of the TV on the LEV. As a result, the LEV is being shed downstream periodically. Distinct wake types of the wing should be the reason for the different lift curves observed by Torres and Mueller (2004).

By correlating the forces with the vortical structures along the wing span,

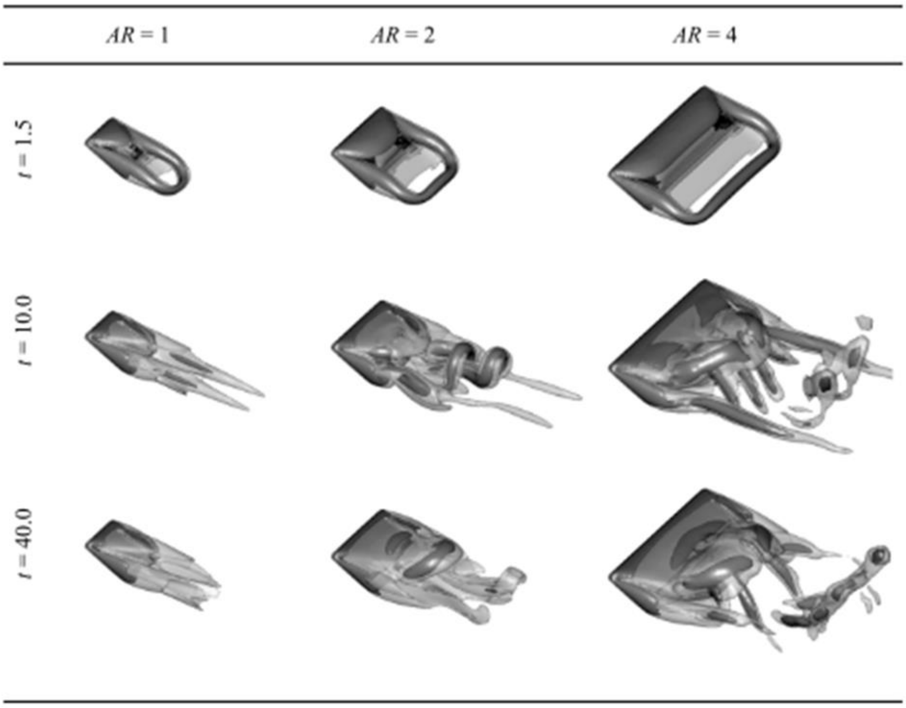

Figure 2.6: Vortical structures over flat plate wings of AR = 1, 2 and 4 at an AoA of 30° at $Re = 300$ (Taira and Colonius, 2009).

Zhang et al. (2020) investigated the tip effects on the wing aerodynamics. Close to the mid-span, the sectional lift force exhibits considerable fluctuations due to the shedding of the LEV. Moving to the tip edge, the flow is maintained to attach to the wing surface and there is no leading-edge flow roll-up, resulting in a relatively steady lift force. This suggests that the TV can stabilise the unsteady LEV shedding. Noteworthy is that the maximum sectional lift force is seen close to the wing tip, which probably is owing to the attachment of the flow. DeVoria and Mohseni (2017a) explored the reason why the high-incidence lift was achieved on a low AR wing. Their force results indicated that the maximum lift force was increased approximately two times while the stall angle was postponed nearly three times with a decrease in AR from 2.5 to 0.75, which was ascribed to the reattachment of the separated leading-edge flow on a low AR wing. Flow reattachment reduces the amount of the vorticity shedding downstream, which in turn strengthens the bound vortex, resulting in the large lift generation on a low

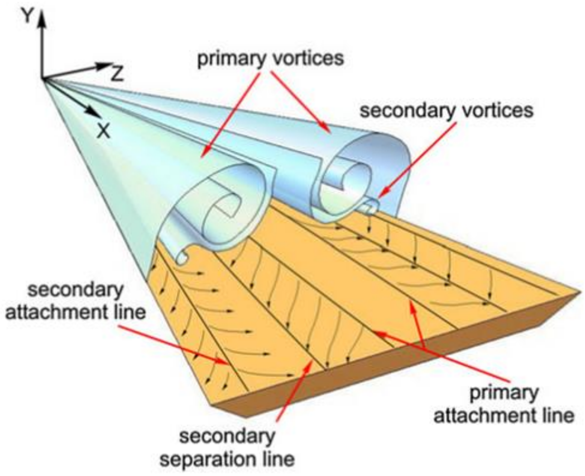

Figure 2.7: Vortices on the delta wing at a large AoA (Sidorenko et al., 2013).

AR wing. The flow reattachment is due to the existence of the TVs, which induce wall-ward downwash to help reattach the separated flow. These researches demonstrate the importance of the TV, which must be taken into account to obtain the accurate aerodynamics of the wing.

The behaviour of the LEV on the delta wing is comparable to the TV formed on the low AR wing. Further information on the TV can be provided by the investigations of the delta wing. For the sake of clarity, the term TV is used here to indicate the LEV on the delta wing. One of the key advantages of the delta wing, which is served for fighter and supersonic civil transport, is its high manoeuvrability (Gursul, 2004). This is due to the formation of two counter-rotating vortices over the lifting surface at large AoAs, see Fig 2.7. Formed vortices can produce the vortex lift, which can reach or even exceed half of the total lift, to improve the performance of the delta wing (Polhamus, 1966). Figure 2.8 shows the contribution of the vortex lift on the delta wing at various ARs. At large AoAs, where the TVs are formed, the lift of the wing is dramatically enhanced by the vortex suction. For example, the lift coefficient of the wing with an AR of 2 and a sweep angle of 60° at the AoA of 25° is approximately 0.75 based on the

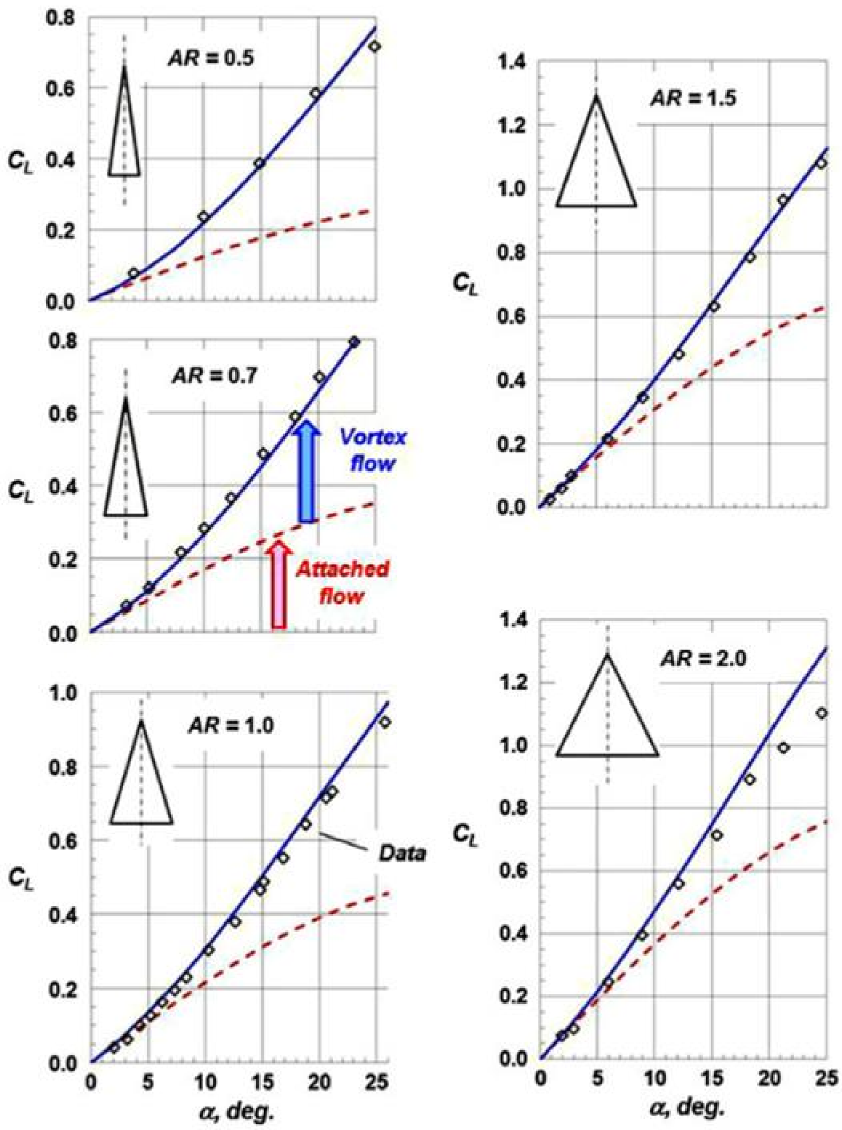

Figure 2.8: Vortex lift of the delta wing at different ARs as a function of AoA (Polhamus, 1966).

lift theory but the real lift coefficient is 1.1 under the influence of the TVs. It is also observed that decreasing the AR makes the vortex suction much more dominant.

In addition to the advantages of the TV, such as helping reattachment and generating vortex lift, many investigations have also been conducted to understand the evolution and characteristics of the TV itself. Unsteadiness of the TV is found even at a small AoA, where the TV is quite compact and grows downstream along the wing tip. Menke and Gursul (1997) pointed out the strong velocity fluctuations inside the vortex core and the maximum turbulence intensity around the vortex centroid. This is due to the random displacement of the TV core, so-called vortex wandering (Corsiglia et al., 1973), whose mechanism has long been debated. Bailey and Tavoularis (2008) studied the influence of the freestream turbulence on the vortex wandering. They found that the decay of the peak circumferential velocity of the vortex core was increased with freestream turbulence intensity, which possibly explains the increasing amplitude of the vortex wandering. However, Jacquin et al. (2001) revealed that the vortex wandering should be independent of the residual perturbation, which is more related to the propagation of unsteadiness with the evolution of the TV. The mechanism of the vortex wandering still remains elusive, which requires more studies to obtain a better understanding.

Another intriguing phenomenon of the TV is the vortex breakdown, which is generally observed at large AoAs and can be classified into two types, namely bubble type and spiral type (Lambourne and Bryer, 1961). The occurrence of the vortex breakdown has adverse impacts on the aerodynamics of the wing, such as reducing the lift force and the generation of the pitching moment. There are several mechanisms for the vortex breakdown, which can be divided into three categories: flow stagnation (like flow separation of the 2D boundary layer), wave propagation and hydrodynamic instability (Gursul, 2004). To obtain the critical parameters for the vortex breakdown, a wide range of experimental and computational research has been carried out (Billant et al., 1998; Gursul et al., 2005; Mitchell and Délery, 2001; Agrawal et al., 1992; Mary, 2003). It is generally believed that the swirl level and pressure gradient outside the vortex core are two important factors for the vortex breakdown. By increasing either parameter, the vortex breakdown takes place earlier.

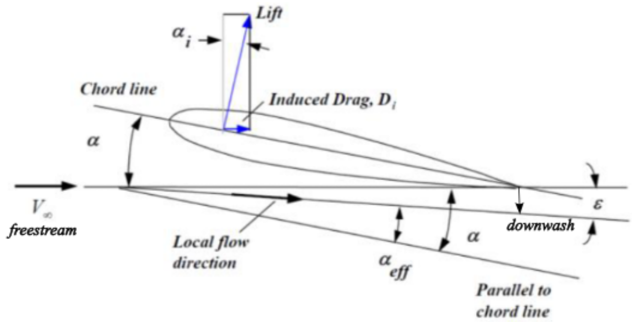

Figure 2.9: Sketch of the induced drag (Nabhan, 2018).

Despite its benefits, the TV has some negative consequences. One of the important drawbacks of the TV is the induced drag (also known as the lift-dependent drag), as illustrated in Fig. 2.9. The downwash is induced by the TV from the inboard region of the wing, which deflects the direction of the freestream, indicated by ϵ in Fig. 2.9. As a result, the effective AoA of the wing is reduced, resulting in a smaller lift coefficient. Compensation of the reduction in the lift can be achieved by increasing the AoA. But the tilted lift vector can generate a force component in the drag direction, which greatly reduces the aerodynamic efficiency. Henderson and Holmes (1989) and Anderson Jr (2010) indicated that the induced drag of the wing can account for almost 50% and 25% of total drag in the high lift and cruise configurations, respectively.

Once the TV is formed over the wing, it develops far downstream and dominates the flow structures after the trailing edge. Based on the characteristics of the TV, the region downstream the trailing edge can be categorised into three types: near field ($0 \sim 10$ chords), mid-field ($10 \sim 2000$ chords) and far-field (> 2000 chords) (Giuni, 2013). In the near field, a complicated vortex interaction can be observed, where the TV mixes with the trailing-edge vortices. Thereafter, the TV begins to decay at a slow rate in the mid-field and eventually goes through the breakdown in the far-field, accompanied by a rapid fall in circulation. The TV generated by a leading aircraft can exist several hundred chords downstream of the trailing edge, causing a considerable influence on a trailing aircraft. Encountering the TVs leads to a collapse in the lift, as well as the generation of a pitching moment. There have been over 100 serious accidents as a result of these encounters (Chigier, 1974). To avoid the wake hazard, the distance between the aeroplanes is essential, especially during take-off and landing.

2.4 Unsteady wings

Birds and insects can respond quickly to adapt to the sudden change in the surrounding environment, such as wind gusts, predators and so on. Their flight abilities have attracted many biologists and engineers to explore the underlying physical mechanism. The instantaneous lift of a locust flying in a wind tunnel was measured directly by Cloupeau et al. (1979). The lift coefficient of the locust is twice that being deduced from the conventional lift theory. This suggests that the aerodynamics of the wing can be enhanced dramatically by applying certain kinematics to the wing. In order to grasp how the large lift coefficient is generated by the flying animals, Ellington et al. (1996) visualised the flow field around Manduca (a moth) undergoing the downstroke motion. They observed the reattachment of the leading-edge separated flow, forming a large LEV. Due to the low pressure of the LEV, the total lift is increased, which is equivalent to increasing the circulation around the wing. The generation of large-scale vortices around the wing has been widely recognised as the fundamental reason for the amazing aerodynamic performance of the unsteady wing.

The simplified models for the insect flight are proposed, including three basic kinematics: pitching, sweeping and plunging (Wang, 2005). The pitching motion accompanies the continuous change of the geometric AoA while the other two motions are made at a fixed geometric AoA. Based on these kinematics, the motion applied on the wing includes pure pitching, pure sweeping, pure plunging, combined pitching and plunging, combined pitching and sweeping, combined plunging and sweeping, combined pitching, plunging and sweeping and so on. The influence of these motions on the aerodynamics of the wing has been extensively studied (Schreck and Hellin, 1994; Sunada et al., 2001; Ozen and Rockwell, 2012; Bross et al., 2013; Williams et al., 2015; Ramasamy et al., 2007; Gkiolas et al., 2018). Considering our present research, we mainly concentrate on investigations of the pure pitching wing in the following.

The pitching wing is generally defined as the wing pitching about the spanwise axis after Birnbaum (1924) proposed a novel idea of designing a propeller by applying the pitching motion on the wing. The objective of the pitching wing is to obtain a high lift coefficient and delay the stall angle. Granlund et al. (2013) studied the variation of the aerodynamics of a flat plate with the pitching motion, whose results indicated that both lift and stall angle were dramatically increased. However, the impact of the pitching motion on the aerodynamics of the wing is dependent on several key parameters, including the Reynolds number (Re), the pitch rate, the pitch pivot and the wing shape. Here, the non-dimensional pitch rate K is defined as $K = \dot{\alpha}c/2U_\infty$ (Triantafyllou et al., 2000), where $\dot{\alpha}$ is the angular velocity of the wing, c is the chord length and U_∞ is the freestream velocity.

2.4.1 Vortical structures

The flow field of a pitching aerofoil was investigated by Ohmi et al. (1991) in a water tank at $Re = 3000$ pivoting at the semi-chord, as shown in

Fig. 2.10, where convective time τ is given by $\tau = tU_\infty/c$. As the AoA (α) increases with time, the flow separates at the leading edge, followed by the formation of the shear layer vortex and the large-scale LEV. The LEV expands dramatically and its reattachment point eventually moves downstream of the trailing edge, showing the shedding of the LEV ($\tau >$ 3.0). Once the LEV convects away from the wing, the vortex lift from the LEV disappears, resulting in only a transient improvement of the total lift. The detachment of the LEV on a pitching aerofoil is generally explained by two main postulated mechanisms (Widmann and Tropea, 2015). The first one is the 'bluff body detachment mechanism' (Gerrard, 1966) referred to the interaction of the LEV and the trailing edge vortex (TEV) which can create an upstream boundary layer with opposite sign vorticity to the LEV. The other mechanism is the 'boundary layer eruption' (Doligalski et al., 1994) based on the boundary layer separation due to the adverse pressure gradient depending on the LEV strength.

Due to the importance of the LEV, the formation process of the LEV of a pitching aerofoil ($K = 0.05$) was studied by Deparday and Mulleners (2019). Applying the pitching motion, the flow is able to attach to the wing surface with a very thin shear layer thickness even at the stall angle of the static aerofoil. Thereafter, a separation point is observed in the vicinity of the trailing edge, where small-scale vortices with positive vorticity (opposite to the shear layer of the aerofoil) are obtained. The separation point, as well as these small-scale vortices, travel upstream towards the leading edge with an increase in the AoA. During this stage, the thickness of the shear layer exhibits an almost linear increase. When the separation point arrives at the leading edge, the shear layer starts to roll up and form a large-scale coherent LEV.

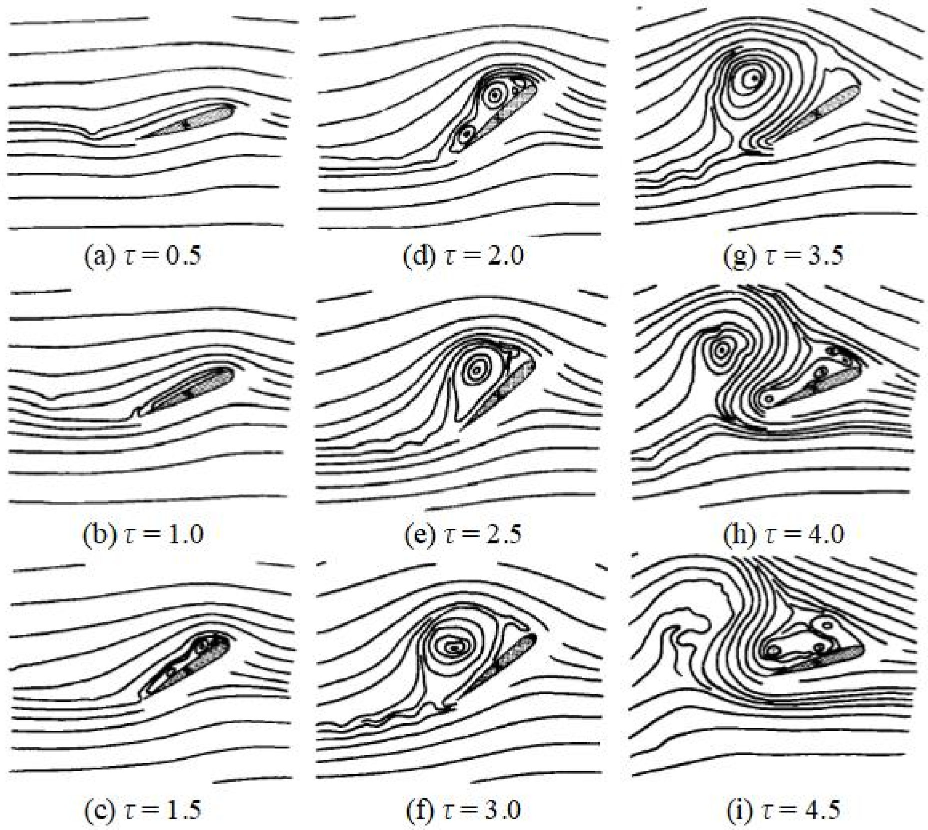

Figure 2.10: Streamlines of an aerofoil pitching up from $\alpha = 15°$ to $\alpha = 45°$ and then pitching down at a fixed pitch rate of $K = 0.63$ (Ohmi et al., 1991).

2.4.2 Effect of the Reynolds number

The range of the Reynolds number of the pitching wing being studied is concentrated between 10^2 and 10^7 (Wu et al., 2020). Ohmi et al. (1990) examined the vortex formation and wake establishment of a pitching aerofoil at three Reynolds numbers ($Re = 1500$, $Re = 3000$ and $Re = 10000$), whose results indicated little or no Re effect. However, increasing Re changes the duration of some phases of the flow and vortical development. Specifically, the wake development stage is accelerated while the transitional stage is shortened. Ol et al. (2008) compared the vorticity fields of a pitching wing at $Re = 300$, $Re = 600$ and $Re = 1200$. Generally, they obtained the same result as Ohmi et al. (1990): the fundamental progress of the vortex formation is independent of Re. But with increasing Re, the strength of the LEV is significantly enhanced and its attenuation with time becomes less, resulting in an intensive interaction between the LEV and the TEV at a high Re. The influence of Re ($Re = 23000$, 33000 and 48000) on the position of the reattachment point and the associated flow field on a pitching aerofoil ($K = 0.1$) was studied by Kim and Chang (2010). The reattachment point shifts upstream with Re, suggesting a small separation bubble at a high Re. Besides, there is the unsteady laminar separation downstream the reattachment point, which is promoted during pitching up and delayed during pitching down with an increase in Re. Amiralaei et al. (2010) studied the change of the TEV of a pitching aerofoil ($K = 0.1$) with an increasing Reynolds number from $Re = 555$ to $Re = 5000$. Increasing Re initially increases the size and strength of the TEV but eventually promotes the shedding of the TEV.

Although the behaviour of the vortices is related to the Reynolds number, it is still debated whether the aerodynamics of the pitching wing is

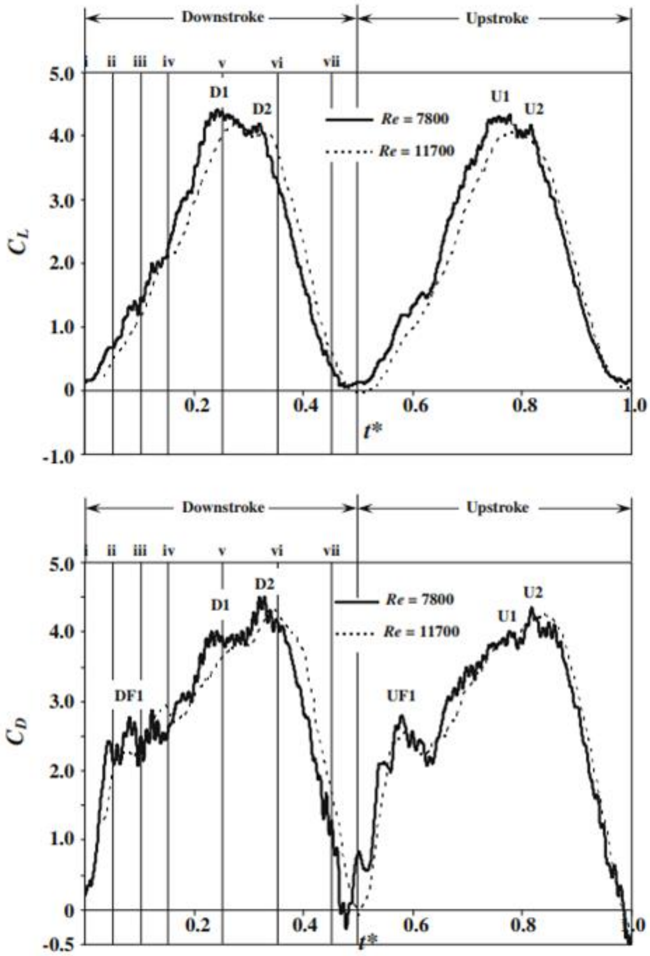

Figure 2.11: Aerodynamic forces of the wing undergoing a simple pitching motion at $Re = 7800$ and $Re = 11700$ (Lua et al., 2010).

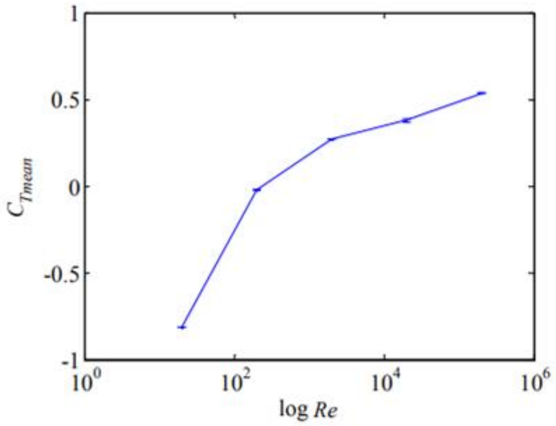

Figure 2.12: Thrust coefficient of the pitching wing as a function of *Re* (Ashraf et al., 2009).

also affected. Lua et al. (2010) studied the lift and drag coefficients of a hawkmoth-like pitching wing, presenting that the influence of *Re* on the lift and drag coefficients was negligible, as illustrated in Fig. 2.11. This result is also confirmed by Robinson and Wissler (1988), Baik et al. (2012) and Das et al. (2016). However, Ashraf et al. (2009) pointed out that the thrust coefficient of the pitching aerofoil is dependent on *Re*, which was improved with an increase in *Re*, see Fig. 2.12. Here, the drag rather than the thrust generated at small *Re*s is due to the plunging motion. Kinsey and Dumas (2008) and Zhu (2011) also mentioned that increasing *Re* was an effective way to improve the thrust coefficient.

2.4.3 Effect of the pitch rate

For the pitching wing, it is obvious that the pitch rate K is a major parameter, which dominants the flow fields and forces over the wing. Figure 2.13 shows the aerodynamics of a flat plate pitching up from $\alpha = 0°$ to $\alpha = 90°$ at the pivot of the leading edge (Granlund et al., 2013). At a small pitch rate $K < 0.03$, the pitch motion delays the stall angle, where all lift curves obey the lift theory, as shown by $2\pi\alpha$. At $K > 0.05$, the lift

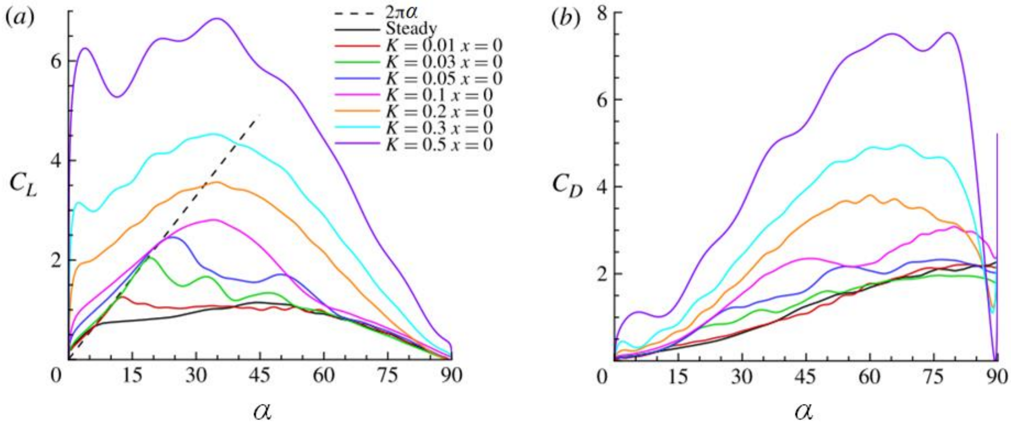

Figure 2.13: Lift (a) and drag (b) coefficients of a flat plate pitching from $\alpha = 0°$ to $\alpha = 90°$ with different pitch rates (Granlund et al., 2013).

curve is no longer able to be computed based on the lift theory, which is due to the flow separation and formation of vortices. Either the maximum lift coefficient or the stall angle is significantly increased with an increase in K. Unfortunately, the drag coefficient is always increased. A similar result is also obtained by Yu and Bernal (2017) who compared the normal force of the flat plate pitching from $K = 0.022$ to $K = 0.39$. This is due to the formation of the large-scale LEV which is influenced by the pitch rate. Increasing the pitch rate shifts the separation point towards the leading edge due to the lower adverse pressure gradient on the suction side, which delays the formation of the primary LEV (Choudhuri and Knight, 1996; Schreck and Robinson, 2002). Meanwhile, the strength of the LEV is enhanced, leading to a higher lift and stall angle (Gharali and Johnson, 2014).

The influence of the pitch rate on the wake of a pitching aerofoil (up to $K = 11.5$) was investigated by Bohl and Koochesfahani (2009). The characteristics of the vortices, such as the locus and strength, become dominant with an increase in the pitch rate. Baik et al. (2012) concluded that the flow evolution on a pitching aerofoil was governed by the pitch rate

($0.314 < K < 1$). At a higher pitch rate, the growth rate of the LEV is slower, which consequently delays the detachment and shedding of the LEV and the TEV, generating a large effective AoA. A contradictory observation, however, was made by Onoue and Breuer (2016), where the vorticity field at various pitch rates ($0.06 < K < 0.175$) exhibits a self-similarity. Smith and Jones (2020) also presented the insensitivity of the vortex formation to the pitch rate ($0.1 < K < 0.3$) by considering trailing wake effects. The wake-induced velocity and unsteadiness of the shear layer remain constant with a large change in the pitch rate. Lee and Gerontakos (2004) pointed out that the effect of the pitch rate on a pitching wing should be considered comprehensively. For example, the occurrence of the flow separation, the AoA of the vortex breakdown and the formation and detachment of the LEV are strong functions of the pitch rate. The location of the flow reversal and convection velocity of the LEV and secondary vortex are not affected by the change in the pitch rate.

2.4.4 Effect of the pitch pivot location

Moving the pivot location from the leading edge to the trailing edge, the aerodynamics of a pitching flat plate becomes dramatically different, as shown in Fig. 2.14 (Granlund et al., 2013). Downstream movement of the pivot makes a monotonic decrease in the lift and drag coefficients but it increases the AoA for the maximum lift and drag. Positive lift spikes are detected at the initiation of the pitching motion when the pivot is located before the mid-chord. On the other hand, negative lift forces are observed when the pivot is located after the mid-chord. This is because the initial position of the starting vortex is dependent on the pivot location (Yu and Bernal, 2017). The starting vortex is generated at the trailing edge when

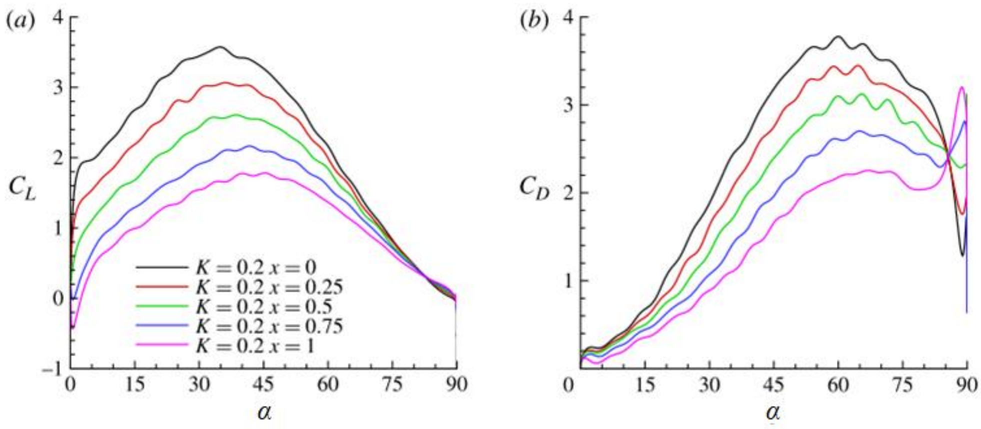

Figure 2.14: Lift (a) and drag (b) coefficients of a flat plate pitching from $\alpha = 0°$ to $\alpha = 90°$ at different pivot locations (Granlund et al., 2013).

the wing pivot is located before the mid-chord, contributing to a positive lift force. Conversely, a downstream pivot location results in the starting vortex formed at the leading edge, giving a negative lift force. The primary vortical structure LEV is also affected by the pivot position, which should be responsible for the different lift and drag curves in Fig. 2.14. The LEV forms earlier with a stronger circulation during the pitching motion when the pivot is close to the leading edge (Li et al., 2019). The delay in the formation of the LEV with a pivot located downstream is attributed to the interference from the starting vortex. It was also proposed that the motion-induced downwash is enhanced, which suppresses the formation of the LEV, as the pivot moves aftward (Ol et al., 2010). An intriguing phenomenon is also observed by Granlund et al. (2013) that there is no contribution from the pitching motion to the aerodynamics of the wing when the pivot is located at the three-quarter chord position.

Further investigations about the influence of the pivot location are made on the thrust performance of the aerofoil. Tian et al. (2016) experimentally studied the difference in the thrust coefficient of a pitching aerofoil with four different pivot locations ($0.16c$, $0.25c$, $0.43c$ and $0.52c$). Forward movement of the pivot leads to a better thrust coefficient, which is due to the increased strength and transverse spacing of the wake vortices. Similar work is also undertaken by Mackowski and Williamson (2017), covering a larger range of pivot locations from $-1c$ to $2c$. The minimum thrust coefficient is obtained when the aerofoil pivots at $0.75c$. Either forward or rearward shift of the pivot results in an improvement of the thrust coefficient. Computational results from Sinha et al. (2021) are consistent with Tian et al. (2016) and Mackowski and Williamson (2017).

2.4.5 Effect of the aspect ratio

The importance of the TV on a stationary wing has been introduced in Sec. 2.3, which also has a significant effect on the aerodynamics of the pitching wing. Yilmaz and Rockwell (2012) and Visbal (2011) studied the flow structures around a finite-span pitching wing and both clarified the developing process of the TV and the LEV, as shown in Fig. 2.15. Their results showed that the LEV exhibited a spanwise variation, which changed from the attachment state to an arc-shaped state with an increase in the AoA. This was caused by the induced velocity from the TV. The spanwise-changing LEV results in a nonuniform pressure distribution along the span on the suction side of the wing whose suction peak is located close to the wing tip, where the LEV intensively interacts with the TV (Schreck and Hellin, 1994). The arc-shaped LEV was also obtained by Visbal and Garmann (2019b) who numerically investigated the dynamic stall on a pitching wing at $AR = 4$. The arc-shaped LEV is formed as the LEV near the wing tip is pinned to the wing surface throughout the pitching motion while lift-off and shedding of the LEV occur near the mid-span.

Figure 2.15 also shows that the spanwise vortices, which are shedding from the leading edge, connect to the streamwise vortices to form a coherent

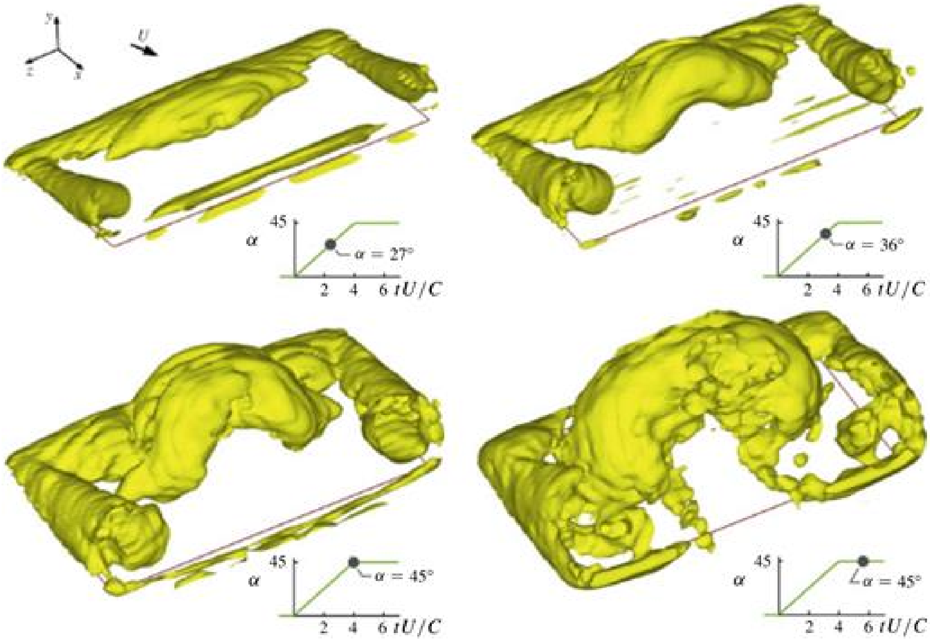

Figure 2.15: Vortical structures of a finite-span pitching wing (AR = 2, $K = 0.098$) at different AoAs (Yilmaz and Rockwell, 2012).

structure. It is also shown that the proportion of the streamwise vortices becomes greater with a decrease in the AR. The flow structure over a finite-span pitching wing (AR = 3) was studied by Von Ellenrieder et al. (2003) using dye flow visualisation. They proposed a wake model which mainly consisted of the LEV and the TEV. The LEV connects to the TEV according to two filamentary vortex lines, forming a ring-like structure. A similar wake structure is observed by Dong and Liang (2010) who investigated the near-field flow structure around a dragonfly. Buchholz and Smits (2006) conducted the flow visualisation experiment of a pitching wing with a very low AR of 0.54 and proposed a vortex skeleton model as shown in Fig. 2.16. The wake structure here predominantly consisted of the streamwise vortices due to the very low AR. Figure 2.16 illustrates that the wake is made up of a couple of horseshoe vortices, resembling a three-dimensional Kármán vortex street. The legs of each horseshoe are influenced by the next two horseshoes, where the first one has an opposite-sign interaction and the second one has a like-sign interaction.

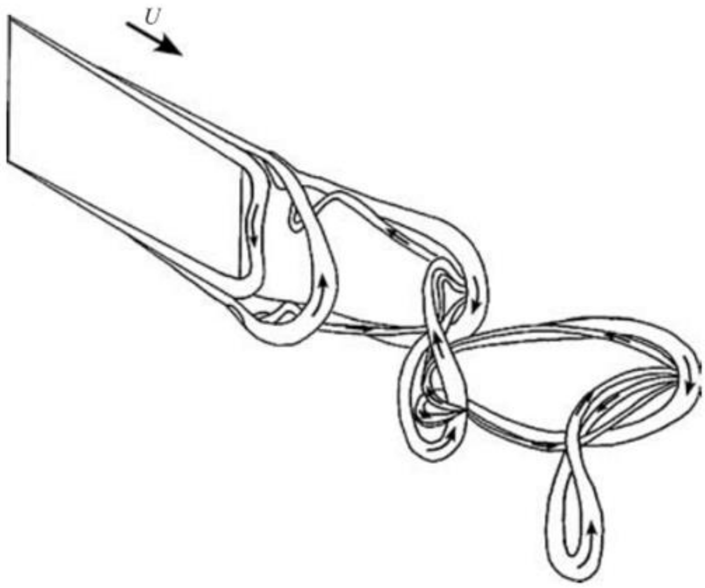

Figure 2.16: Vortex skeleton model of the wake of a very low AR pitching wing (AR = 0.54) (Buchholz and Smits, 2006).

The wake structure of a pitching wing is also dependent on the AR, which subsequently impacts on the energy harvesting efficiency of the wing. By comparing the thrust coefficients of the pitching wing with different ARs, Buchholz and Smits (2008) pointed out that the AR is one of the primary parameters for optimising the thrust coefficient. Generally, reducing AR leads to a lower thrust coefficient. The effect of the AR on the energy harvesting efficiency of a pitching wing was also studied by Simpson et al. (2008); Deng et al. (2014) and Kim et al. (2017), whose results were in excellent agreement. The best energy harvesting efficiency is always obtained from a large AR wing.

The significance of the LEV on a 2D pitching aerofoil has already been discussed and a number of investigations have been made on the characteristics of the LEV. However, there is an equally important vortex for a finite-span pitching wing, namely the TV. The discussions about the development of the TV over a pitching wing are relatively few, although it has a significant impact on the aerodynamics of the wing. Visbal (2017) showed that the TV exhibited the vortex breakdown at a certain AoA during the pitching motion, which was increased by increasing the pitch rate. The TV structure before the vortex breakdown was independent of the pitch rate. Birch and Lee (2005) obtained the same results and confirmed that the TV structure did not have a pronounced change at a fixed incidence at different pitch rates. But they pointed out that the strength of the TV was decreased by the pitch-up motion as compared to that of the stationary wing. In fact, not only the strength but the tangential velocity, axial velocity and turbulence intensity in the inner region of the TV were dependent on the pitch rates and pitching kinematics. The behaviour of the TV under a pitching motion and its impact on the overall flow field are not yet well known.

2.5 Plasma flow control

The objective of flow control is to modify the flow fields into the desired state, achieving specific objectives, including aerodynamic improvement, turbulent mixing enhancement, steadiness manipulation, noise reduction, etc. Flow control is generally categorised into two types called passive and active flow control, respectively. Passive control means no input power while active control is powered, which can be either an open loop (variable but with no flow sensing) or a closed loop with feedback signals from the flow. Many effective methods of active flow control have been proposed in the last century (Cattafesta III and Sheplak, 2011), such as the synthetic jet and the plasma actuator, which have become essential research subjects in the last two decades due to their unique advantages. Compared with the plasma actuator, the synthetic jet can generate higher jet velocity ($>$ 10 m/s) with a similar bandwidth of around 100 kHz but a higher power

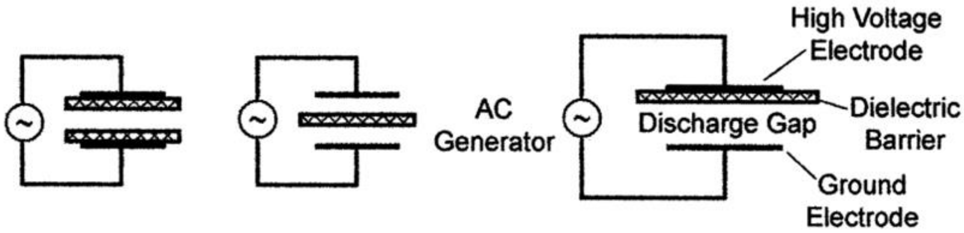

Figure 2.17: Basic configurations of the DBD actuators(Kogelschatz, 2003).

consumption (> 150 W). To achieve flow control using the synthetic jet, a number of orifices are necessary over the wing surface, however. As a result, the plasma actuator is chosen as the control method in this study.

The first experiment of the plasma actuator, known as the dielectric barrier discharge (DBD) actuator, was carried out by Siemens (1857). The basic configuration of the DBD actuators is depicted in Fig. 2.17, which is designed to generate ozone at that time. The dielectric sheet placed between two electrodes prevents the pass of current. Applying enough high voltage, the air in the gap of electrodes breaks down, generating numerous microdischarges and forming the fourth state of matter—the plasma. As time goes, the plasma actuator appears in the sight of aerodynamicists. A new configuration of plasma actuator is designed, which is composed of two electrodes, called DC surface corona discharge actuator. This type of plasma actuator can create an electric wind when it is excited by a high DC voltage, indicating the direct conversion of electric energy into kinetic energy without any moving mechanical parts (Moreau, 2007).

In 1994, Roth's group proposed a new type of plasma actuator, which owed a very similar configuration to the DBD actuator in Fig. 2.17 but removed the air gap, known as surface dielectric barrier discharge (SDBD). The SDBD actuator is generally activated by the high AC voltage, inducing an electric wind up to approximate 10 m/s, allowing for significant flow manipulation. Since 2000s, a large number of investigations about SDBD have been conducted to explore its formation mechanism and ability on flow control.

2.5.1 SDBD plasma actuators

Detailed results about the effect of the excitation voltage on the discharge mode and current were provided by Roth (1995) as shown in Fig. 2.18. As the excitation voltage is initially increased, the initial increase in the current at stages A-B is due to the movement of natural ions and electrons contained in the surrounding gas under the influence of the electric field, giving an extremely low current. Thereafter, this current reaches a constant value (saturation B-C) until all natural, discharged particles move out of the volume. Since a further increase in the excitation voltage generates a relatively strong electric field, the electrons are able to be emitted from the electrode. The electrons moving in the electric field collide with the neutral particles, exciting additional ions and electrons. As a result, the current increases exponentially in stages C-E. When the excitation voltage approaches the breakdown voltage of the gas (V_B, depending on the gas pressure and the gap between electrodes), a glow discharge is formed and the plasma can be viewed by naked eyes (F-H). It should be noted that the voltage distributed on the SDBD plasma actuator starts to be much smaller than the excitation voltage since the resistance of the plasma actuator is reduced with the glowing discharge. The SDBD plasma actuator can be used in this region. When the excitation voltage is increased further, the air is completely broken down and an arc (also called thermal plasma) is formed to connect two electrodes, generating a dramatic high current (H-K).

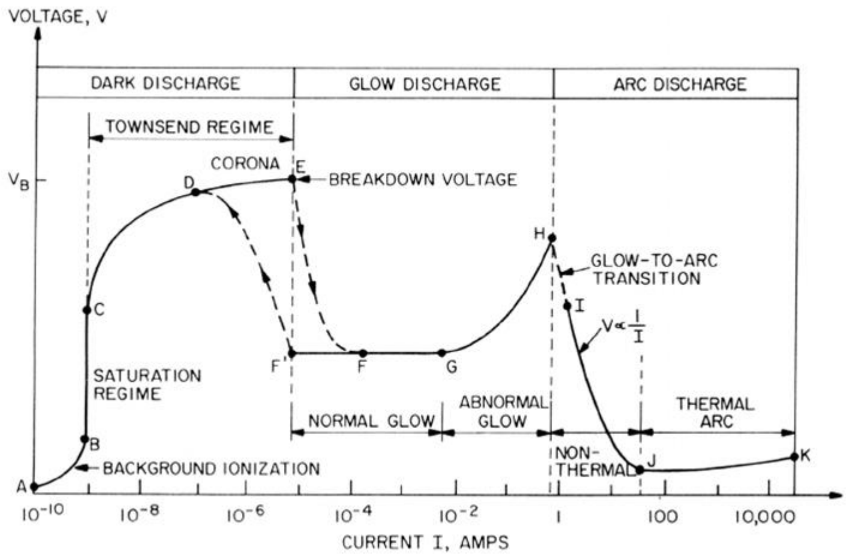

Figure 2.18: Influence of the excitation voltage on the discharge mode (Roth, 1995).

A typical configuration of the SDBD plasma actuator is illustrated in Fig. 2.19 a, which is composed of two electrodes separated by a dielectric sheet. The material of the dielectric sheet generally has a high relative permittivity, like polyamide, polymethyl methacrylate (PMMA), glass, etc. When the SDBD actuator is excited by a high AC voltage, the air in the vicinity of the exposed electrode is weakly ionised, forming a purple glow discharge, see Fig. 2.19b. Due to extremely low emission intensity, a dark environment is necessary to view the formation process. Further increasing the voltage changes the glow discharge into the streamer discharge, accompanying high heat generation and power consumption. The dielectric sheet is then easily damaged due to the ablation of the streamer discharge. Therefore, the excitation voltage has to be at an appropriate level to conduct the SDBD actuator, see stages F-H in Fig. 2.18.

The collision of discharged particles with neutral particles not only produces new ions and electrons but transfers the momentum. As a consequence, the ionic wind is induced by the SDBD plasma actuator blowing from the exposed electrode towards the encapsulated electrode, which can

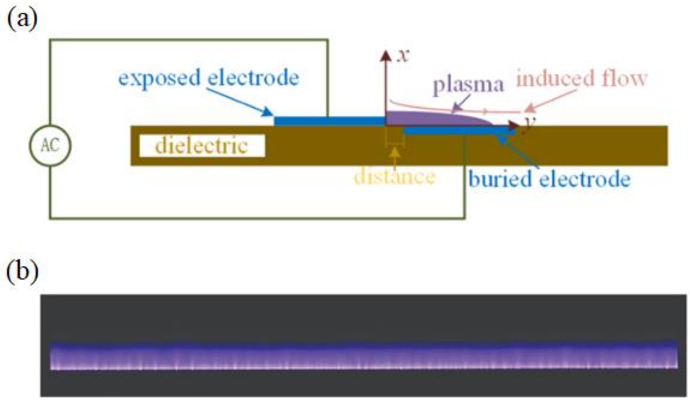

Figure 2.19: (a) A basic configuration of the SDBD plasma actuator (Dong et al., 2017) and (b) plasma generated by the SDBD plasma actuator in the atmosphere (Ashpis and Thurman, 2019).

be used for active flow control (Corke et al., 2010). The formation process of the induced flow by SDBD plasma actuators was studied by Whalley and Choi (2012). Once the SDBD plasma actuator is initiated, the fluid close to the exposed electrode moves along the dielectric sheet. The fluid above the SDBD actuator is entrained towards the dielectric sheet to replenish the ejected fluid due to the electric field, forming a starting vortex. The characteristics of the starting vortex, including its location, velocity and circulation, are scaled with time $t^{2/3}$, $t^{-1/3}$ and $t^{1/3}$, respectively. When the SDBD plasma actuator is operated continuously ($t > 0.5$ s), the starting vortices merge to become a steady plasma jet. Forte et al. (2007) measured the velocity profile in the direction perpendicular to the dielectric sheet for a developed ionic wind.

A typical power supply for the SDBD plasma actuator is sinusoidal alternating voltage, whereby there are the negative half-cycle and the positive half-cycle. The performance of the SDBD plasma actuator at different cycles was examined by Forte et al. (2007) as shown in Fig. 2.20. It is observed that the voltage and current are identical as expected in two cycles but significant differences in the induced flow. The horizontal velocity (primary velocity component) is clearly larger in the negative half-cycle.

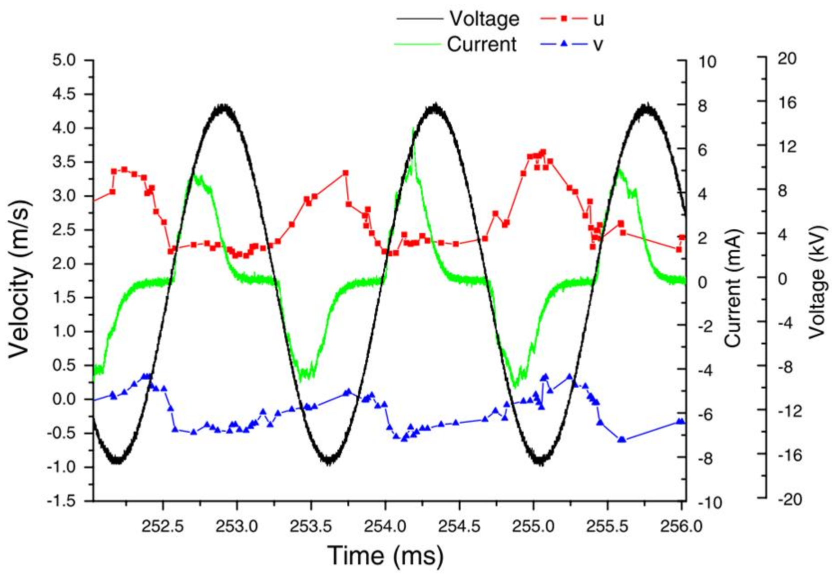

Figure 2.20: Evolution of the ionic wind with the voltage and current on a SDBD plasma actuator (Forte et al., 2007).

The plasma in the negative half-cycle is more uniform than that of the positive half-cycle where streamers are formed. Noteworthy is the vertical velocity (blue triangle-dotted curve) has opposite directions in two cycles, which still remains unclear and needs further study.

Given the importance of the ionic wind for flow control, the optimisation of the SDBD plasma actuator is investigated. Basically, there are five key parameters of the SDBD actuator: amplitude of voltage and current, the material of the dielectric sheet, the thickness of the dielectric sheet, the gap between two electrodes, and the width of electrodes. Conclusions of the impact of these parameters are much similar (Roth and Dai, 2006; Forte et al., 2007), which are shortly summarised in the following. The induced velocity increases with the power frequency and the electrode width. The gap between two electrodes for a particular SDBD actuator has an optimum value. In other words, either too close or too far reduces the effectiveness of the electric-to-momentum transition. Increasing the excitation voltage and reducing the relative permittivity and thickness of the dielectric sheet cause an enhancement of the induced velocity. Nonetheless, the greatest velocity of the SDBD plasma actuator operated with optimised geometry is still less than 10 m/s at the present.

2.5.2 Plasma flow control

The SDBD plasma actuator has been extensively utilised for various types of flow control. The main goals of employing the SDBD plasma actuator in fluid mechanics can be summed up as follows. The first is concerned with boundary layer manipulation, such as advancing or delaying the laminar-to-turbulent transition, reducing the skin friction and enhancing the turbulent mixing (Jukes et al., 2006; Grundmann and Tropea, 2007; Whalley and Choi, 2011). The second objective is to modify the aerodynamic characteristics of the wing, obtaining a high lift and a low drag (Roth, 2003; Post and Corke, 2004; Opaits et al., 2005). The last one is about controlling the vortex-shedding using a pulsed plasma actuator with a particular frequency (Asghar and Jumper, 2003; McLaughlin et al., 2004). Eliminating or changing the vortex shedding leads to the reduction of fluctuating forces and aerodynamics noise (Wang et al., 2013). In light of our current research, we will concentrate our review on flow control on the wing.

Corke et al. (2002) examined the influence of the SDBD plasma actuator on the aerodynamic forces of a NACA 0009 aerofoil at $Re = 1.8 \times 10^5$ before the stall angle from $\alpha = 0°$ to $\alpha = 10°$. Both lift and drag coefficients are increased with plasma on. They assumed that the function of the plasma actuator here (without separation) was equivalent to adding the camber of the aerofoil. Flow separation controlled by the SDBD plasma actuator on an aerofoil was studied by Roth (2003) as shown in Fig 2.21. Flow separated at the leading edge almost fully reattaches to the wing surface when the plasma actuator is actuated, resulting in a significant reduction of

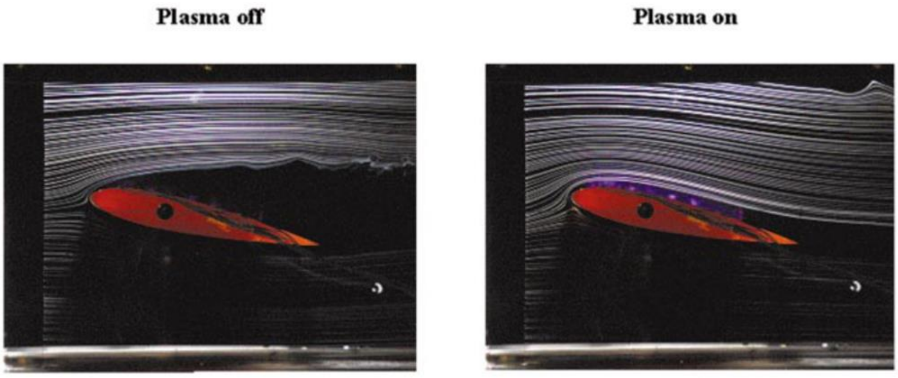

Figure 2.21: Flow fields around a NACA 0015 aerofoil with plasma off and on at $\alpha = 12°$ and $Re = 2.5 \times 10^4$.

the wake area. Therefore, the lift of the aerofoil is expected to be increased. Flow separation control was also conducted by Post and Corke (2004) who separately placed the SDBD actuator at the leading edge and the half-chord of a NACA 66_3-018 aerofoil at $Re = 7.7 \times 10^4 \sim 3.33 \times 10^5$. The separated leading edge flow can be effectively modified by the plasma actuator up to 8° past the stall angle, where the lift coefficient is improved and the drag coefficient is reduced. Furthermore, they pointed out that placing the plasma actuator at the leading edge is most effective.

Similarly, Vorobiev et al. (2008) placed the SDBD actuators along the span separated at the mid-span of a NACA 0009 wing at $Re = 2.7 \times 10^4 \sim 1.34 \times 10^5$. The lift of the wing from $\alpha = 0°$ to $\alpha = 10°$ is enhanced up to 30% by two plasma actuators but this enhancement becomes weaker with Re. They demonstrated that the plasma actuator affected the aerodynamics of the wing in two ways consisting of adding momentum to flow and suppressing viscous effect in the vicinity of the trailing edge. In addition to the lift enhancement, a rolling moment is obtained by operating each side plasma actuator singly. He et al. (2009) and Feng et al. (2015) examined the impact of the SDBD plasma actuator when it was placed at the trailing edge of a NACA 0015 aerofoil at $Re = 2.17 \times 10^5$ and $Re = 3.07 \times 10^5$, showing that the plasma actuator seemed to behave as a virtual trailing-edge

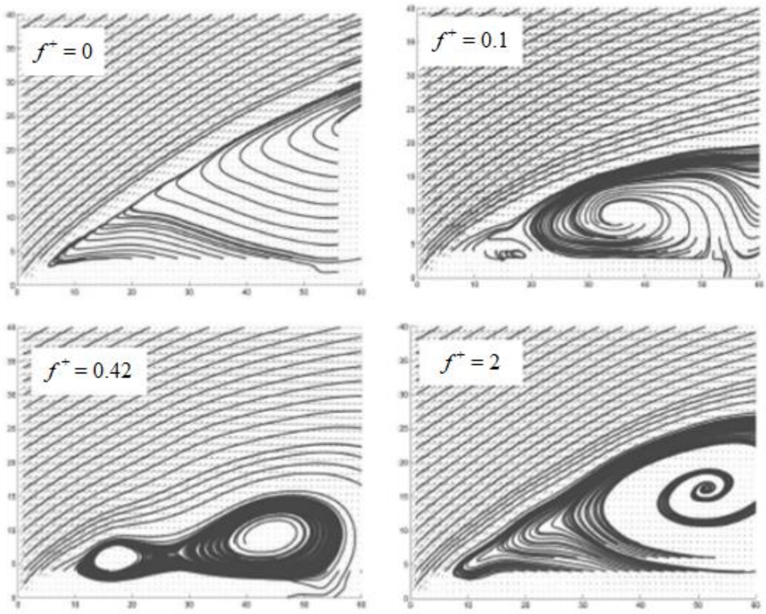

Figure 2.22: Flow fields around a plate aerofoil with different f^+ at $\alpha = 24°$ and $Re = 3 \times 10^3$ (Greenblatt et al., 2012).

flap. Overall, the Reynolds number of the wing is generally less than 10^6 to achieve effective flow control with the SDBD plasma actuator. Moreover, the results from He et al. (2009) presented that the pulse-modulated SDBD plasma actuator achieved a better control than the steady one, where the stall angle was further postponed 4°. Here, the optimum modulation frequency of the pulsed plasma actuator is at $f^+ = fc/U_\infty = 1$, where f is the modulation frequency, c is the chord length.

A pulsed SDBD plasma actuator means that its excitation voltage is modulated by a rectangular wave at a certain duty cycle and modulation frequency. Consequently, a starting vortex is produced in every single pulse. Some investigations present that the pulsed SDBD plasma actuator can be more effective than the steady one if the frequency of the starting vortex is appropriate. Greenblatt et al. (2012) studied the separation control on a flat plate by the pulsed SDBD plasma actuator at $\alpha = 24°$ and $Re = 3 \times 10^3$, as shown in Fig. 2.22. The lift improvement on this plate aerofoil is determined by f^+. Around $f^+ = 0.4$, two recirculation areas are formed over the suction surface due to the merger of the leading-edge shear layer and the naturally growing vortex, resulting in the greatest lift increase. Sato et al. (2015) investigated the influence of f^+ from 0.25 to 25 on separation control of a NACA 0015 aerofoil at $Re = 6.3 \times 10^4$ and $\alpha = 12°$. The unsteadiness of the leading-edge-separated shear layer is effectively enhanced at $f^+ = 5$ and 15, advancing the transition of the shear layer from laminar to turbulent. This results in the reattachment of the separated flow and the formation of the separation bubble, producing additional lift. Apart from leading-edge separation control, the pulsed plasma actuator is also applied close to the flap shoulder of the NASA Energy Efficient Transport aerofoil to mitigate the trailing-edge separation at $Re = 2.4 \times 10^5$ (Little et al., 2010). They pointed out the pulsed SDBD plasma should be actuated at a frequency equivalent to the natural frequency of the flow field rather than a high f^+ which could be treated as the quasi-steady forcing. The momentum transferred from the freestream to the wake is improved by the pulsed plasma actuator with an appropriate f^+, reducing the size of the separation region.

Given the importance of the TV described in Sec. 2.3, the influence of the SDBD plasma actuator is also utilised to modify the TV of a finite-span wing. Hasebe et al. (2011) investigated the effect of the blowing and suction SDBD plasma actuator on the TV of a NACA 0012 wing at $Re = 3 \times 10^3$, showing that both plasma actuators successfully reduce the strength of the TV but lead to a lower lift-to-drag ratio. Boesch et al. (2010) examined the influence of the SDBD plasma actuator on the TV of a NACA 4418 wing at $Re = 1.5 \times 10^5$. The TV becomes diffused and moves outboard under the influence of the plasma actuator, which in turn mitigates the influence of the downwash, generating a high lift.

As already noted, in the present work, the TV also refers to the LEV of

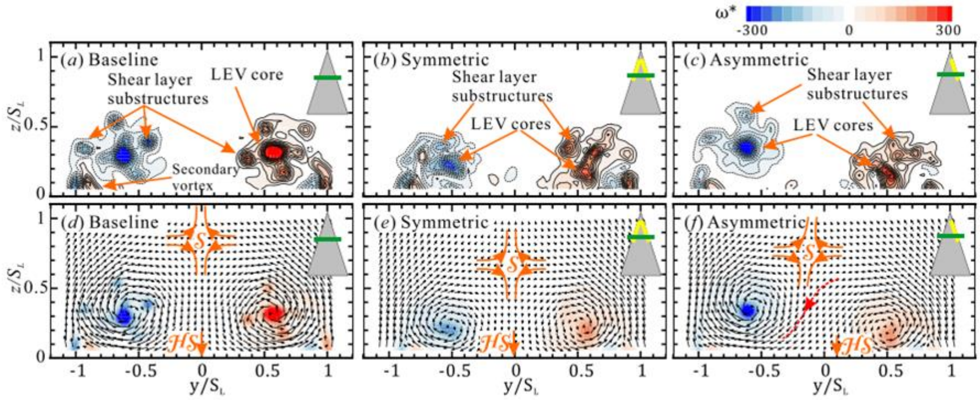

Figure 2.23: Vorticity fields of the delta wing in the cross section at $\alpha = 36°$ and $Re = 5 \times 10^4$:(a) and (d) baseline cases, (b) and (e) symmetric control cases, and (c) and (f) asymmetric control cases (Shen and Wen, 2017).

the delta wing due to their similarity. Figure 2.23 depicts the vorticity field of the delta wing with and without plasma control at $\alpha = 36°$ and $Re = 5 \times 10^4$ (Shen and Wen, 2017). The separated shear layer at the wing tip is pulled towards the wing surface by the SDBD plasma actuator, influencing the structure of the TV. In particular, the TV breakdown is delayed by the symmetrical control (Figs. 2.23b and e) but promoted by the asymmetrical control (Figs. 2.23c and f). The aerodynamic forces of this delta wing, however, do not exhibit any changes. A different result was obtained by Greenblatt et al. (2008) who used the pulsed plasma actuator to modify the TV after the vortex breakdown at $\alpha = 36°$ and $Re = 2 \times 10^4$. They found that the breakdown of the TV was delayed under the influence of the plasma actuator at $f^+ = 1$, resulting in a significant increase in the lift. Similar results were also mentioned by Sidorenko et al. (2013) but they pointed out that $f^+ = 2$ was the optimum frequency.

Apart from the traditional SDBD plasma actuator illustrated in Fig. 2.19, several novel types of the SDBD plasma actuator are proposed in the recent decade, like the multiple-arrayed plasma actuator, the plasma synthetic jet actuator, the 3D plasma actuator and the plasma vortex generator, see

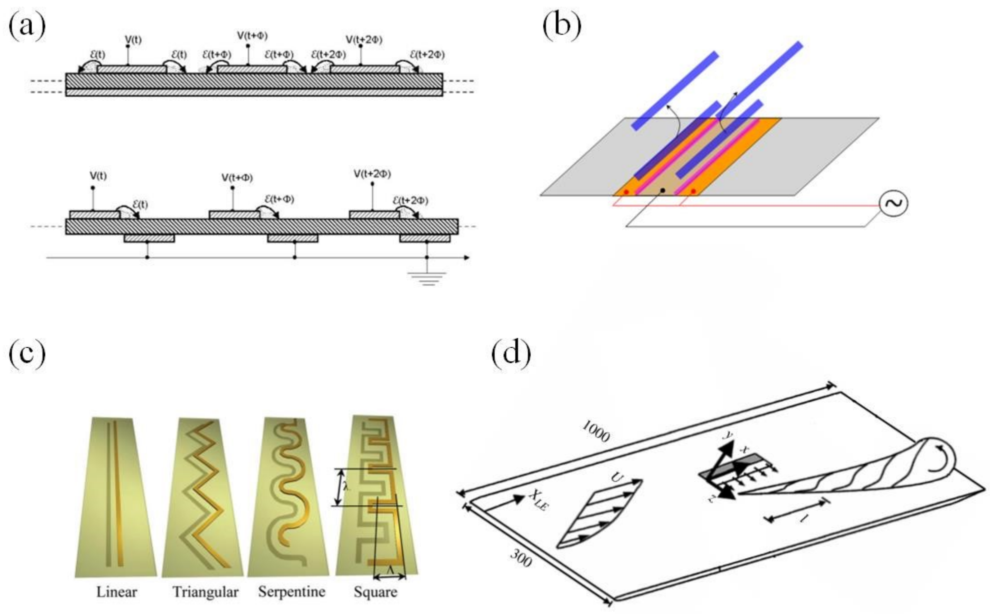

Figure 2.24: Novel SDBD plasma actuators:(a) multiple arrays (Roth, 2003), (b) the synthetic jet (Santhanakrishnan et al., 2006), (c) 3D plasma actuators (Wang et al., 2011) and (d) the vortex generator (Jukes and Choi, 2013).

Fig. 2.24. Roth (2003) arranged a series of the SDBD plasma actuators to pursue a better separation control on the aerofoil. Compared to a single SDBD plasma actuator, the induced velocity is enhanced by this multiple-arranged actuator (Forte et al., 2007). This enhancement depends on many discharge parameters, such as the space between two actuators, the number of the actuators and so on. Inspired by the synthetic jet, two SDBD plasma actuators are axisymmetrically placed to generate an induced jet normal to the wall (Santhanakrishnan et al., 2006), as shown in Fig. 2.24b. When actuated, the fluid moved by each single SDBD plasma actuator ideally encounters at the centre of two SDBD actuators, forming a pair of vortices moving vertically away from the wall. The behaviour of this vortex pair should follow the rules of the starting vortex proposed by Whalley and Choi (2012).

Velocity fields around the above-mentioned SDBD plasma actuators are generally 2D. To produce a 3D flow field, Wang et al. (2011) proposed three different geometries of electrodes (triangular, serpentine and square) on the SDBD plasma actuator, see Fig 2.24c. Their computational results exhibited that newly designed electrodes generated much wider and stronger vorticity, which was probably more effective in an application of the turbulent mixing. Instead of directly using the induced velocity, the SDBD plasma actuator can be placed in the freestream at a yaw angle to generate a streamwise vortex for flow control (Jukes and Choi, 2013). The strength of this streamwise vortex is dominated by the plasma-to-freestream velocity ratio, the yaw angle and actuator length. The formation of the streamwise vortex is due to the roll-up of negative vorticity at the outer edge of the shear layer. Unlike the conventional vortex generator, the existence of the streamwise vorticity is controllable on the SDBD vortex actuator and no pressure drag or device drag is introduced (Wang et al., 2013).

2.6 Summary

Significantly different aerodynamics between the infinite-span and finite-span wings have been introduced, which gives several crucial questions in the following that remain elusive and require thorough study: (a) aerodynamics of a very low AR wing, (b) characteristics of the vortical structures over a very low AR wing at different AoAs, (c) effect of the pitching motion on the development of vortices over a very low AR wing, (d) interplay of the LEV and the TV over a stationary and unsteady very low AR wing and (e) influence of the plasma actuator on the aerodynamics of a low AR wing by controlling the TV.

Chapter 3

Experimental methods

3.1 Introduction

This chapter gives information about the experimental facilities used in this study. Detailed information about the wind tunnel used throughout this study is introduced along with the dimension of the wing model. The aerodynamic forces and velocity measurements are explained and different experimental conditions are defined. The method of obtaining the quasi-3D vortical structures and processing the raw particle image velocimetry (PIV) image is given. The design of the plasma actuator for flow control is sketched. The synchronisation of all parts, such as the motion control, force measurement, PIV system and plasma excitation, is explained.

3.2 Wind tunnel facility

All experiments were conducted in an open-return wind tunnel at the University of Nottingham, which had the test section of 1.5 m $\times$ 0.9 m $\times$ 0.9

(a)

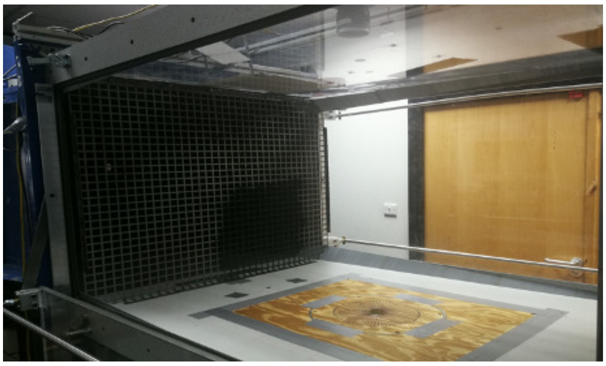

(b)

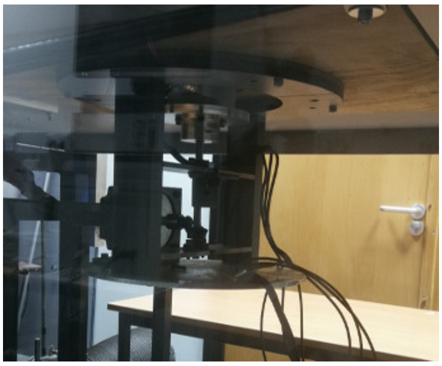

Figure 3.1: Open-return wind tunnel at the University of Nottingham:(a) test section and (b) turntable and stepper motor at the bottom of the wind tunnel.

m (length × width × height) and the maximum wind speed of 20 m/s, as shown in Fig. 3.1a. In this study, the freestream velocity U_∞ was set to 10 m/s, which was monitored by a Pitot tube placed 0.2 m downstream of the contraction section of the wind tunnel. To promote the transition to turbulence near the leading-edge of the wing, we installed a turbulence-generating grid upstream of the test section to increase the freestream turbulence level to 4%. A turntable controlled by a stepper motor was set 0.5 m downstream of the inlet of the test section at the bottom of the wind tunnel, providing precise angle movement of the model, see Fig. 3.1b.

3.3 Wing model

A thin rectangular flat plate was mounted on the turntable at the bottom of the wind tunnel. The profile of the 3-mm thick model is illustrated in Fig. 3.2a, which was made of an aluminium composite with a 3D-printed elliptic leading edge with the 18-mm major axis and the 3-mm minor axis. It had a chord length $c = 260$ mm and half span length $s = 36$ mm, giving a very low AR of 0.277 with a thickness-to-chord ratio of 1.2%. The maximum blockage of the wind tunnel due to this wing model was 1.8% at an AoA of 90°. Wang et al. (2014) pointed that increasing the turbulent intensity might cause early transition in the shear layer and postpone the flow separation, giving a concept of the effective Reynolds number. Considering the installation of the turbulence-generating grid, the effective chord Reynolds number of the wing in this research was increased 15 times from $Re = 2 \times 10^5$ to $Re = 3 \times 10^6$ (Wang et al., 2014). In this test, two coordinate systems were used, as shown in Fig. 3.2b, both of which had the origin located at the leading edge at the mid-span. One was the laboratory-based coordinate system which had x in the streamwise direction, y in the cross-flow direction and z in the spanwise direction, corresponding to their mean velocity components U, V and W and fluctuation velocities u, v and w. The other one was the wing-based coordinate system, namely x_m in the chordwise direction, y_m in the normal-to-wing direction and z_m in the spanwise direction, whose mean velocity components were U_m, V_m and W_m.

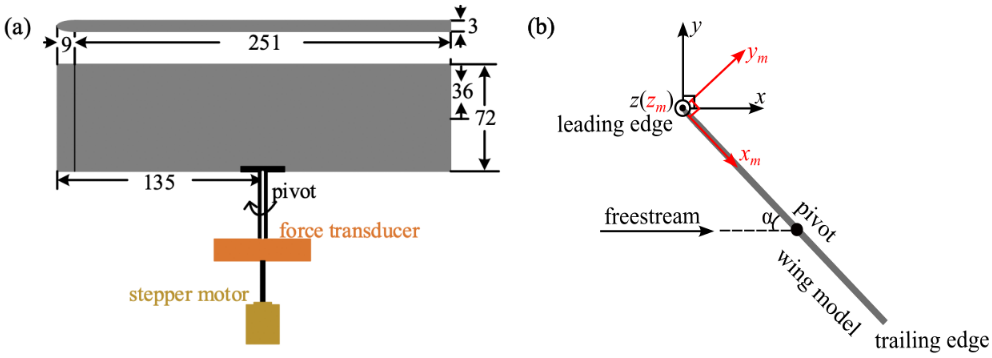

Figure 3.2: (a) Plan and side view geometries of the very low AR wing. All dimensions are in millimetres. (b) Two different defined coordinate systems.

3.4 Force measurements

Aerodynamic forces on the test model were measured using a Kyowa LSM-B-SA1 three-component force transducer whose accuracy was ±0.02 N. The wing was attached to the force transducer via a strut, which was rotated by a step motor, giving a 150-mm clearance to avoid the boundary layer over the wind tunnel floor, see Fig. 3.2a. The measured signals were sent to a Kyowa DPM-911B strain-gauge amplifier, which were then converted to digital signals by a NI 9215 16-bit analogue-to-digital converter on a CompactRIO. At the stationary condition, the aerodynamic forces were acquired at a sample rate of 2 kHz for 10 s from 0° to 90° at an interval of 1.8°. To avoid any hysteresis effect, we waited 10 seconds at each AoA before starting force measurements. For the pitching cases, the data acquisition rate was set according to the non-dimensional pitch rate $K = \dot{\alpha}c/2U_\infty$ as shown in Tab. 3.1. At least 2000 data points were acquired during the pitching motion in all cases. To remove undesired signal fluctuations due to the model vibration during pitching, a low-pass filter was used, whose cutoff frequency of 10 Hz was less than the natural frequency of the whole system ($\sim$ 24 Hz). The acceleration and deceleration at the start and the end of the motion, respectively, were smoothed by C^∞

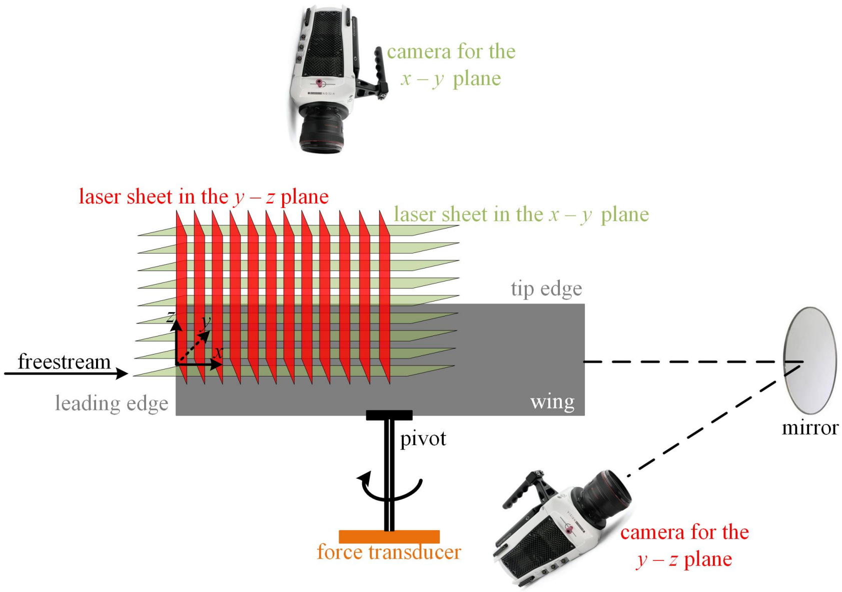

Figure 3.3: Imaging configuration for PIV measurements in planar and cross-flow sections.

function (see Sec. 3.6). The force measurements were synchronised with the pitch motion, and were repeated 50 times for each case. A moving averaging was also applied to the measured data to further smooth the signals. For plasma control cases, force measurements were conducted at a sampling rate of 2000 Hz from 0° to 90° at an interval of 1.8°, each of which lasted 3 s with plasma off followed by 3 s with plasma on. The measured axial force F_A and normal force F_N on the wing were converted to lift force $F_L = (F_N \cos\alpha - F_A \sin\alpha)$ and drag force $F_D = (F_N \sin\alpha + F_A \cos\alpha)$, where α is the AoA. Here, the normal force coefficient, axial force coefficient, drag coefficient and lift coefficient are given by $C_N = F_N/\frac{1}{2}\rho U_\infty^2 A$, $C_A = F_A/\frac{1}{2}\rho U_\infty^2 A$, $C_D = F_D/\frac{1}{2}\rho U_\infty^2 A$ and $C_L = F_L/\frac{1}{2}\rho U_\infty^2 A$, respectively, where U_∞ is the free-stream velocity, ρ the air density and A the plane area of the test model.

3.5 Particle image velocimetry measurements

Table 3.1: Parameters of force and PIV measurements at different experimental conditions.

		Stationary cases	Pitching cases(K)					Plasma actuators			
		$10.8° \sim 50.4°$	0	0.003	0.01	0.03	0.08	baseline	blowing	suction	still air
Forces	Sample rate (Hz)	2000	300	300	1000	3000	8000	2000	2000	2000	-
	Number of tests	50	50	50	50	50	50	50	50	50	-
	Sample time (s)	10	10	-	-	-	-	3	3	3	-
PIV	Sample rate (Hz)	200	200	270	360	540	900	320	320	320	960
	Number of tests	-	2	5	8	10	-	-	-	-	-
	Sample time (s)	2	5	-	-	-	-	1.5	2.5	2.5	3
	Angle of two adjacent images (°)	-	-	0.05	0.125	0.25	0.4	-	-	-	
	Number of image pairs for averaging	400	1000	42	45	40	30	480	800	800	2880

The velocity field around the wing was captured using a high-speed PIV technique, where the 2D data on the x-y and y-z planes were measured separately, as shown in Fig. 3.3. To depict the quasi-3D vortical structures of the LEV and the TV over the wing, the time-averaged velocities in two measured planes were assembled together. The wind tunnel was seeded with Di-Ethyl-Hexyl-Sebacate (DEHS) particles approximately 0.5 μm in diameter, which were generated by two seeder generators (TSI 9307-7) placed upstream of the wind tunnel test section. The test area was illuminated using a Litron LDY 302-PIV Nd:YLF dual-cavity laser with 15 mJ per pulse and captured with a CMOS high-speed camera with a resolution of 1280 $\times$ 800 pixels. The time delay between laser pulses was set to 50 μs for the x-y plane measurements while a shorter time delay of 30 μs was set for the y-z plane measurements. Most of our measurements were made over the top half of the wing upstream of the pivot ($x_m/c = 0.52$).

The camera was fixed on the top of the wind tunnel for the x-y plane measurements, where the thickness of the laser light sheet was set to 0.5 mm, investigating 18 x-y planes from $z/s = 0$ to $z/s = 2$. For the y-z plane measurements, a round mirror with a diameter of 100 mm was placed 300 mm downstream of the test model at 45° to the freestream so that the camera was able to be set outside the wind tunnel, see Fig. 3.3. Here, the laser sheet thickness was increased to 2 mm, investigating 14 planes from $x_m/c = 0$ to $x_m/c = 0.52$. For the stationary and plasma control cases, a focal length of 110 mm lens was used for the x-y plane measurement while a focal length of 200 mm lens was for the y-z plane measurement. Differently, in order to capture the flow field successively from $\alpha = 0°$ to $\alpha = 90°$ during the pitching motion, a focal length of 50 mm lens and 110 mm lens was used for the x-y plane measurements and the y-z plane measurements, respectively, to view a large field. For the stationary case, the quasi-3D PIV measurement was conducted at six AoAs, including $\alpha = 0°, 10.8°, 20.7°, 30.6°, 40.5°$ and $50.4°$. Considering that the effectiveness of flow control by the plasma actuator was related to the AoA (Chappell and Angland, 2012), a preliminary test was also conducted to find the maximum AoA at which the TV could be modified by two types of the plasma actuator. A negligible change in the TV was observed after $\alpha > 15°$ for blowing and suction control. Therefore, PIV measurements were only finished at $\alpha = 10°$ and $\alpha = 15°$ for plasma control cases.

It should be noted that the laser sheets in the y-z plane did not stay perpendicular to the wing surface with increasing AoA, although the laser sheets in the x-y plane did. A summary of the PIV parameters is given in Tab. 3.1. The velocity vectors were obtained by Dantec DynamicStudio 2015a software by iteratively adjusting the size and shape of the individual interrogation areas depending on the local seeding densities. The minimum and maximum interrogation areas of measurement planes were 8 and 32 pixels with a 50% overlap, respectively. The universal outlier detection analysis was also applied to remove spurious vectors (Westerweel and Scarano, 2005), where any invalidated vectors were replaced by the median value calculated using 3×3 neighbourhood vectors. This gave about 16000 vectors in each frame with a spatial resolution of $0.005c$.

The velocity data for the stationary and plasma control cases was time-averaged but it is phase-averaged for the pitching wing, where the 2D PIV images were ensemble-averaged at a given AoA during the pitching motion. Here, the "phase" indicated the attitude of the pitching wing instead of the phase of the flow or vortex motion. Similar phase-averaging techniques have been used to study pitching and plunging aerofoils (Baik et al., 2012; Akkala and Buchholz, 2017; Gupta and Ansell, 2019). In order to reduce the phase-averaging errors due to velocity fluctuations over a pitching wing, all PIV images within $\pm 0.5^\circ$ of the target AoA were used for averaging in this study. As a result, the total number of PIV image pairs used for phase averaging at each AoA was increased to between 30 and 45 depending on the non-dimensional pitch rate K, see Tab. 3.1. Here, the number of tests indicates the number of pitching motions which we have repeated. Uncertainty in velocity measurements using PIV was estimated by $U_e = \sqrt{\frac{D_e^2}{T_i^2} + (-\frac{D_s}{T_i^2})^2 T_e^2}$ (Kline and McClintock, 1953), assuming that its primary sources of error were the shift distance D_s of seeding particles and the interval time T_i between image pairs. Here, D_e was the uncertainty in particle shift distance, which was about 0.15 pixel obtained by Dantec DynamicStudio 2015a software. The uncertainty in the interval time T_e between image pairs was negligible. This gave $U_e/U_\infty = 5.2\%$, which was similar to the PIV measurements error estimated by Westerweel (1997). Estimated errors of derived quantities, such as the vorticity and circulation, were less than 8% and 10%, respectively.

PIV measurements of the flow velocity induced by the plasma actuator were conducted without external flow in a transparent sealed box of $0.6 \times 0.3 \times 0.3$ m^3. The same coordinate in Fig. 3.2 was used. This box was pre-seeded particles via a nozzle and waited 10 minutes to resume the quiescent condition. The camera equipped with a 110 mm Canon lens viewed an area of $2.5s \times 4s$ parallel to the y-z plane at $x = 0.5c$, which was illuminated by a 0.5 mm thick laser sheet with a time delay of 150 μs between two pulses. Here, the sample rate and time of the PIV were set to 960 Hz and 3 s, respectively. PIV processing was the same as aforementioned.

Identification of the vortices over a very low AR wing was made using the λ_2-criterion (Jeong and Hussain, 1995), while the vortex centroid was determined by a minimum negative value of λ_2 within the uncertainty of $0.005c$. Other vortex identification techniques such as the Γ_1 criterion (Michard et al., 1997) and the Q-criterion (Chong et al., 1990) were also tested, both of which gave similar results.

3.6 Pitching motion control

The wing pitch motion was controlled using a stepper motor and an NI 9512 drive with a minimum step angle of 0.1°. The pivot in this study was located at $0.52c$ rather than $0.5c$ due to the added elliptical leading edge. Here, a constant pitch rate during the pitch-up (leading-edge up) motion and pitch-down (leading-edge down) motion was maintained from $\alpha = 0°$ to 90° and from $\alpha = 90°$ to 0°, respectively. To reduce the unwanted acceleration effects on the force measurements at the start and the end of the pitch motion, the following smoothing transient suggested by Eldredge et al. (2010) was applied

$$\alpha = \frac{K}{b}\ln\left[\frac{\cosh(b(\tau-\tau_1))}{\cosh(b(\tau-\tau_1-\frac{\alpha_{max}}{2K}))}\right]+\frac{\alpha_{\max}}{2}, \tag{3.1}$$

where

$$K = \frac{\dot{\alpha}c}{2U_\infty}, \tag{3.2}$$

$$b = \frac{\pi^2 K}{2\alpha_{max}(1-\sigma)}. \tag{3.3}$$

Here, α is the AoA in radians, K is the non-dimensional pitch rate as defined by Eq. 3.2, τ is the non-dimensional convective time ($\tau = tU_\infty/c$), α_{max} is the maximum pitch angle, $\dot{\alpha}$ is the angular velocity of the wing, τ_1 is the start of the ramp and σ is the smoothing parameter which was set to 0.9 for this test. A preliminary test indicated no appreciable force fluctuations were experienced with this smoothing transient at the pitch rate $K < 0.1$.

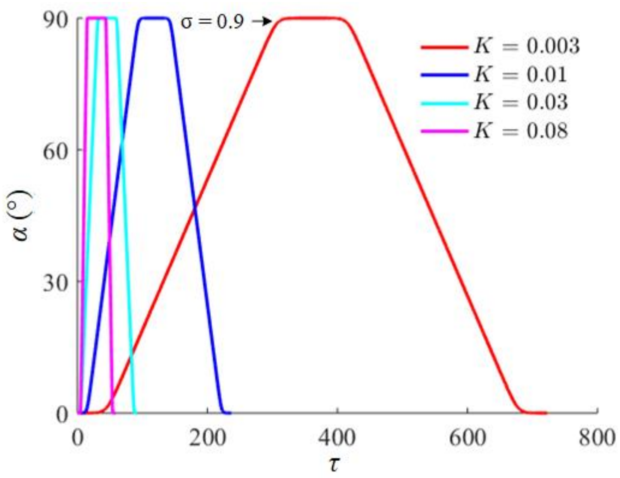

Figure 3.4: The pitch motion profiles for $K = 0.003, 0.01, 0.03$ and 0.08 consisting of pitch-up, hold and pitch-down.

Typical pitch-up and pitch-down motion profiles are presented in Fig. 3.4, where the wing was held 20 convective times before pitching down from the maximum pitch angle ($\alpha = 90°$).

3.7 Plasma actuators

The plasma actuators were placed only on one side of the wing model, see Fig. 3.5, where two different configurations of plasma actuators were considered. The first plasma configuration was intended to blow a synthetic plasma jet away from the wing tip, while the second plasma configuration was intended to draw the air from the wing tip. They were called the blowing and suction plasma actuators, respectively. Both plasma actuators consisted of an upper exposed electrode and a lower encapsulated electrode made of a single layer of 0.05-mm thick and 240-mm long copper tapes, separated by two layers of 0.15-mm thick Cirlex sheets. For the blowing plasma actuator, a pair of 10-mm wide upper electrodes was attached 10 mm from the wing tip as shown in Fig. 3.5a. For the suction plasma actuator, on the other hand, a 3-mm wide upper electrode was attached

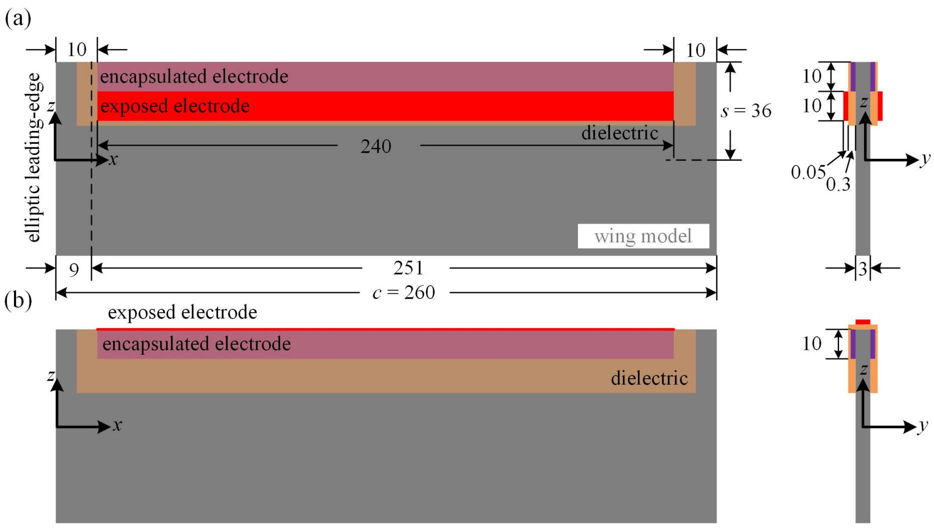

Figure 3.5: Configuration of the plasma actuator on the very low AR wing: (a) blowing plasma actuator and (b) suction plasma actuator. All dimensions are in millimetre.

over the tip edge of the wing, see Fig. 3.5b. The Reynolds number based on the thickness of the plasma actuators and the freestream velocity was $Re_p = 270$, which was below the critical Reynolds number for triggering boundary-layer transition (Schlichting, 1955). Therefore, the roughness effect of the model wing due to the plasma actuators was negligible. Plasma actuators were excited with a sinusoidal waveform by a Minipuls 6 AC power supply at a peak-to-peak voltage $E_{PP} = 18$ kV and an operating frequency of 7 kHz. Due to the thickness restriction, it was not possible to install the plasma power cables within the wing model in this case. To mitigate the impact of the cables on the force measurements, all cables were placed along with the wing edges and support before being taken out through the bottom floor of the wind tunnel. The performance of plasma flow control during the "plasma on" period was evaluated against the "plasma off" conditions throughout this study.

The plasma actuators were operated either at a steady mode or a pulsed mode at a 50% duty cycle. Here, the normalised pulsed frequency was given by $f^+ = fc/U_\infty$, where f is the modulation frequency, c is the chord

Table 3.2: Momentum coefficient of different plasma actuators.

f^+	0	2
C_μ (blowing plasma actuator)	0.4%	0.27%
C_μ (suction plasma actuator)	0.32%	0.21%

length of the wing model and U_∞ is the freestream velocity. Preliminary tests showed that the effective pulsed-mode frequency was $f^+ = 2$, which was identical to that of Sidorenko et al. (2013) who examined flow control on a delta wing. The momentum coefficient for the plasma actuators used in this work is shown in Tab. 3.2. Here, the momentum coefficient of the plasma jet was defined by $C_\mu = 2M/\rho U_\infty^2 c$, where the momentum flux is given by $M = \int \rho W^2 \mathrm{d}y$ (Jukes and Choi, 2009).

3.8 Experimental procedure

All experimental facilities as already noted, including motor control, force measurement, PIV system and plasma generation system, were synchronised by the Compact RIO and controlled by a high-performance PC according to LabView software as shown in Fig. 3.6. Details about the virtual instruments (VIs) used in this study can be seen in Appx. A. Here, the PIV system and plasma power supply were set to external trigger mode controlled by a rectangular wave output from a NI 9264 voltage-output module. The voltage and frequency of this rectangular wave were able to be delicately defined depending on the experimental conditions. The output signals of NI 9264 and Minipuls 6 were verified and monitored using the Tektronix DPO oscilloscope. The acquired force data was stored in the Compact RIO according to a VI while the captured PIV images were stored on the PC according to Dantec DynamicStudio software. A time delay among these different systems was less than 5 ns.

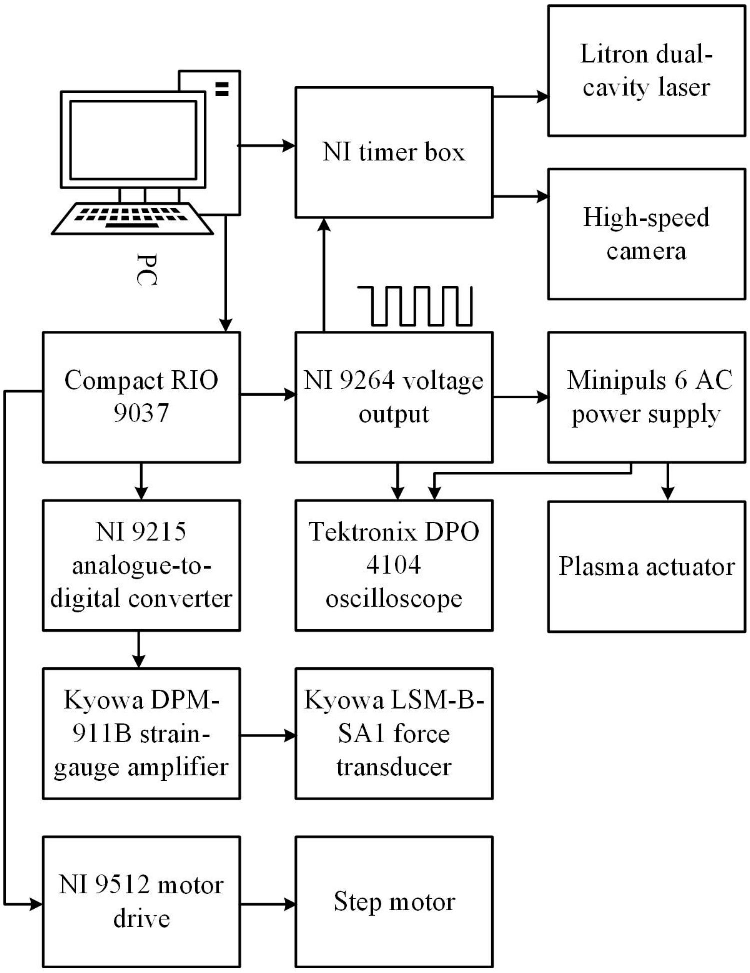

Figure 3.6: Synchronisation of all experimental facilities, including force measurement system, PIV measurement system, motor control system and plasma generation system.

The general procedure for the experiment was as follows. Firstly, the high-speed camera and laser sheet were positioned and the excitation power of the plasma actuator was setup (i.e. voltage amplitude and frequency). The voltage and frequency of the triggering wave were determined. Then, the wind tunnel would be operated to the target wind speed, followed by opening the high-pressure valve to generate seeding particles. Next, the particularly designed VI would be run and the rest of experiments would be conducted automatically.

Chapter 4

Vortices over a very low AR wing under stationary condition

4.1 Introduction

In this chapter, we pay attention to the characteristics of a stationary very low AR wing at various AoAs from $\alpha = 0°$ to $50.4°$ via PIV and force measurements. The aerodynamics of this very low AR wing are compared to that of the 2D aerofoil and their differences are studied. Particular attention is given to the vortical structures over the low AR wing. The development of the LEV along the span and the TV along the chord at different AoAs is explored by examining their circulation and shapes. The interaction between the LEV and the TV is studied based on the distribution of the Reynolds stress. Thereafter, the effect of the TV on the leading-edge separation and the behaviour of the LEV is discussed using the estimated downwash.

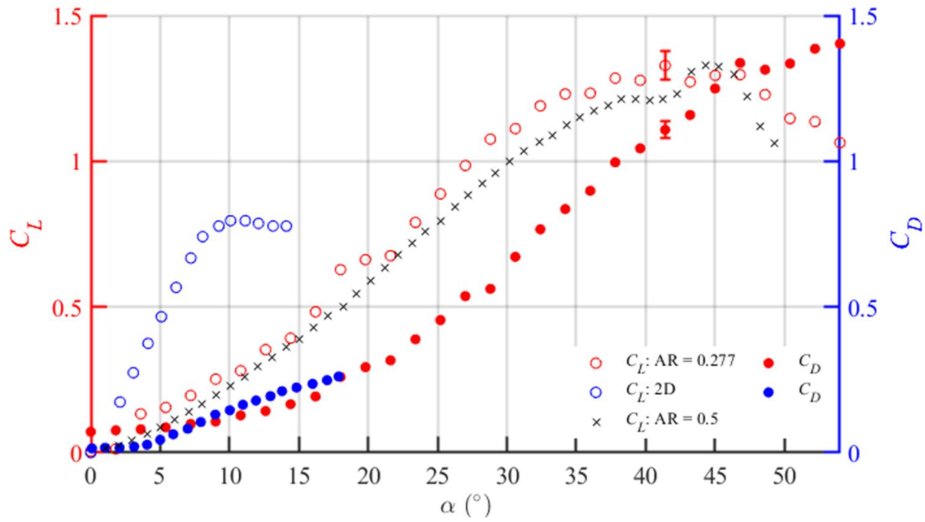

Figure 4.1: Force measurements (lift coefficient C_L, left Y-axis and drag coefficient C_D, right Y-axis) of the wing at different AoAs. The hollow and solid red circles indicate the C_L and C_D of our low AR wing, respectively, which is compared with that of the 2D thin aerofoil (hollow and solid blue circles) from Pelletier and Mueller (2000) ($Re = 10^5$) and the C_L of a wing with an AR of 0.5 (black $\times$) from Torres and Mueller (2004) at $Re = 10^5$. The error bar indicates a standard deviation of the present experimental uncertainty.

4.2 Overview of the flow around a very low AR wing

The lift coefficient $C_L = F_L/\frac{1}{2}\rho U_\infty^2 A$ and drag coefficient $C_D = F_D/\frac{1}{2}\rho U_\infty^2 A$ of a low-aspect-ratio thin wing at different AoAs are shown in Fig. 4.1, where ρ is the air density, A is the plane area of wing. Uncertainties in force measurements are on the order of 5% and 3% for C_L and C_D, respectively, which are shown by error bars in Fig. 4.1. It is known that the lift coefficient C_L of a 2D aerofoil has a constant lift slope for small AoAs (Pelletier and Mueller, 2000). However, the highly nonlinear lift curve can be seen on the low AR wing. Meanwhile, comparing to the 2D case, both the stall angle and the C_L of the low AR wing are greater although it requires a high AoA to get the same C_L as the 2D wing. Similar results were obtained by Torres and Mueller (2004), showing almost the same trend only with a small difference in the stall angle due to different ARs. The delayed stall angle seems to be due to the existence of the TV which can affect the flow structure on a low AR wing (Fig. 4.2). The C_D on the low AR wing stays low until $\alpha = 8°$ before increasing fast until the stall angle.

Three velocity components (U, V and W) from two separate PIV measurements are combined together to show quasi-3D flow fields around a low AR thin wing. Vortical structures from $\alpha = 0°$ to $\alpha = 50.4°$ are shown in Fig. 4.2. These vortical structures are identified by the iso-surface of λ_2-criterion (Jeong and Hussain, 1995) representing 4% of its maximum value. It has been confirmed that this choice of the λ_2 does not affect the identification of vortices in this work after testing various λ_2 values. The freestream velocity is along the x-axis from left to right in this figure, where the pink and the cyan-blue colours represent the LEV and the TV, respectively. Note that, the TV is identified by V- and W-component velocities while the LEV is by U- and V-component velocities in each PIV measurement. With an increase in the AoA, the separated flow at the wing tip moves from the pressure side to the suction side, resulting in a TV. Meanwhile, a LEV can be observed near the leading-edge, accompanying a recirculation area. Low pressure on the wing surface can be created by the TV and the LEV to enhance the lift on a wing (Madnia, 2010).

For a 2D or a large AR aerofoil, the stall angle is generally less than 20° (Storms and Jang, 1994; Rossow, 1978; Mueller and Batill, 1982). With an increase in the AoA, the flow will start to separate and this separation point will move towards the leading-edge, and then the lift is decreased. Interestingly, a stronger LEV can be observed on a low AR wing. The existence of this TV is thought to induce velocity to suppress the leading-edge separation, which maintains the LEV (Taira and Colonius, 2009; Winter, 1936; Jian and Ke-Qin, 2004). At a small AoA the LEV is small and nearly

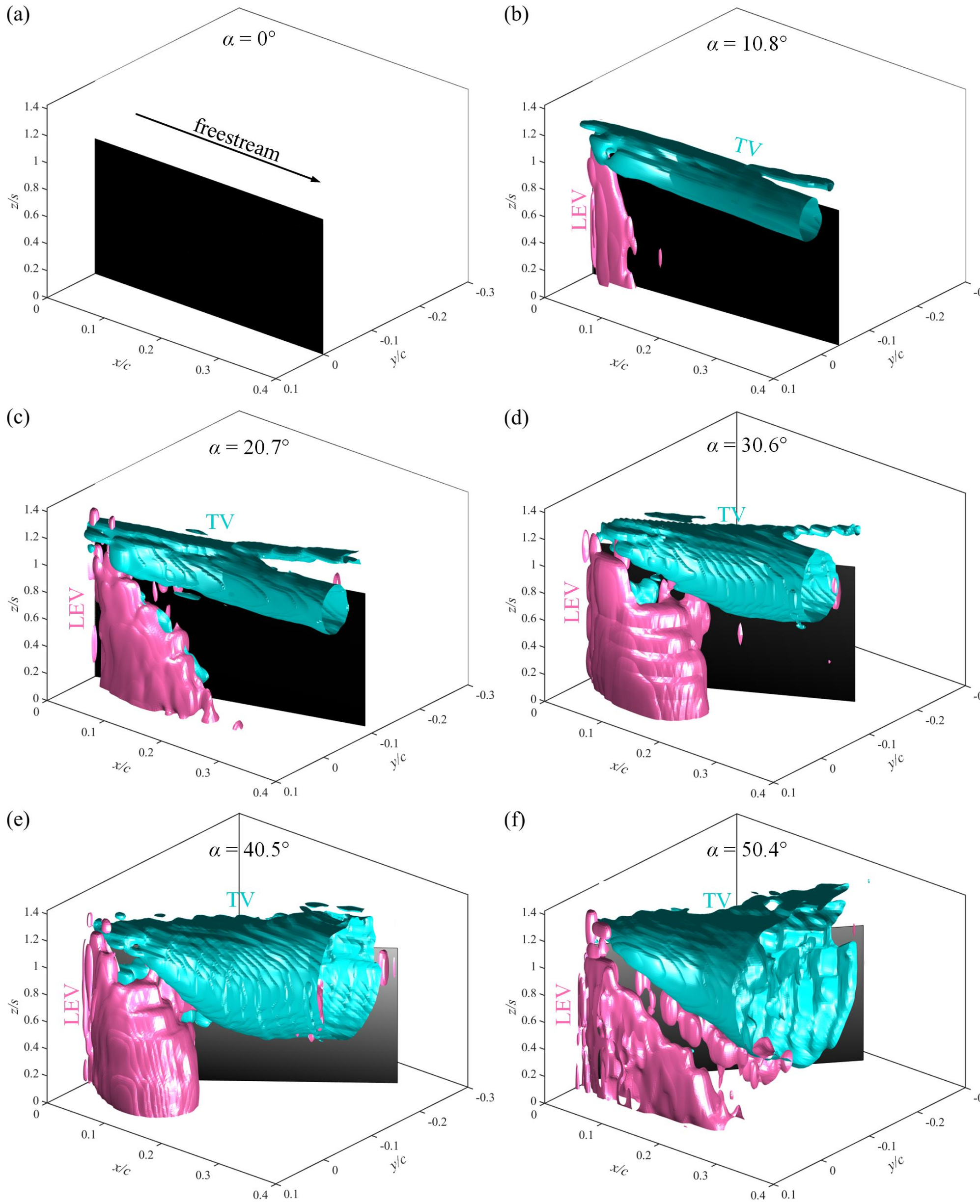

Figure 4.2: Vortical structures at different AoAs ($\alpha = 0°$ to $50.4°$) from present PIV measurements. The flow is from left to right along the x-axis. Pink iso-surface indicates the LEV while cyan-blue structure indicates the TV at $\lambda_2 = -6 \times 10^4$.

uniform in spanwise direction, see Fig. 4.2b. With an increase in the AoA, the volume of both the LEV and the TV increases (Figs. 4.2c and 4.2d). Near the stall angle the TV starts to expand as shown in Fig. 4.2e and finally detaches from the wing surface at $\alpha = 50.4°$ (Fig. 4.2f). In the following, the characteristics of the LEV along the span will be studied by investigating how the TV affects the separated flow and delays the stall.

4.3 Details of the LEV on a very low AR wing

The non-dimensional spanwise vorticity ($\omega_z c/U_\infty$) superimposed on velocity vectors in the x-y plane at different AoAs along the span is shown in Fig. 4.3. Yellow solid lines and points are the LEVs and their centroids, respectively, which are identified by the λ_2 criterion. Although this criterion may not distinguish the multiple adjacent vortices (Jiang et al., 2005), it is useful in our study to understand the interaction between the TV and the LEV. Note that the contour of λ_2 here indicates the LEV as well as the shear layer. The thin wing is shown by the thick black line. The chord position of flow structures can be identified by white markers, which are shown at every 10% chord length along the wing. For small values of AoAs at the mid-span, the LEV can hardly be identified, since the flow is dominated by a shear layer represented by negative vorticity as shown in Fig. 4.3a. With an increase in the AoA from $\alpha = 20.7°$ to $\alpha = 40.5°$ at the mid-span ($z/s = 0$), the boundary layer separates at the leading-edge and then reattaches to the wing surface, at $x/c = 0.24$ at $\alpha = 30.6°$ (see Fig. 4.3i) and at $x/c = 0.2$ at $\alpha = 40.5°$ (see Fig. 4.3m). This creates a recirculation zone, whose size increases with α. Here, the LEV is clearly identified at

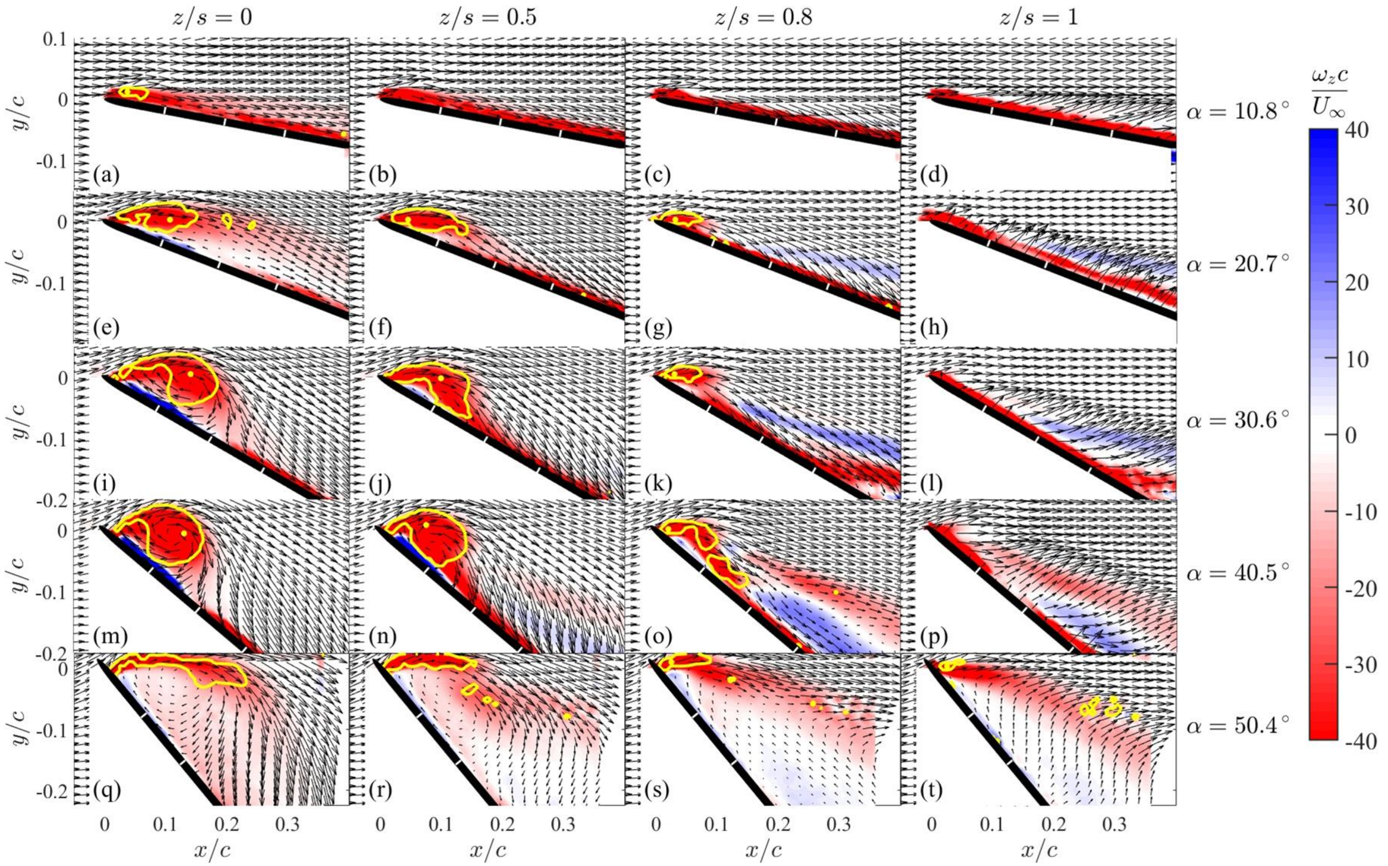

Figure 4.3: Vorticity field superimposed on the velocity vectors along the span from $z/s = 0$ to $z/s = 1$ at five AoAs ($\alpha = 10.8^\circ$ to 50.4°). The solid yellow lines and points in figure indicate the LEVs and the centroids of the LEVs identified by the λ_2-criterion, respectively. White markers are shown at every 10% chord length along the wing.

$\alpha = 30.6°$ and $\alpha = 40.5°$ as shown in Figs. 4.3i and 4.3m. Downstream of the LEV, the vorticity field is dominated by the wall shear due to the induced velocity by the TV. Moving away from the mid-span, the flow field does not make significant change at $\alpha = 10.8°$. With an increase in the AoA, the separation region becomes smaller and finally vanishes at the wing tip ($z/s = 1$). At the same time, the LEV centroid moves towards the leading-edge, see Figs. 4.3g, 4.3k and 4.3o. Although, the induced velocity by the TV helps reattach the separated flow (Taira and Colonius, 2009; Winter, 1936; Jian and Ke-Qin, 2004), how such an induced velocity controls the separated flow along the span is not fully understood. This will be discussed later.

The time-averaged velocity field as shown in Fig. 4.3 demonstrates that the separated flow can be suppressed and reattached to the wing surface, forming a compact LEV. To investigate the interplay between the LEV and TV, the turbulence intensity of u' ($u' = \sqrt{\overline{u^2}}/U_\infty$) and v' ($v' = \sqrt{\overline{v^2}}/U_\infty$) and the Reynolds stress ($-\overline{uv}/{U_\infty}^2$) superimposed by the streamlines are shown in Figs. 4.4, 4.5 and 4.6, respectively. There is a large turbulence intensity region near the leading edge, indicating a strong shear layer. Interestingly, the largest streamwise turbulence intensity can be observed at $\alpha = 30.6°$. The flow behaviour over a low AR wing can be determined by the balance between the flow separation at the leading-edge (negative effect) and the induced velocity by the TV (positive effect), both of them are a function of the AoA. At small AoAs ($\alpha = 10.8°$ and $\alpha = 20.7°$), the TV is weak, so it cannot help reattach the separated flow completely. Some velocity fluctuations can still be observed even at $x/c = 0.4$. With an increase in the AoA, the strength of the TV is increased, suppressing the leading-edge separation by its induced velocity. This is clearly seen in Fig. 4.5, where velocity within the leading-edge shear layer is turned towards

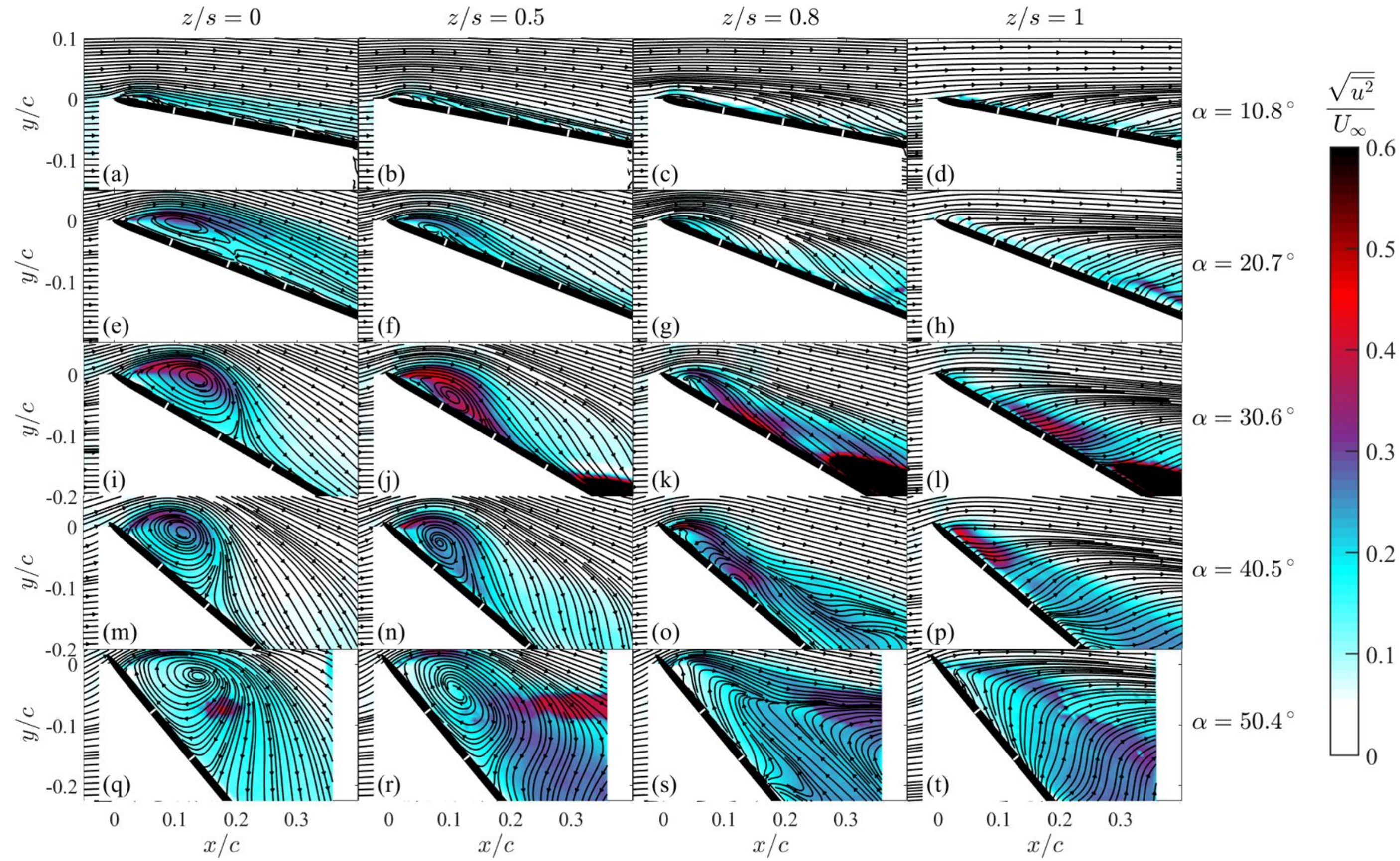

Figure 4.4: Non-dimensional turbulent intensity $u' = \sqrt{u^2}/U_\infty$ superimposed on the streamlines along the span from $z/s = 0$ to $z/s = 1$ at five AoAs ($\alpha = 10.8^\circ$ to 50.4°). White markers are shown at every 10% chord length along the wing.

the wing surface with a strong region of v' on the perimeter of the LEV.

Near the stall angle, the intense leading-edge separation cannot be managed by the induced velocity of the TV anymore, so the flow starts to separate and a large wake region can be seen in Fig. 4.4q. Moving from mid-span to the tip-edge ($z/s = 1$), there is a strong interaction between the separated flow and the TV, generating intense velocity fluctuations near the leading edge as shown in Figs. 4.4k and 4.4o as well as in Figs. 4.5k and 4.5o. While the u' is generated by the shear layer, the increase in v' is predominantly due to the induced velocity of the TV. The strongest v' is observed close to the reattachment point of the separated flow.

The turbulent mixing in the shear layer developing from the leading-edge and near the flow attachment region can be indicated by the Reynolds stress ($-\overline{uv}/U_\infty^2$) in Fig. 4.6. At the mid-span, the Reynolds stress increases and reaches its peak along the chord, and then decreases downstream at all AoAs, which is similar in behaviour to backward facing step flows (Chandrsuda and Bradshaw, 1981). This is due to the development of a shear layer from the leading-edge, which could involve shedding vortices. Moving from the mid-span to the tip-edge, the flow reattachment regions have large Reynolds stress, see Figs. 4.6j, 4.6n, 4.6k and 4.6o, which was not observed in backward facing step flows (Chandrsuda and Bradshaw, 1981). These should be due to the interaction between the LEV and TV, since these areas correspond to the edge of TV cores, see Figs. 4.8.

To clarify the contribution of the LEV on the total lift, the non-dimensional circulation $\Gamma_L/U_\infty c$ along the span of the negative vorticity inside of the LEV is shown in Fig. 4.7. Only the results at $\alpha = 20.7°$, $\alpha = 30.6°$ and $\alpha = 40.5°$ are shown, where the LEV can be clearly observed. With an increase of AoA, the circulation of the LEV increases and contributes

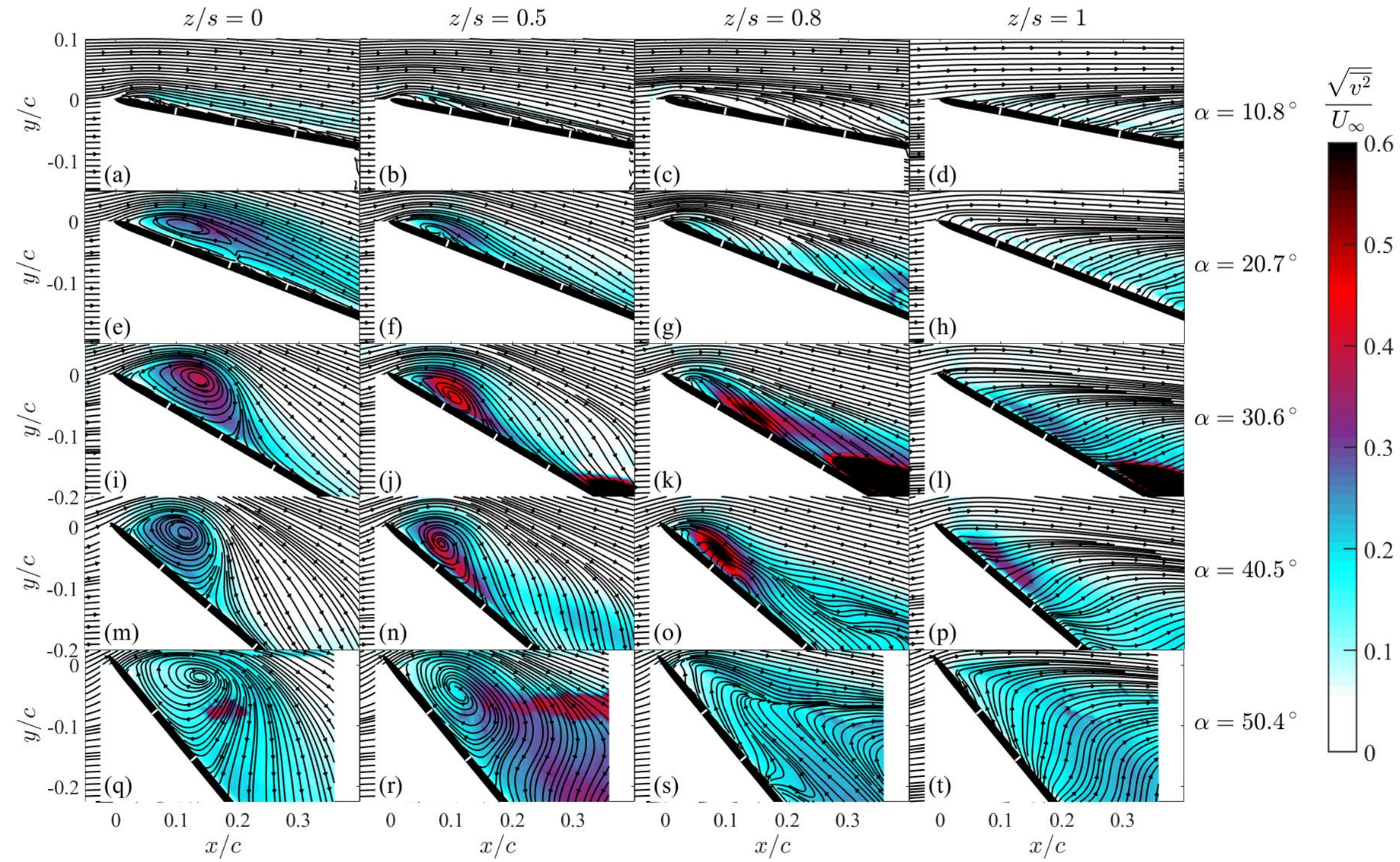

Figure 4.5: Non-dimensional turbulent intensity $v' = \sqrt{\overline{v^2}}/U_\infty$ superimposed on the streamlines along the span from $z/s = 0$ to $z/s = 1$ at five AoAs ($\alpha = 10.8^\circ$ to 50.4°). White markers are shown at every 10% chord length along the wing.

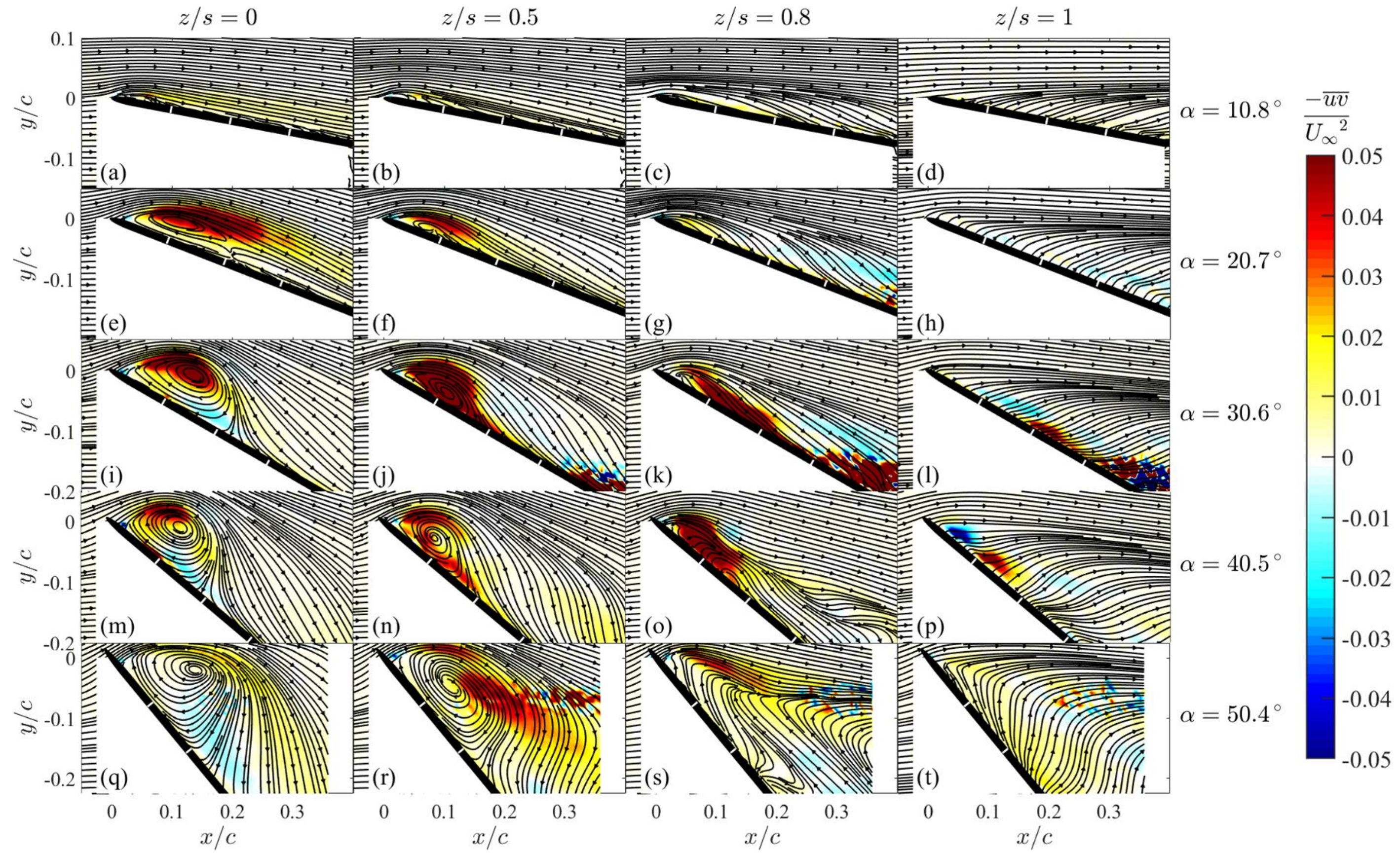

Figure 4.6: Non-dimensional Reynolds stress $-\overline{uv}/{U_\infty}^2$ superimposed on the streamlines along the span from $z/s = 0$ to $z/s = 1$ at five AoAs ($\alpha = 10.8°$ to $50.4°$). White markers are shown at every 10% chord length along the wing.

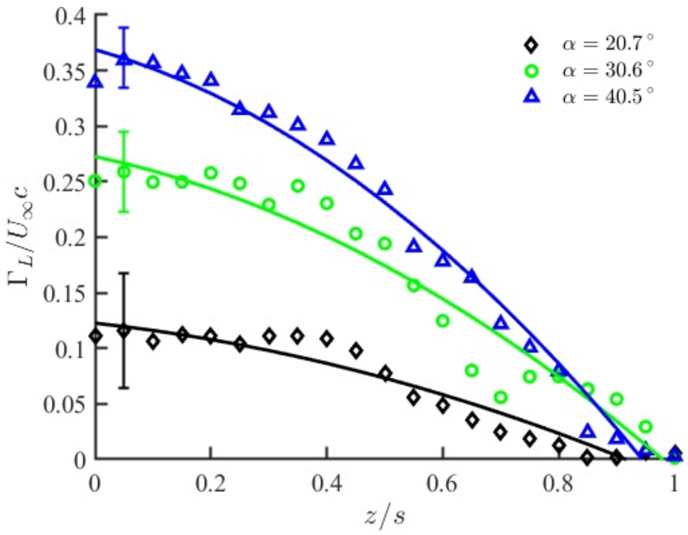

Figure 4.7: Non-dimension LEV circulation ($\Gamma_L/U_\infty c$) of a thin wing along the span from $\alpha = 20.7°$ to $\alpha = 40.5°$. The error bar indicates a standard deviation of the measurement uncertainty.

to the lift on the wing, although it collapses to zero at $z/s = 1$ at all AoAs. A similar change of the LEV circulation from the mid-span to the wing-tip has been shown by DeVoria and Mohseni (2017a) and Yilmaz and Rockwell (2012). The contribution of the LEV to the total lift was estimated by applying the Kutta-Joukowski's lift theorem on Γ_L, assuming that the LEV circulation distribution on the other half-span (unmeasured) is identical with the measured half-span as shown in Fig. 4.7. Results show that the LEV plays an important role on total lift, contributing $27 \pm 7\%$ for $\alpha = 20.7°$ to $40.5°$.

4.4 Details of the TV on a very low AR wing

Figure 4.8 shows the non-dimensional streamwise vorticity ($\omega_x c/U_\infty$) superimposed on the velocity vectors along the chord in the y-z plane at five AoAs. The solid yellow lines and points indicate the TVs and the centroids of the TVs, respectively, identified by λ_2 criterion. The black rectangles indicate the wing profile viewed from downstream, where the upstream sec-

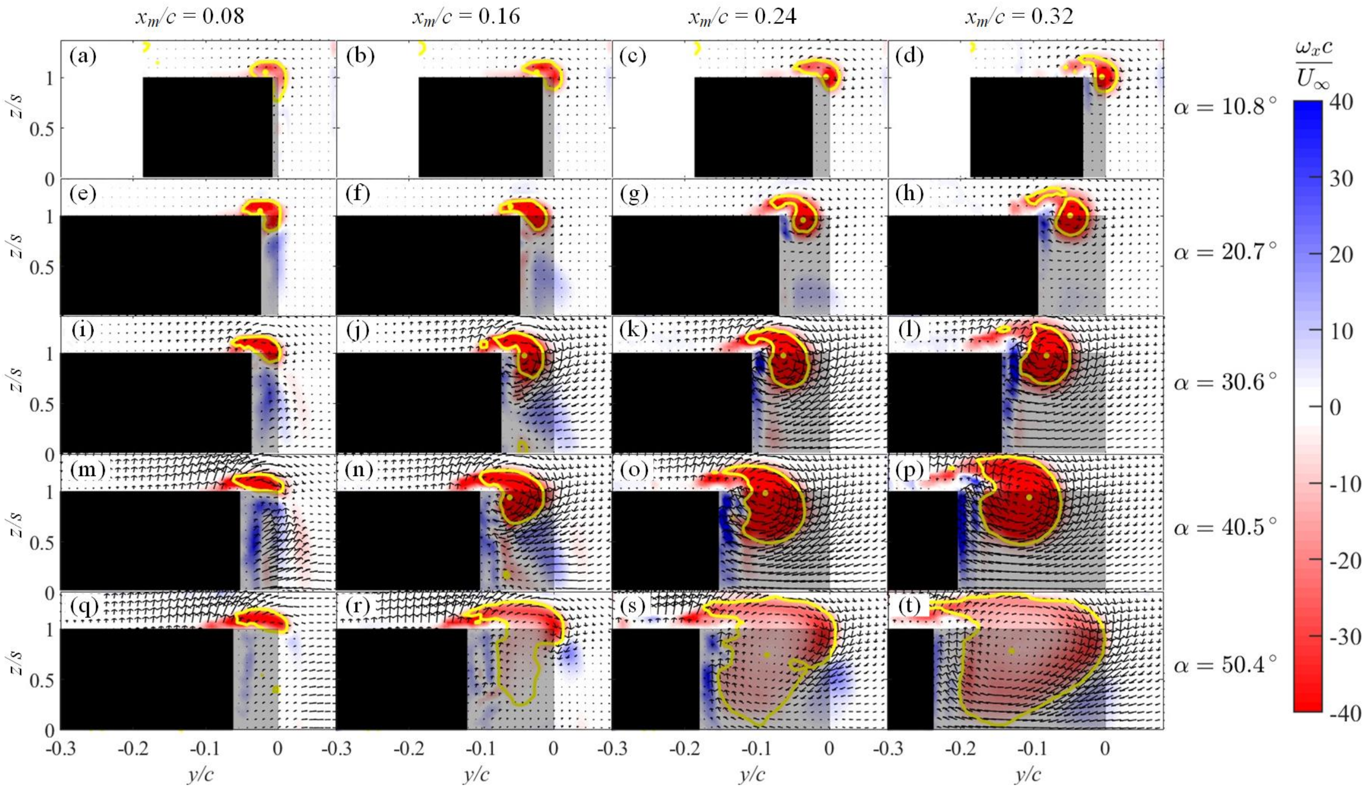

Figure 4.8: Vorticity fields superimposed on the velocity vectors at different distance to leading-edge along the chord at five AoAs ($\alpha = 10.8°$ to $50.4°$). The yellow lines and points in figure indicate the TVs and the centroids of the TVs identified by the λ_2-criterion, respectively.

tion is made translucent to show the flow field. The velocity vector near the tip-edge moves from the pressure side (left-hand side of the figure) to the suction side (right-hand side of the figure) due to the imbalance of the pressure on the wing surfaces. At a short downstream distance from the leading-edge, the TV is about to form, where the velocity magnitude is still very small as shown in Figs. 4.8a, 4.8e, 4.8i, 4.8m and 4.8q. Meanwhile, another flow motion from the mid-span towards the tip-edge can be found between $z/s = 0$ and $z/s = 0.7$, which originates from the LEV. The maximum velocity of this flow can reach to the freestream value near the stall angle as the LEV develops. In Figs. 4.8j at $\alpha = 30.6°$ and 4.8n at $\alpha = 40.5°$, the swirling velocity induced from the TV helps the separated flow reattach to the wing surface. With an increase in the distance to the leading-edge, the velocity associated with the LEV reduces under the effect of the TV as shown in Figs. 4.8k and 4.8o. Moving from the leading-edge towards the trailing-edge of the thin wing, TV's swirling area indicated by a constant streamwise vorticity enlarges together with its velocity magnitude. We can also observe that the area as well as the velocity magnitude of the swirl is increased with an increase in the AoA before the stall angle. For instance, at $x_m/c = 0.32$, the swirling area only occupies a quarter of the half-span with the maximum velocity similar to the freestream value at $\alpha = 20.7°$. However, the swirling area increases to 50% of the half-span with the maximum velocity of 1.5 times the freestream value at $\alpha = 40.5°$. This is one of the reasons why the stall angle of the low AR flat plate is as high as $\alpha = 42°$.

Some other vorticities are seen between $z/s = 0$ and $z/s = 1$, which seem to come from the interaction of the TV with the LEV. The strength of those vorticities becomes much more intense at $\alpha = 40.5°$ with an increase in the LEV strength, see Fig. 4.7. Moving downstream, the negative vorticity

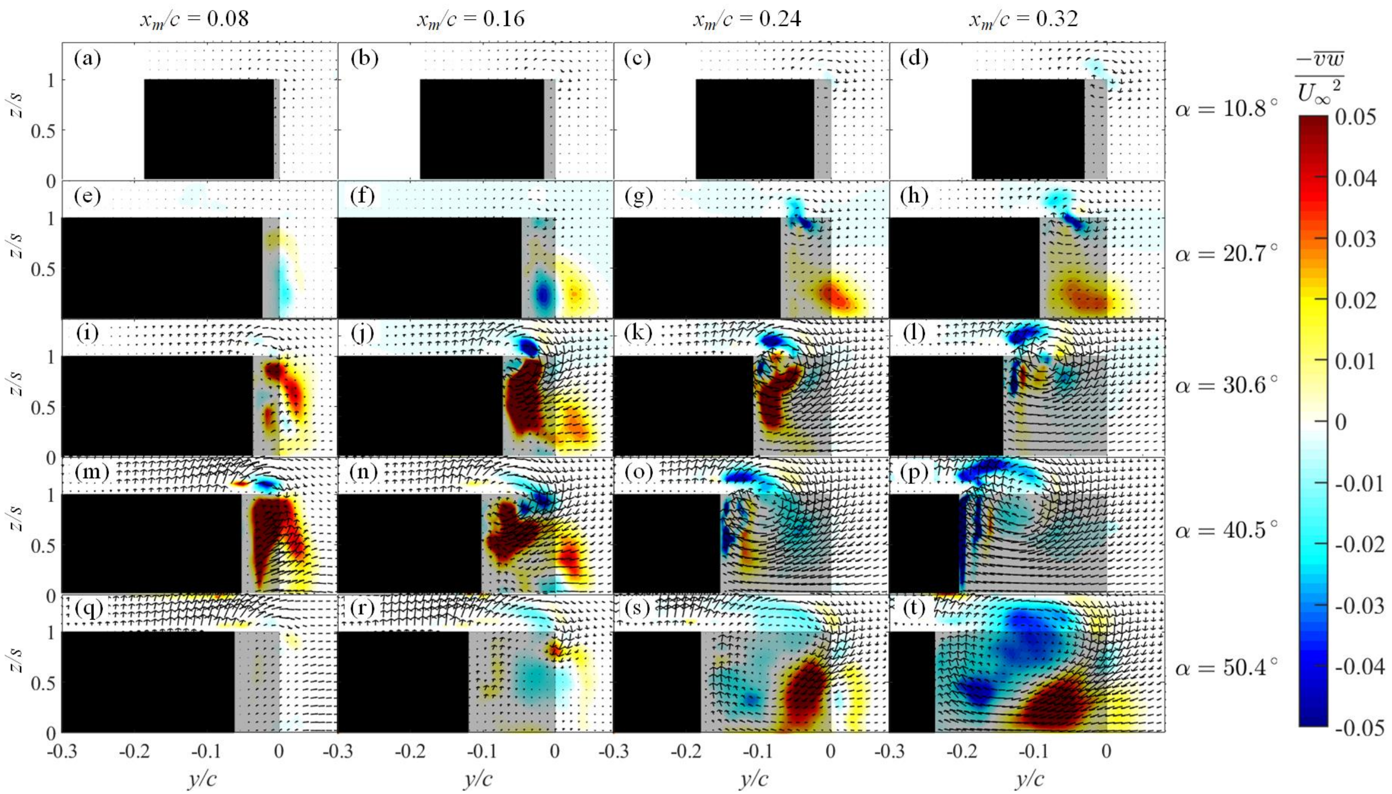

Figure 4.9: Non-dimensional Reynolds stress $-\overline{vw}/U_\infty{}^2$ superimposed on the velocity vectors along the chord at five AoAs ($\alpha = 10.8^\circ$ to 50.4°).

of the TV near the tip increases, inducing the secondary vorticity at the wing surface. Figures 4.8j at $\alpha = 30.6°$ and 4.8n at $\alpha = 40.5°$ indicate that the vorticity produced by the TV is extended from the tip towards the mid-span. Although the TV becomes greater in size at $\alpha = 50.4°$, the vorticity strength inside is much weaker than that at other AoAs. It is also moving away from the wing surface downstream.

The Reynolds stress ($-\overline{vw}/{U_\infty}^2$) in the y-z plane is presented in Fig. 4.9. The areas of high Reynolds stress are around the edge of the TV core, indicating an interaction between the LEV and the TV. Downstream of the leading-edge, the Reynolds stress is reduced progressively without LEV, see Figs. 4.9l and 4.9o. At a small AoA, very weak Reynolds stress can be observed near the leading-edge, which is due to the weak LEV and TV. With an increase in the AoA, the TV becomes stronger, resulting in a greater turbulent mixing indicated by the high Reynolds stress shown here. After the stall at $\alpha = 50.4°$, a large separation area develops. Here, an intense interaction between the TV and the separated flow can be observed at $x_m/c = 0.24$ and $x_m/c = 0.32$ in Figs. 4.9s and 4.9t, respectively, showing a stronger mixing layer.

The Reynolds stress can still be observed inside the TV, which might be due to the effect of the vortex core wandering. Probability density functions (PDF) of 400 instantaneous TV centroids along the y-axis and z-axis at a distance of $0.35c$ along the wing chord from the leading-edge at three AoAs are presented in Fig. 4.10 to show this phenomenon, where $\triangle y$ and $\triangle z$ are the centroid distance between the instantaneous and the time-averaged TV. The probability density function of TV centroids are well represented by a Gaussian distribution (see Fig. 4.10), where the standard deviation (σ) increased with an increase in the AoA. Here, the location of maximum probability has been slightly affected by the size of interrogation

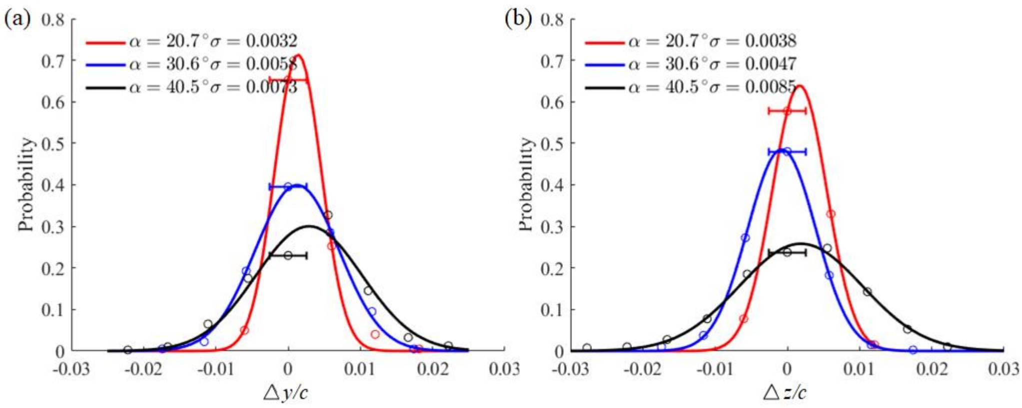

Figure 4.10: Probability density functions of the 400 instantaneous TV centroid at $0.35c$ from the leading edge along the wing chord at three AoAs: (a) the wandering of the TV centroid along the y-axis; (b) the wandering of the TV centroid along the z-axis. The error bar indicates the size of interrogation area for the calculation of PDF.

area ($0.0025c \times 0.0025c$) during the PIV analysis. This suggests that the degree of vortex wandering increases with the angle of attack, causing a higher C_L fluctuation at a higher AoA.

The non-dimensional streamwise circulation $\Gamma_T/U_\infty c$ of the TV is shown in Fig. 4.11 for $\alpha = 10.8°$ to $\alpha = 50.4°$. At $\alpha = 0°$, Γ_T is nearly zero because there is no TV. With an increase in the AoA until the stall Γ_T increases monotonically. The figure also shows that the Γ_T increases downstream. This suggests that a low AR thin wing is similar to a delta wing (Gordnier and Visbal, 1994; Ma et al., 2017), where the circulation of the TV increases linearly with a downstream distance (Visser and Nelson, 1993; Traub, 1997). We can fit the experimental data as $\Gamma_T/U_\infty c = 3.72\alpha_r^{2.1} x/c$ up until the maximum lift angle, where α_r is the AoA in radians, see solid lines in Fig. 4.11. The relationship between the circulation and angle of attack is linear only for a small angle of attack. At a large AoA, there is an intense interaction between the TV and LEV for $x/c < 0.12$, therefore the growth of circulation near the leading edge is different from the rest. After the stall angle, the LEV becomes weaker, but the rate of increase in

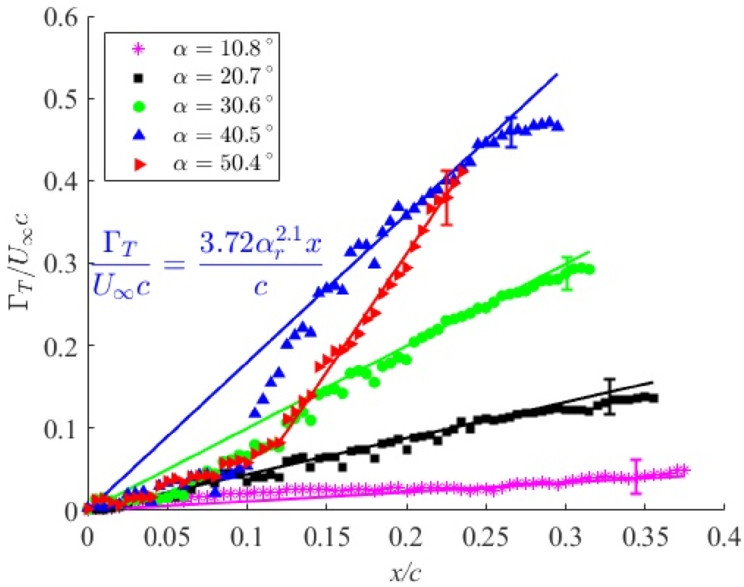

Figure 4.11: Streamwise circulation Γ_T along x-axis from $\alpha = 10.8°$ to $50.4°$, the fitted curves ($\Gamma_T/U_\infty c = 3.72\alpha_r^{2.1}x/c$) are shown in solid lines. The error bar indicates a standard deviation of the measurement uncertainty.

circulation becomes greater downstream, however, as can be seen in Fig. 4.11.

In order to characterise the development of the TV, the distance of the TV centroid to the wing surface and the TV diameter (D) were obtained and shown in Fig. 4.12 in non-dimensional form. Figure 4.12a shows that the non-dimensional distance of the TV centroid to the wing (y_c/c) changes almost linearly along the chord, which can be represented by $y_c/c = 0.56e^{2.3\alpha_r}x/c$. Here, the vortex diameter is calculated by $D = 2 \times \sqrt{S_{\mathrm{TV}}/\pi}$, where S_{TV} is area of the vortex core identified by λ_2, which is shown in Fig. 4.8. The non-dimensional diameter of the TV increases with an increase in the AoA, which can be fitted to an expression given by $D/c = 0.027e^{2.78\alpha_r}\sqrt{x/c}$, see Fig. 4.12b. This relationship is expected since the circulation of the TV with a constant vorticity core is proportional to D^2, which linearly increases with x/c as shown in Fig. 4.11. Near the leading-edge, the development of the TV is affected by the LEV, therefore,

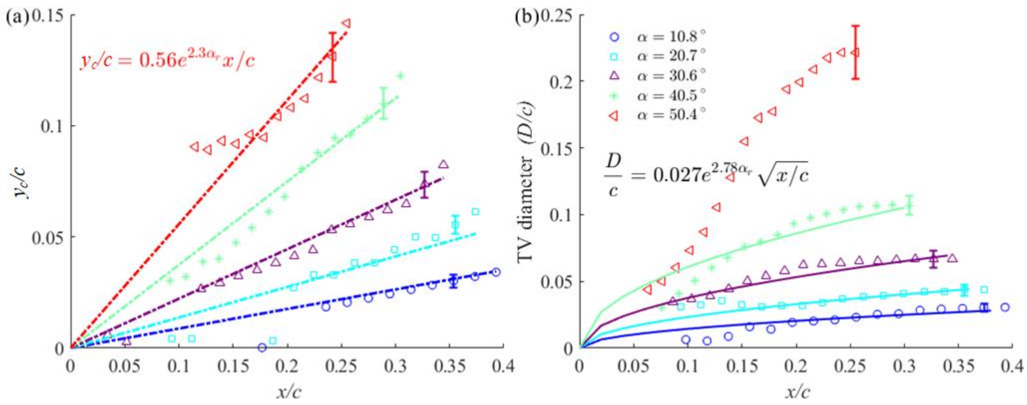

Figure 4.12: TV's centroid positions (a) and diameters (b) along x-axis at different AoAs. The error bar indicates a standard deviation of the measurement uncertainty.

the data do not fit to these expressions very well. We expect the proportional constants in the expressions for y_c/c and D/c are function of the AR of the wing as well as the Re. It is noted that the TV diameter increases much faster after the stall angle.

4.5 The induced velocity of the TV

We showed in Figs. 4.2 and 4.3 that the flow separates at the leading-edge and then reattaches to the wing surface, forming the LEV. To quantify the flow behaviour of this leading-edge separation region, we define the separation length (SL) as the distance between the leading-edge and the reattachment point along the wing chord where the probability of forward flow and reversed flow becomes equal (Kasagi and Matsunaga, 1995). This is shown in Fig. 4.13 along the span. Only results at three AoAs are presented here, where the separation region can be identified unambiguously. The non-dimensional separation length SL/c takes maximum at the mid-span ($z/s = 0$) and reduces to zero towards the tip edge. At a small angle of attack ($\alpha = 20.7°$), SL/c reduces nearly linearly with z/s. With an increase in the AoA, however, the rate of reduction in SL/c with z/s is less

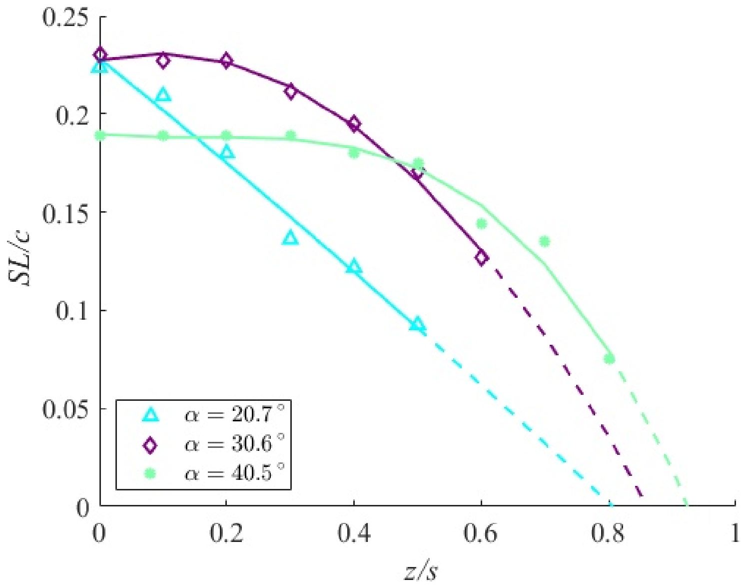

Figure 4.13: Separation length and the reattachment point along the span from $\alpha = 20.7°$ to $40.5°$.

as shown in Fig. 4.13, although the maximum value in SL/c is smaller. The induced velocity of the TV helps suppress the separation around the leading-edge for a low AR wing, thereby increasing the maximum lift angle to 42° (see Fig. 4.1).

In order to investigate how the leading-edge flow separation is influenced by the TV, the induced velocity V_d at three AoAs is computed and presented in Fig. 4.14 together with the streamlines near the leading-edge. Here, we assumed that the TV can be represented by a Rankine vortex and neglected the interaction between the TV and LEV near the leading edge. There is a strong correlation between the reattachment point and the region of large induced velocity in Fig. 4.14. In other words, the reattachment point moves upstream with an increase in the induced velocity. The variation of the span-averaged value of induced velocity V_{davg} along the streamwise direction is presented in Fig. 4.15 together with the reattachment points of the LEV. The results in the figure show that the spanwise-averaged induced velocity is given by $(0.16 \pm 0.032)U_\infty$ at $\alpha = 20.7°$, while it is $(0.39 \pm 0.023)U_\infty$ at $\alpha = 30.6°$ and $(0.59 \pm 0.037)U_\infty$ at $\alpha = 40.5°$. These

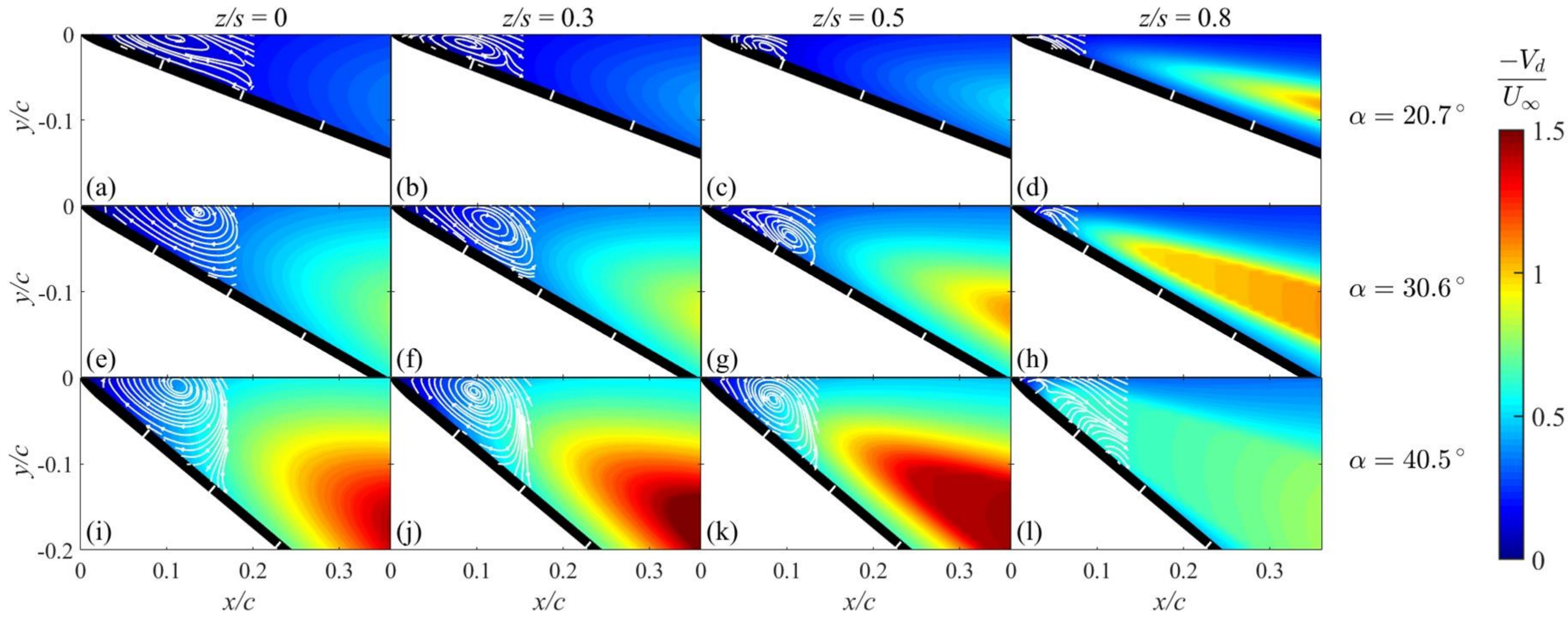

Figure 4.14: The induced velocity distribution superimposed on the separated flow streamlines (white colour) from the mid-span ($z/s = 0$) to tip-edge ($z/s = 0.8$) at $\alpha = 20.7°$, $\alpha = 30.6°$ and $\alpha = 40.5°$. White markers are shown at every 10% chord length along the wing and the colour bar on the right applies to all plots.

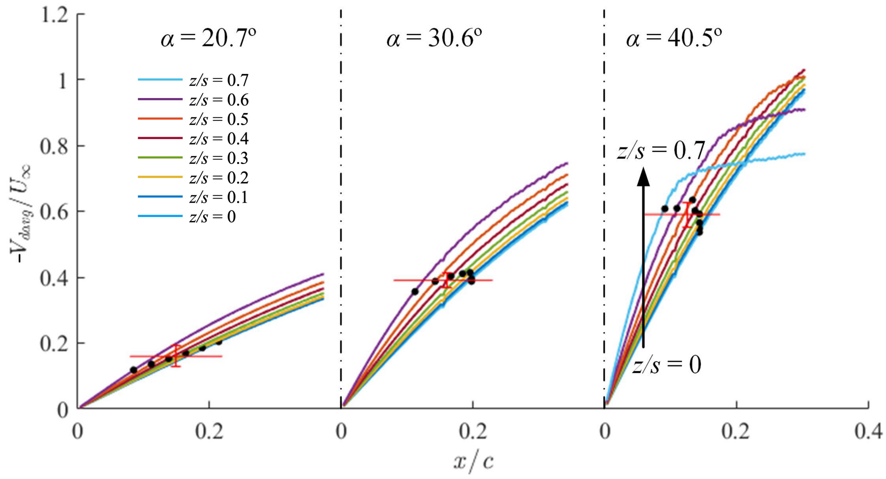

Figure 4.15: Variations of the spanwise-averaged induced velocity from $z/s = 0$ to $z/s = 0.7$ at $\alpha = 20.7°$, $\alpha = 30.6°$, and $\alpha = 40.5°$. The solid points indicate the reattachment points along the span.

results suggest that the induced velocity of the TV should reach a certain required value in order to suppress a leading edge flow separation. With an increase in the AoA, this required value of induced velocity increases due to an increased separation region. When the induced velocity of the TV cannot reach the required value with a further increase in the AoA, the separated flow cannot be reattached, resulting in the stall (Figs. 4.3q–t).

Overall, the fundamental reason for a high C_L and a large stall angle on a low AR wing is that the induced velocity from TV can suppress and reattach the separated flow near the leading edge. This results in a formation of LEV which has an important contribution to the lift. With an increase in the AoA, the induced velocity due to TV increases, which can suppress and reattach the separated flow more efficiently. Our result should help design MAVs that require a large stall angle and better understand the flight physics of natural flyers, such as fruit flies, whose wings have low AR.

Chapter 5

Vortical structures over a very low AR wing under pitching motion

5.1 Introduction

In the previous chapter, we have studied the interaction between the TV and the LEV over a very low AR wing, where the influence of the TV on the development of the LEV was demonstrated (Dong et al., 2020). Building on the understanding of the vortex interactions gained from this study, we investigate the effect of the pitching motion on the development of vortical structures over a very low AR wing at $K = 0, 0.003, 0.01, 0.03$ and 0.08 in this chapter, by examining the relationship between the vortex behaviour and the aerodynamic forces. Three-dimensional flow fields around the pitching wing are constructed by velocity measurements using high-speed PIV. The development of the TV and LEV at different pitch rates is quantified by carefully documenting their shapes, locations and trajectories

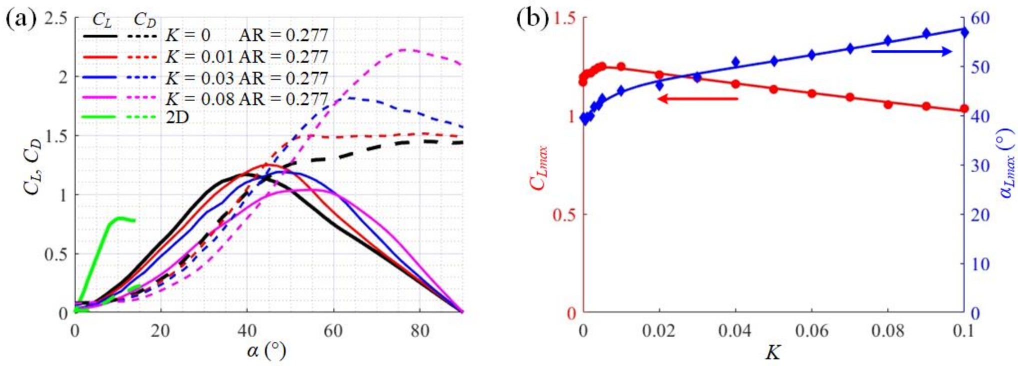

Figure 5.1: The aerodynamic characteristics of a very low AR flat-plate wing as a function of AoA and the pitch rate: (a) the lift coefficient C_L and the drag coefficient C_D as compared with those of a stationary 2D thin flat plate ($Re = 10^5$) by Pelletier and Mueller (2000); (b) the maximum lift coefficient C_{Lmax} and the maximum lift angle α_{Lmax}.

as well as vorticity distributions and circulations. The self-similarity of the aerodynamic forces and vortical structures over pitching wings is obtained using phase-lag adjusted AoA. Finally, the behaviour of the LEV during the pitching motion in delaying flow separation is studied in the light of the induced velocity of the TV, which is confirmed by the Biot-Savart law.

5.2 Aerodynamic forces on a pitching wing

Figure 5.1a shows the lift coefficient C_L and the drag coefficient C_D of a thin flat-plate wing with a very low AR (AR = 0.277). Here, the C_L of this very low AR wing is compared with that of a 2D plate wing at $Re = 10^5$ since we could not find many experimental data for a 2D flat plate at high Reynolds numbers, certainly not at $Re = 3 \times 10^6$. We believe, however, the C_L characteristics near the maximum lift angle will not change significantly with the Reynolds number once the flow is separated from the sharp leading edge of the flat plate. Although the lift coefficient C_L of the stationary case ($K = 0$) is very small at small AoAs (Lamar, 1974) as compared with a 2D thin plate (Pelletier and Mueller, 2000), the C_L slope increases with an increase in the AoA up to $\alpha = 30°$ and the C_L eventually reaches a maximum lift coefficient of $C_L = 1.18$ which is 40% greater than that of a 2D flat plate. Then, the lift coefficient C_L gradually reduces with a further increase in the AoA, returning to zero at $\alpha = 90°$. The drag coefficient C_D of the stationary thin flat-plate wing, on the other hand, increases with increasing AoA all the way up to $\alpha = 90°$. Here, the C_D slope increases with the AoA from $\alpha = 0°$ to the maximum lift angle of $\alpha = 40°$. Thereafter the rate of increase in C_D reduces until $\alpha = 90°$, where the maximum drag coefficient of $C_D = 1.43$ is observed.

Applying pitch motion, the maximum lift angle α_{Lmax} of a very low AR thin plate is increased with increasing pitch rate K, see Fig. 5.1b. On the other hand, the maximum lift coefficient C_{Lmax} is reduced with pitching motion, although there is a small increase in C_{Lmax} for a small value of pitch rate $K < 0.04$. This is due to the very low AR wing being studied here. While Gendrich (1999) and Granlund et al. (2013) demonstrated the lift enhancement on pitching wings with the aspect ratio with AR = 4 and 6, respectively, we have used a very low AR wing (AR = 0.277) in this investigation. Similar to the lift curve, the drag curve is shifted to the right (towards the larger α) with pitch motion, as shown in Fig. 5.1a, where the maximum drag coefficient C_D is increased with an increase in the pitch rate K. There is no sign of lift or drag spikes due to the wing acceleration at the start ($\alpha = 0°$) and the end ($\alpha = 90°$) of pitching since the pitch motion is carried out at a mid-chord pivot in this study (Granlund et al., 2013).

The lift coefficient C_L for a very low AR thin plate, as shown in Fig. 5.1a, is reasonably well represented by an empirical formula $C_L = A_L \sin 2\alpha$ proposed by Strickland and Graham (1986), where A_L depends only on the pitch rate K. Granlund et al. (2013) suggested a multiplication factor of $(0.75 - x_p)K$ to this formula, where x_p is the non-dimensional pivot position along the chord, indicating that the effect of the pitch rate K on C_L is zero only if the pivot is located at the 75% chord (Leishman 2006). Despite the mid-chord pivot location, our results do not show any effect of the pitch rate K, suggesting that a different flow physics is at play for very low AR pitching wing aerodynamics. This will be explored in the following sections.

5.3 Effect of pitching motion on the vortical structures

Progressive development of the vortical structures over the upper half of the wing near the leading edge ($x_m/c < 0.52$) is depicted in Fig. 5.2 for $K = 0$ and 0.08 as a function of the AoA, which is identified by the λ_2-criterion (Jeong and Hussain, 1995). Here, the TV (shown in cyan) and the LEV (shown in red) are measured separately on y-z planes and x-y planes, respectively, which are shown together in Fig. 5.2 to present the whole vortical field over a very low AR wing under pitching motion. Note that, the viewing angle changes with the AoA to stop the vortical structures blocking the view. A flat-plate wing model is shown in black, where the freestream is from left to right in the figure. The baseline case ($K = 0$) at $\alpha = 60°$ and $\alpha = 70°$ is not included here due to a global flow separation already taking place at these AoAs. For the baseline case, the sequence of images indicates that a TV is being developed along the tip edge. Figure 5.2 shows that the cross-sectional area of the TV suddenly expands at $\alpha = 40°$ after gradually increasing from $\alpha = 10°$ to $\alpha = 30°$, suggesting the TV breakdown takes place by $\alpha = 40°$ (Leibovich, 1978). A further analysis of the TV breakdown will be presented in a later section

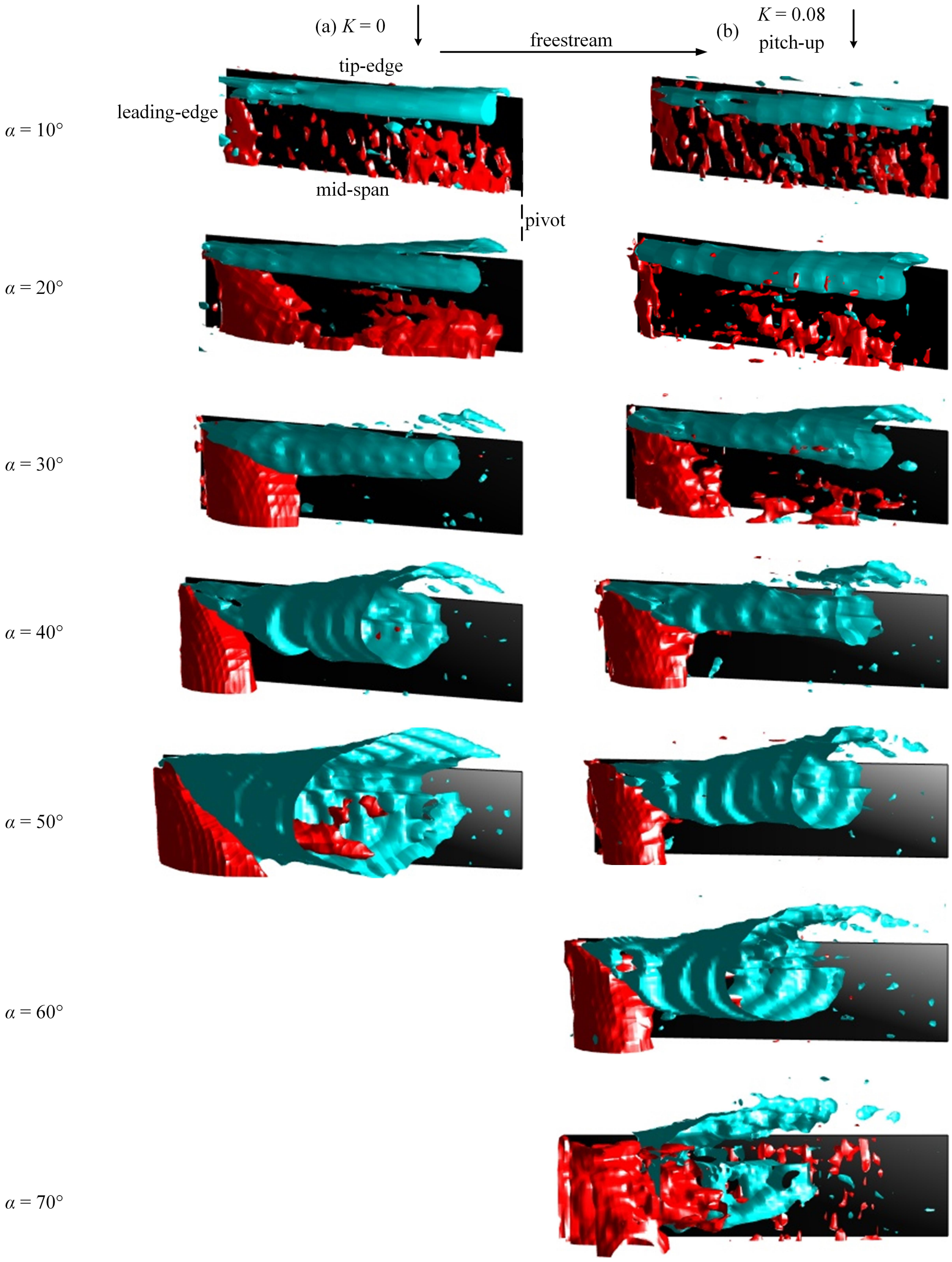

Figure 5.2: Side view of the vortical structures as a function of AoA behind a very low AR static ($K = 0$) and pitch-up ($K = 0.08$) wing. Shown in red and cyan are the volumes of iso-λ_2, which indicate the LEV and the TV, respectively.

to support this observation. The TV grows further to occupy the whole half-span of the wing at $\alpha = 50°$. Meanwhile, the flow near the leading edge seems to be fully attached, with no evidence of flow separation at $\alpha = 10°$. At $\alpha = 20°$, the separated shear layer from the leading edge rolls up to generate discrete vortices, which are convected downstream along the wing chord. With a further increase in the AoA, the separated shear layer from the leading edge reattaches to the wing surface. When the flow over the wing is about to reach a global separation at $\alpha = 50°$, the LEV moves away from the wing surface to become an arch-type structure (Kunihiko and Colonius, 2009; Visbal and Garmann, 2019a). For the pitch-up case at $K = 0.08$, as shown in Fig. 5.2b, LEV and TV structures are similar to those of the baseline case, except that the vortical development including the TV breakdown is delayed by approximately 10°.

5.4 TV development under pitching motion

Figure 5.3 shows the phase-averaged, non-dimensional streamwise vorticity $\omega_x c/U_\infty$ of the TV over a very low AR wing at $K = 0.08$, which is compared with that of the baseline case ($K = 0$). The flow is from left to right and the wing model is shown by a black rectangle. Here, only the flow over the upper half of the wing is shown, from the leading edge to the pivot point at the mid-chord. For the baseline case ($K = 0$), as shown in the first column of Fig. 5.3, the TV with a conical-shaped, negative vorticity region develops from the separated shear layer at the wing tip (Spalart, 1998). Near the leading edge, an area of positive streamwise vorticity is also observed, resulting from the interaction between the TV and the LEV (Dong et al., 2020). Similar results were also shown by Yilmaz and Rockwell (2012). The TV gradually increases its diameter downstream,

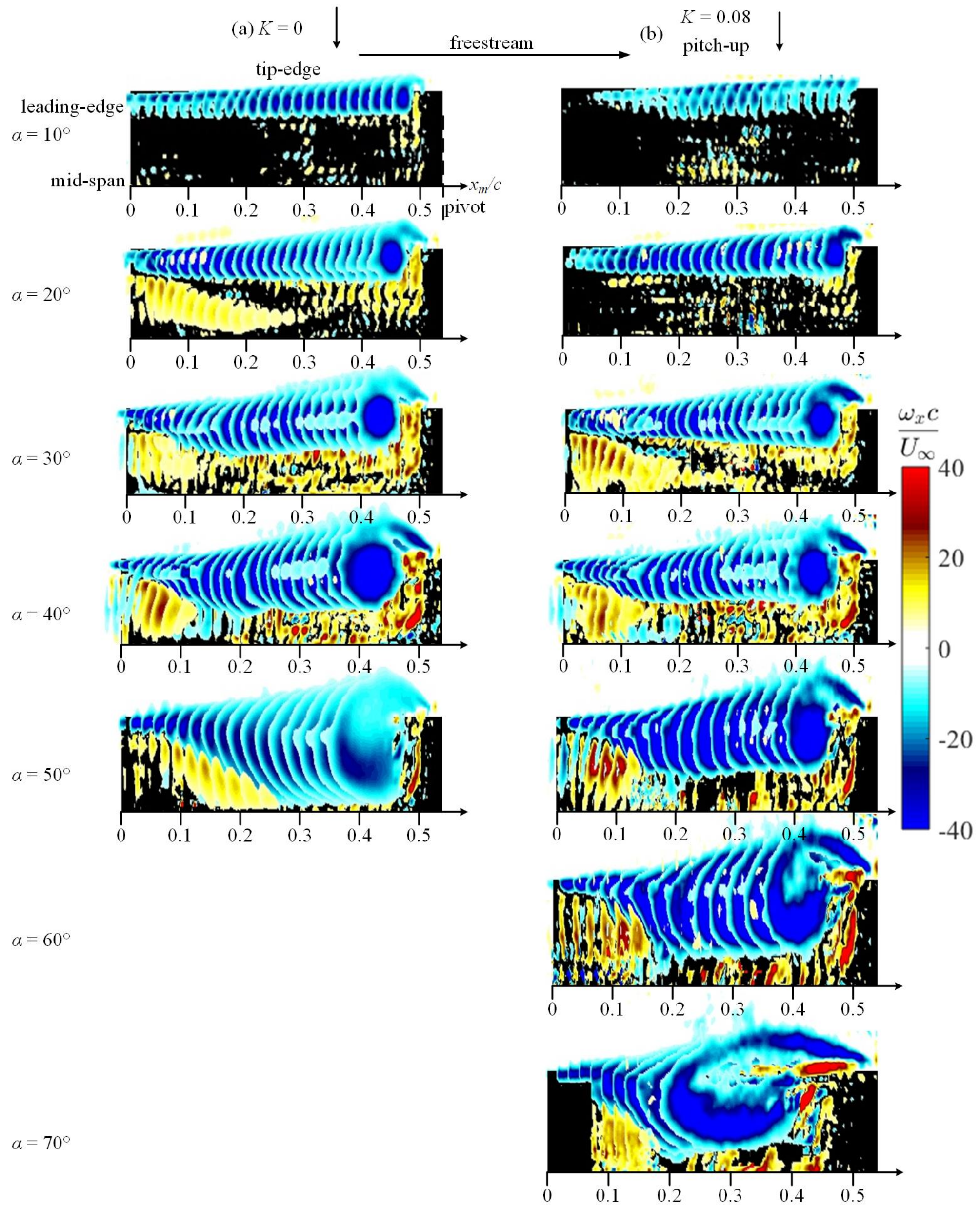

Figure 5.3: The phase-averaged normalised streamwise vorticity ($\omega_x c/U_\infty$) along the chord versus AoA for the wing pitching at $K = 0$ and 0.08. The colour bar on the right side applies to all plots.

whose sudden expansion is observed at $x_m/c = 0.15$ at $\alpha = 40°$. As the AoA is increased to $\alpha = 50°$, the diameter of the TV increases to nearly half the wing span and the vorticity distribution starts to become non-uniform. Between $\alpha = 30°$ and $50°$, the vorticity at the periphery of the TV shows wavy edges typical of the vortex instability, suggesting the occurrence of the vortex breakdown (Lee et al., 2002). The TV behaviour of the pitch-up wing with $K = 0.08$ is similar to that of the baseline case, except that its development seems to be delayed by nearly $10°$.

A comparison of the TV vorticity distribution between the pitch-up and pitch-down cases at $K = 0.03$ is shown in Fig. 5.4. The TV development on the pitch-up wing is similar to that of the baseline wing, as described in Fig. 5.3a, but with a small delay. Figure 5.4b shows that the pitch-down case with $K = 0.03$ starts at $\alpha = 90°$ with a global flow separation, which remains separated until the AoA is reduced to $\alpha = 40°$. A TV finally appears at $\alpha = 30°$. As a result, the vorticity over a pitch-down wing is much lower than that of the pitch-up wing. These results suggest that the influence of the pitch motion is to maintain the initial state of the flow structure over the wing, which is in good agreement with the stall hysteresis phenomenon (Leishman, 2006). In other words, the pitch-up wing starts with a fully attached flow, which is maintained to a higher AoA by delaying the development of the vortex structures. The pitch-down wing, on the other hand, starts with a fully separated flow, maintaining the global flow separation until a small AoA.

Detailed behaviour of the TV development at $K = 0.08$ is shown in Fig. 5.5 by the non-dimensional, phase-averaged streamwise vorticity $\omega_x c/U_\infty$ in the y-z plane at the pivot position ($x_m/c = 0.52$), which is superposed by velocity vectors. Here, the TV core and the vortex centroid are identified by the λ_2 method as described in Chap. 3.5, and are indicated by a circle

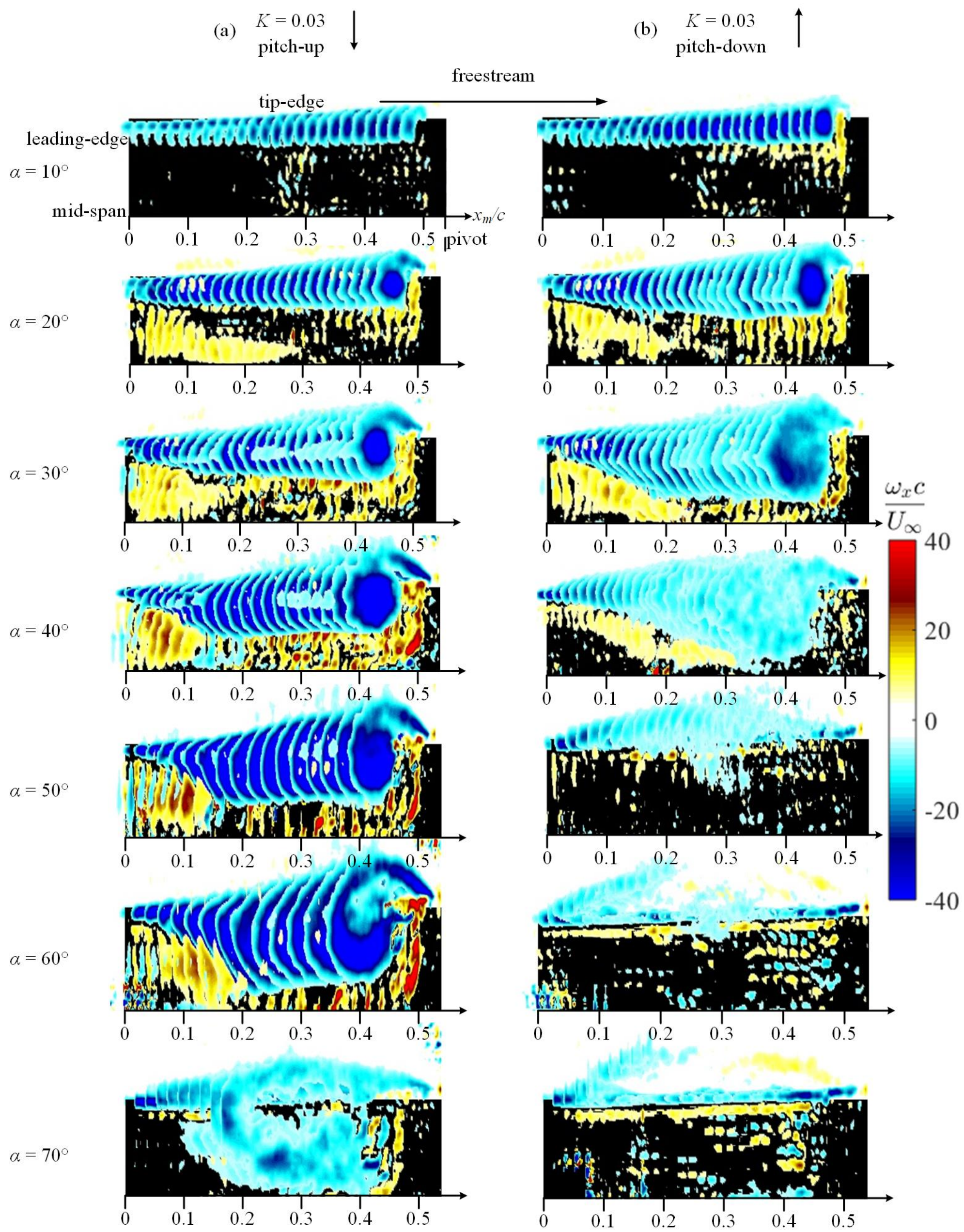

Figure 5.4: The phase-averaged normalised streamwise vorticity ($\omega_x c/U_\infty$) along the chord versus AoA for the wing pitching up and down at $K = 0.03$. The colour bar on the right side applies to all plots.

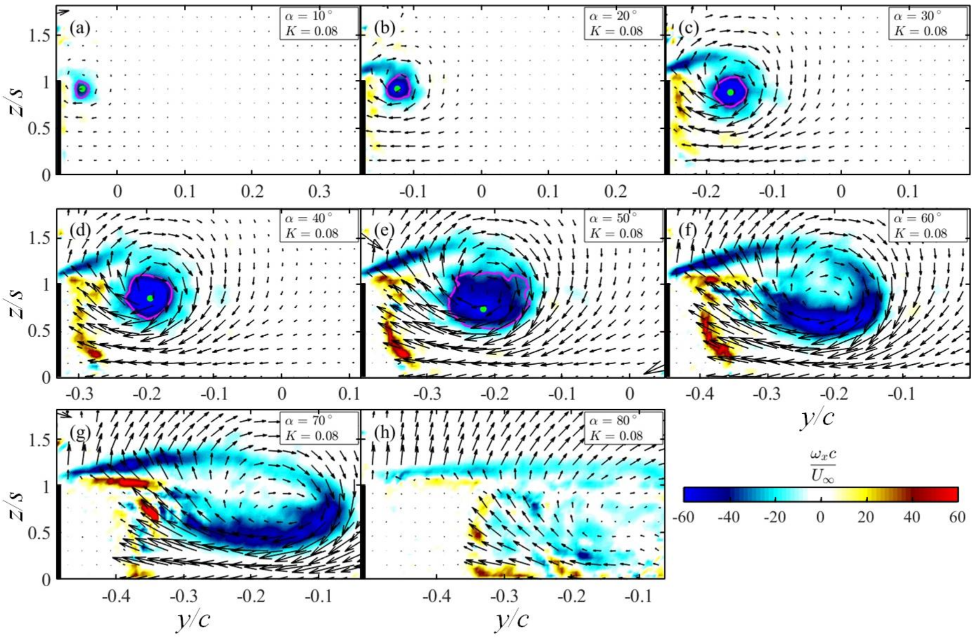

Figure 5.5: Progressive development of the normalised phase-averaged streamwise vorticity $\omega_x c/U_\infty$ superimposed on the velocity vectors in a y-z plane at the pivot ($x_m/c = 0.52$) of the wing from $\alpha = 10°$ to $\alpha = 80°$ pitching at $K = 0.08$. The core and centroid of the TV are indicated by a pink circle and green point, respectively, in each figure.

and a dot, respectively. A thick vertical line on the left of each figure indicates the position of the wing. Here, the velocity vectors and vorticity are missing close to the wing surface for $\alpha > 40°$, see Fig. 5.5. This is due to the PIV laser light reflection on the wing surface, where the affected area is increased with an increase in the AoA. However, this does not influence the circulation measurements and vortex core tracking since the TV moves away from the wing surface at the same time. Up to $\alpha = 40°$, the circular TV core moves away from the wing surface while staying at the same spanwise position. As the AoA increases further, the TV core is wrapped around by a ribbon-like shear layer from the wing tip (see also Fig. 5.9). The diameter of the TV increases dramatically at this point, suggesting that the TV is going through vortex breakdown. At this time, the vortex centroid starts to move away from the wing tip towards the mid-span. With a further increase in the AoA, the vortex core and the associated vorticity

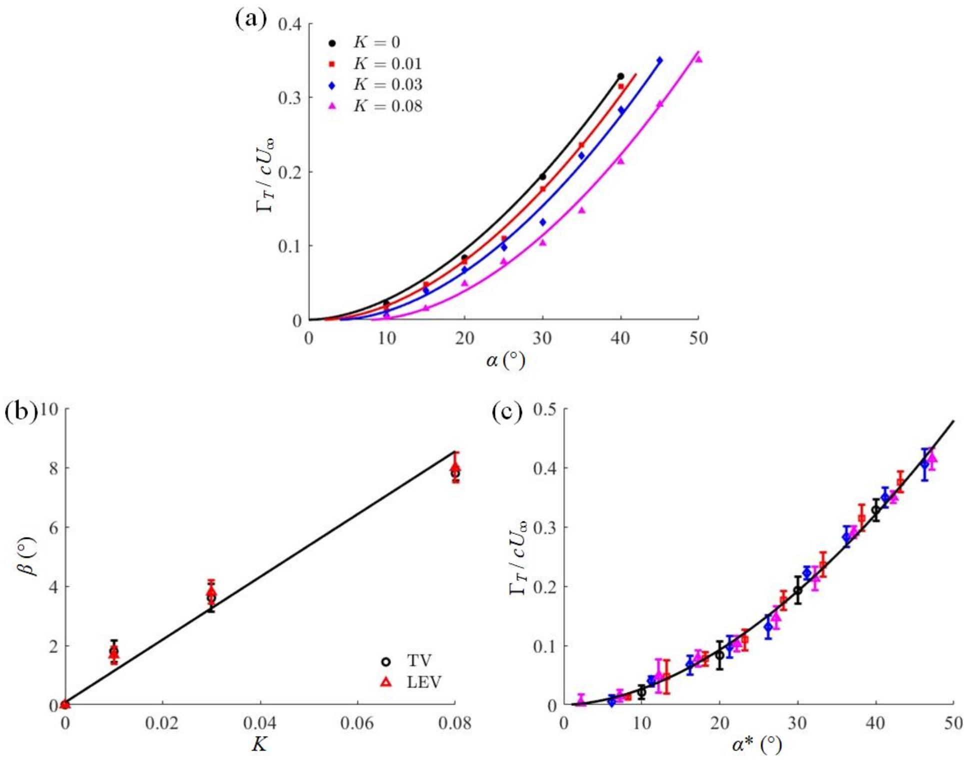

Figure 5.6: (a) Development of normalised circulation (Γ_T/cU_∞) of the TV at the pivot ($x_m/c = 0.52$) as a function of α, (b) phase lag of the TV and the LEV as a function of the pitch rate K and (c) TV circulation (Γ_T/cU_∞) versus α^*.

distribution become highly distorted, making it is difficult to identify the TV core anymore. The vorticity of the TV has almost vanished at $\alpha = 80°$, indicating that the global flow separation takes place at this AoA.

To better understand the effect of the pitch-up motion on the flow structures over a very low AR wing, we now investigate the circulation of the TV core at $x_m/c = 0.52$, excluding the secondary vorticity near the wing surface. Here, the streamwise location ($x_m/c = 0.52$) is where the laser sheet in the y-z plane crosses on the wing chord line. Figure 5.6a shows the non-dimensional circulation of the TV against the AoA α, indicating that the development of the TV circulation is delayed by the pitch-up motion. This delay is called the phase lag, which is defined as the difference in the pitch-up angle between the baseline wing and the pitching wing in

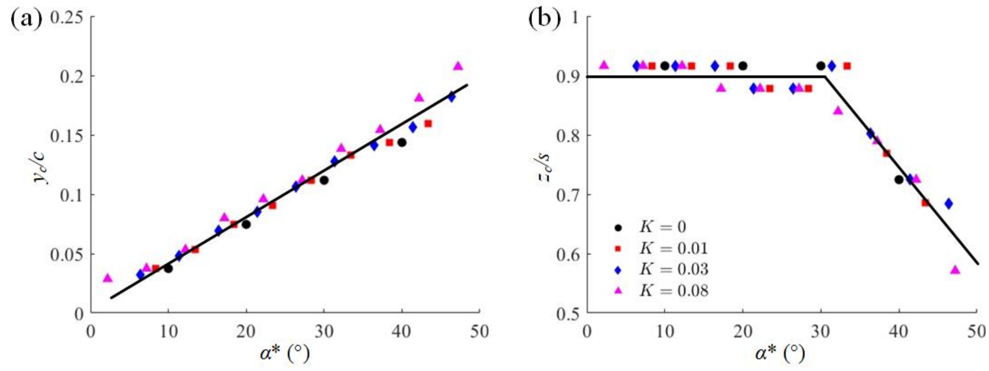

Figure 5.7: The locus of the TV centroid throughout the pitching motion at the pivot ($x_m/c = 0.52$) as a function of α^*. (a) The distance to the wing surface; (b) the distance to the mid-span.

achieving the same circulation. These results show that the phase lag β is a linear function of the non-dimensional pitch rate K, see Fig. 5.6b, which is given by $\beta = 1.85K$ when β is expressed in radians. Here, the error bars in the figure indicate the uncertainties in β based on all circulation measurements up to $\alpha = 50°$. Although the phase lag β is obtained at $x_m/c = 0.52$, it should not be affected by the streamwise position of the TV circulation measurements. This can be seen in Fig. 5.8a, which shows that the TV circulation increases linearly with the streamwise distance until close to $x_m/c = 0.52$. The phase lag of the LEV, which is defined in a similar way for the TV circulation, is also shown in Fig. 5.6b. It is interesting to observe that the phase lag of the LEV is nearly identical to that of the TV, suggesting that the dynamics of the LEV is strongly influenced by the TV. After removing the effect of the phase lag, the AoA is given by a new parameter $\alpha^* = \alpha - \beta$. Figure 5.6c demonstrates that the TV circulation data for all K values can be collapsed onto a single curve when they are plotted against α^*. This gives the non-dimensional circulation as $\Gamma_T/cU_\infty = 0.628(\alpha^*)^{1.8}$ when α^* is expressed in radians.

Similarly, the trajectory of the TV centroid during the pitch-up motion also overlaps using α^*, as shown in Figs. 5.7a and b, where the position of

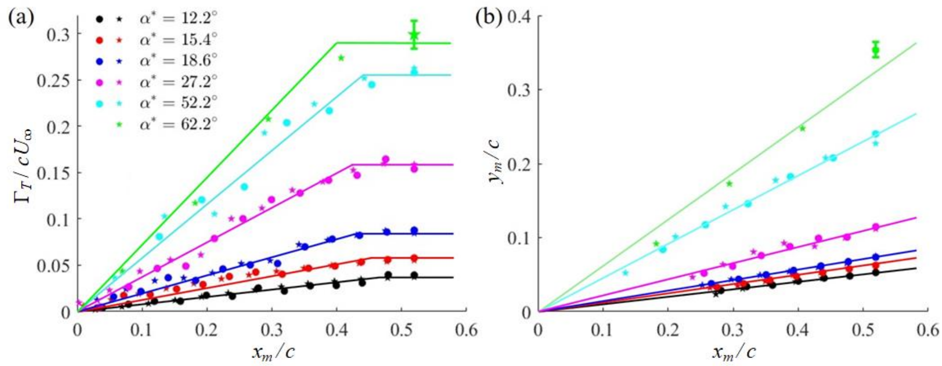

Figure 5.8: Development of (a) the TV circulation and (b) the distance between the vortex centroid and the wing surface along the wing chord at $K = 0.01$ (circles) and 0.08 (stars).

the TV centroid is given by y_c/c and z_c/s, respectively. The TV stays near $z_c/s = 0.9$ for $\alpha^* < 30°$ and moves towards the wing mid-span after the vortex breakdown with an increase in α^*. However, y_c/c always increases linearly with an increase in the AoA. The circulation and the core location of the TV are obtained based on the PIV data, which are shown in Fig. 5.8 for different α^*. Here, only the results at $K = 0.01$ and 0.08 are depicted for clarity. This shows that the circulation initially increases linearly downstream to reach a plateau just before the pivot position ($x_m/c = 0.52$), while the distance between the TV and the wing wall exhibits a monotonic increase along the wing chord. These results are consistent with DeVoria and Mohseni (2017b) and Dong et al. (2020).

Figures 5.9a and b show the instantaneous vorticity field during the TV breakdown in the y-z plane at the pivot ($x_m/c = 0.52$), demonstrating that the development of the vortex structures for $K = 0.01$ and $K = 0.08$ is similar against α^*. At $\alpha^* = 25°$, a circular-shaped TV core is observed near the wing tip. Increasing the AoA to $\alpha^* = 32°$, the vortex core begins to expand rapidly and loses its coherence, indicating the start of vortex breakdown. The process of vortex breakdown continues through to $\alpha^* = 40°$. At $\alpha^* = 50°$, the vortex core disappears, where the vorticity from the

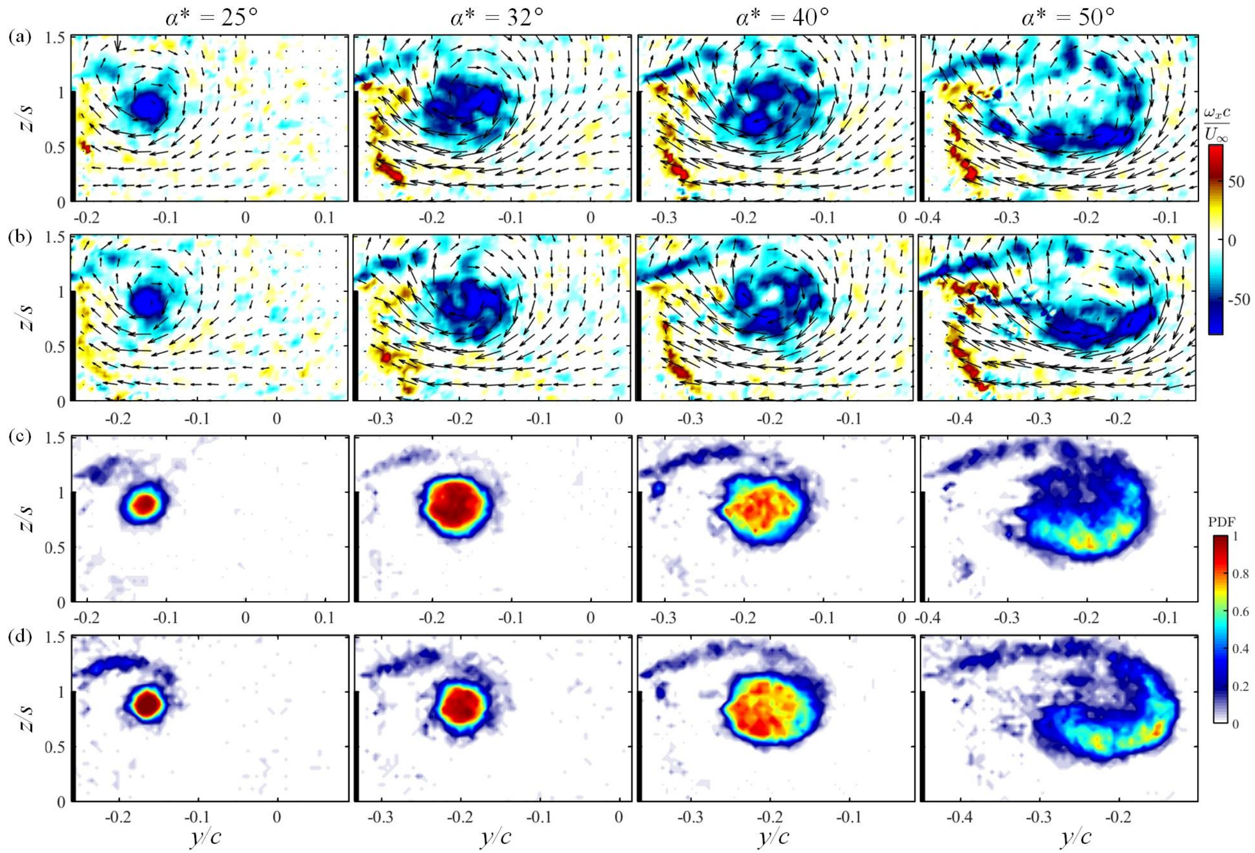

Figure 5.9: Distribution of instantaneous flow fields in the y-z plane at the pivot ($x_m/c = 0.52$). The vorticity fields at $K = 0.01$ (a), the vorticity fields at $K = 0.08$ (b), PDF of the TV vortices identified by the λ_2-criterion at $K = 0.01$ (c) and at $K = 0.08$ (d).

separated shear layer is dispersed to the bottom of the TV near the wing mid-span. The loss of vortex coherence associated with the TV breakdown is analysed using the probability density function (PDF) of the TV vortices identified by the λ_2-criterion. Figures 5.9c and d show the probability distribution of the identified vortices based on the instantaneous vorticity field in the y-z plane at each AoA, as shown in Figs. 5.9a and b. For $\alpha^* < 32°$, the probability of the identified vortices is axisymmetrically distributed around the centre of the TV, where the probability is close to 100%. At $\alpha^* = 40°$, however, the axisymmetry of the probability distribution is lost with a simultaneous reduction in the probability around the centre of the TV, which is caused by the vortex breakdown. A further reduction in the probability of identified vortices is observed at $\alpha^* = 50°$, where a circular TV cross-section is completely lost. Since a sudden expansion of the TV cross-sectional area is one of the criteria for the vortex breakdown (Leibovich, 1978), a jump in the TV core area (S_{TV}) at $\alpha^* = 32°$, as shown in Fig. 5.10a, strongly suggests that TV breakdown is taking place at this AoA. Although a global separation can also lead to a large increase in the TV diameter, it should not be taking place at $\alpha^* = 32°$ since the maximum lift angle of a very low AR flat-plate wing is $\alpha^* = 40°$ as shown in Fig. 5.1. The AoA for the initiation of the vortex breakdown at different chordwise locations x_m/c is also investigated and shown in Fig. 5.10b. This shows that the location of the vortex breakdown is shifted upstream nearly linearly with an increase in α^*.

The V-component velocity over the suction side of the wing at the pivot ($x_m/c = 0.52$) is obtained from the PIV measurements, showing the spanwise variation of the velocity from the TV centroid to the wing mid-span, see Fig. 5.11a. Again, the velocity profiles of the pitch-up wing with $K = 0.08$ are similar to those of the baseline case when the phase-lag ad-

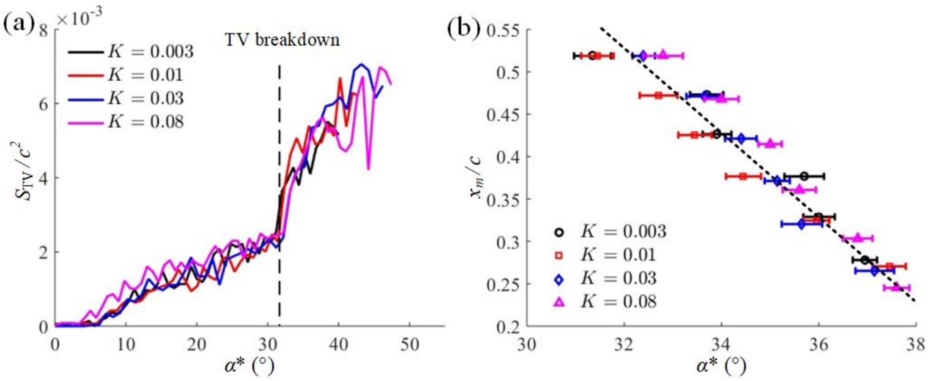

Figure 5.10: (a) The change of the TV core area S_{TV} as a function of α^* at different pitch rates at the pivot ($x_m/c = 0.52$), (b) the TV breakdown along the chord of the wing versus α^* at different pitch rates.

justed AoA α^* is used even after the vortex breakdown ($\alpha^* = 40°$). The peak velocity in Fig. 5.11a is shown in Fig. 5.11b as a function of α^*, where the start of the TV breakdown can be identified by the discontinuity in the velocity profile. Although the negative peak velocity increases nearly linearly with the AoA, its rate of increase reduces to nearly 1/4 after the TV breakdown. The variation of the non-dimensional circulation Γ_r/Γ_T of the TV is shown in Fig. 5.11c as a function of the non-dimensional radius r/r_c. Here, Γ_T is the circulation of the TV core, see Fig. 5.6c, and r_c is the TV core radius which is estimated by $\sqrt{S_{\mathrm{TV}}/\pi}$. Our results agree well with those by Hoffmann and Joubert (1963), Phillips (1981), Birch and Lee (2005) and Skinner et al. (2020), whose suggested the following correlations:

$$\begin{aligned} \Gamma_r/\Gamma_T &= A_1(r/r_c)^2 && \text{for} \quad r/r_c < 0.4, \\ \Gamma_r/\Gamma_T &= A_2\log(r/r_c) + A_3 && \text{for} \quad 0.5 < r/r_c < 1.4. \end{aligned} \tag{5.1}$$

where $A_1 = 1.83$, $A_2 = 2.14$ and $A_3 = 1$ are best-fit constants to our data. The self-similar distribution of Γ_r/Γ_T from $\alpha^* = 20°$ to $\alpha^* = 40°$ is observed for all pitch-up cases studied here. Ours results in the core region can also be expressed by a sixth-order polynomial (Birch and Lee, 2005;

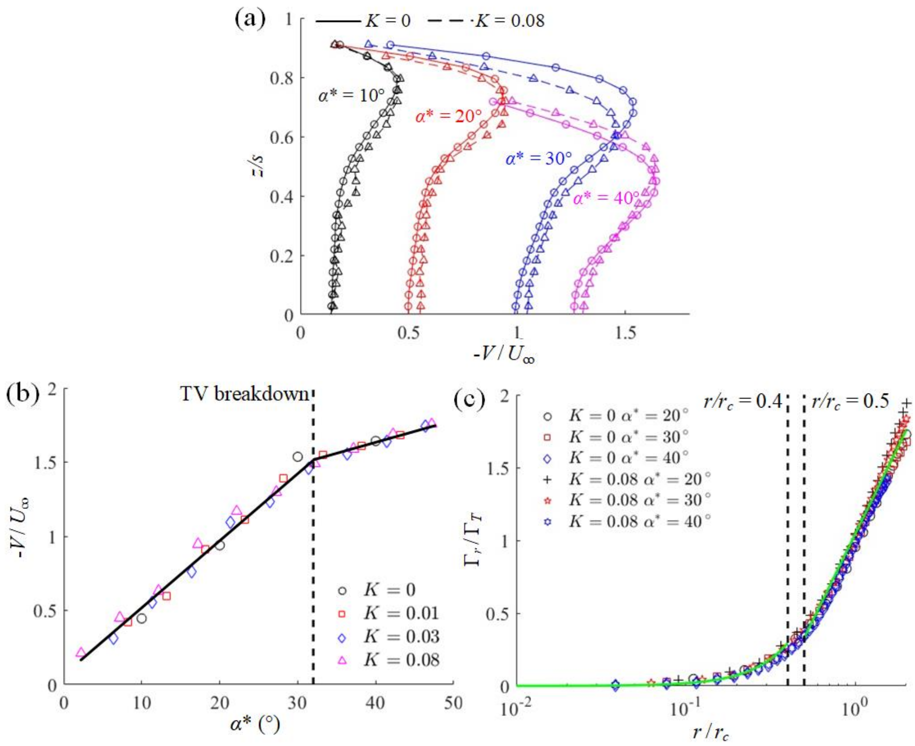

Figure 5.11: (a) The V-component velocity profiles over the suction side of the wing from the TV centroid to the mid-span at the pivot at $K = 0$ and $K = 0.08$, (b) the peak velocity of V between the TV centroid and the mid-span as a function of α^* at different pitch rates, (c) non-dimensional circulation versus its radius at different AoAs at the pivot.

Skinner et al., 2020):

$$\Gamma_r/\Gamma_T = 1.756(r/r_c)^2 - 1.044(r/r_c)^4 + 0.263(r/r_c)^6 \quad \text{for} \quad 0 < r/r_c < 1. \tag{5.2}$$

Figure 5.12 shows a comparison in the development of the axial velocity of the TV at the pivot ($x_m/c = 0.52$) between the pitch-up case ($K = 0.08$) and the baseline case ($K = 0$). The locus of the TV centroid and the TV edges are shown in dash and solid lines, respectively, as a function of α^*. It should be mentioned here that the axial velocity in Fig. 5.12 is not always located at the same spanwise position since the vortex centroid can move towards the mid-span after the TV breakdown, as shown in Fig. 5.7b.

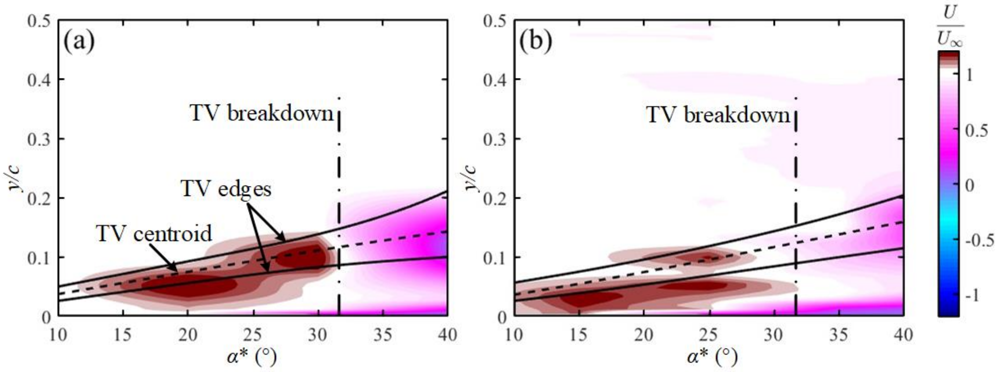

Figure 5.12: Non-dimensional axial velocity (U/U_∞) through the TV centroid as a function of α^*: (a) baseline case and (b) pitching at $K = 0.08$.

At $\alpha^* < 32°$, the axial velocity of the TV is greater than the freestream velocity, forming a jet-like vortex core, which is observed by Shah et al. (1999), Batchelor (1964), Saffman (1995) and Birch and Lee (2005) on delta wings as well as on large AR wings. This may be due to the accelerated flow inside the TV core owing to the negative pressure gradient (Bailey et al., 2006). Another axial velocity excess can be observed between the wing surface and the TV edge. With an increase in the AoA beyond the vortex breakdown angle of $\alpha^* = 32°$, the TV core changes from a jet like to a wake like, increasing the amount of velocity deficit.

5.5 LEV development under pitching motion

The distribution of non-dimensional, phase-averaged spanwise vorticity ($\omega_z c/U_\infty$) over the pitching wing at $K = 0.08$ is shown in Fig. 5.13b for AoAs from 10° to 70°, which is compared with that of the baseline case as shown in Fig. 5.13a. Here, the vorticity contours are obtained from PIV measurements in 8 x-y planes, see Fig. 3.3. For the baseline case ($K = 0$), the shear layer near the leading edge starts to roll up at $\alpha = 20°$, and its reattachment point at the mid-span is near the pivot ($x_m/c = 0.52$). At $\alpha = 30°$, the reattachment point moves upstream, increasing the negative vorticity within the LEV. Here, secondary vorticity regions can also be observed beneath the LEV. With an increase in the AoA the flow reattachment point moves further upstream until $\alpha = 50°$, when the LEV starts to expand, reverting the reattachment point downstream. At the same time, the separated shear layer moves away from the wing surface, creating an arc-shaped vorticity region. The roll-up of the LEV continues until it reaches a global flow separation at $\alpha = 60°$. For the pitching case, see Fig. 5.13b, the LEV goes through much the same developmental process as the baseline case. However, the pitching motion delays the LEV development in a similar way as it does to the TV development, see Fig. 5.3b.

A comparison of the pitch-up and pitch-down cases is shown in Fig. 5.14 for $K = 0.03$. For the pitch-down case, the flow starts with a globally separated state and the separated shear layer does not reattach until at $\alpha = 30°$. Here, the reattachment point is observed much further downstream as compared to the pitch-up case at the same AoA. It is difficult to identify the LEV at $\alpha > 30°$ due to the effect of the pitching motion, which maintains the initial flow state. We will only focus on the pitch-up cases in the following discussions of the LEV.

Figure 5.15 shows the development of the non-dimensional spanwise vorticity with the measured velocity vectors at the mid-span of the wing as a function of α^* under the pitch-up motion at $K = 0.08$. At $\alpha^* = 12.2°$, the shear-layer vorticity and the velocity vectors are parallel to the wing surface almost everywhere, indicating a fully attached flow. At a later stage, a small laminar separation bubble is formed at the leading edge at $\alpha^* = 15.4°$, and the rolled-up vortices start to shed at $\alpha^* = 18.6°$. At $\alpha^* = 27.2°$, the separated shear layer reattaches to the wing, forming a large separation

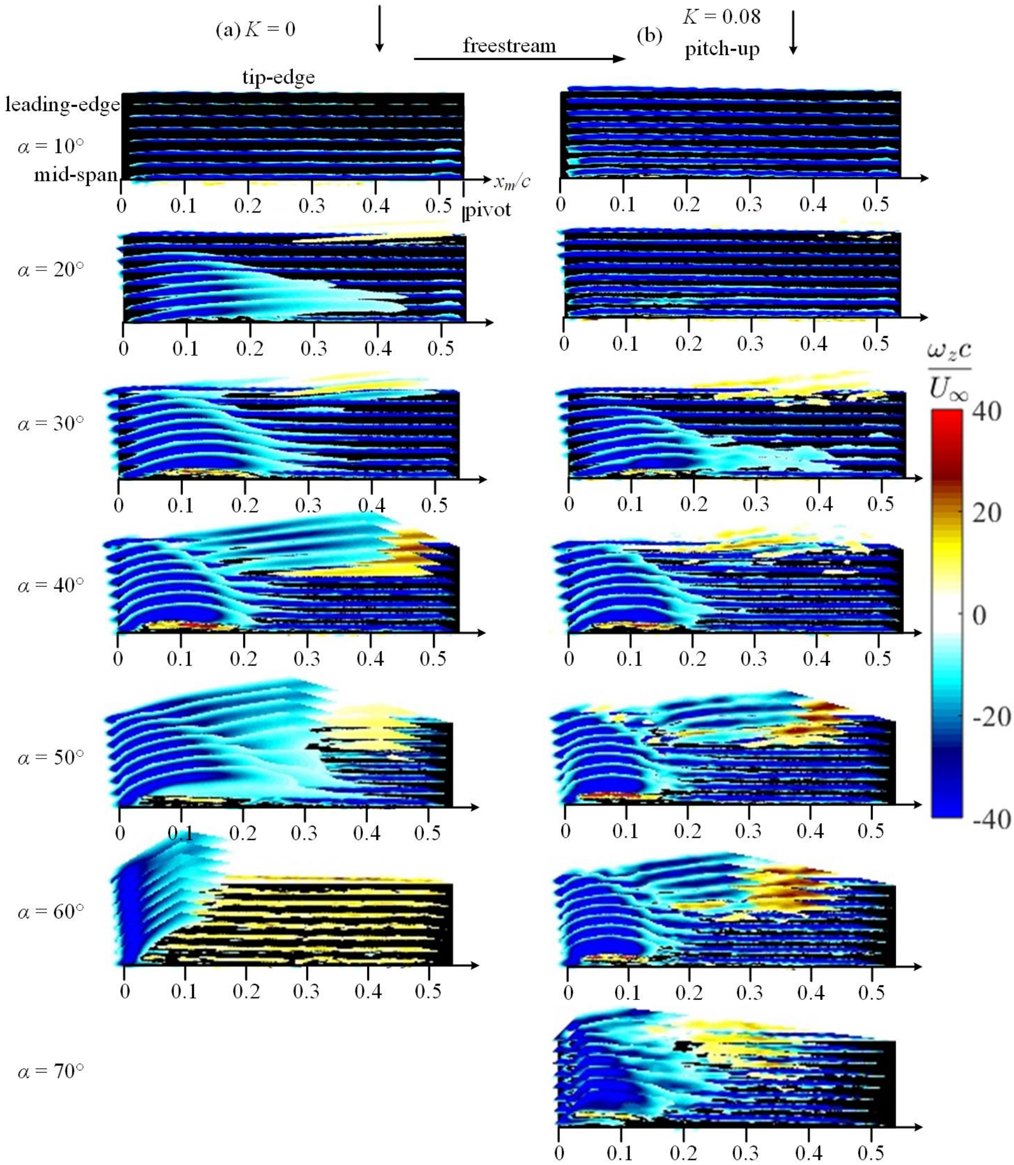

Figure 5.13: The phase-averaged normalised spanwise vorticity ($\omega_z c/U_\infty$) along the span versus AoA for the baseline case and the wing pitching at $K = 0.08$. The colour bar on the right side applies to all plots.

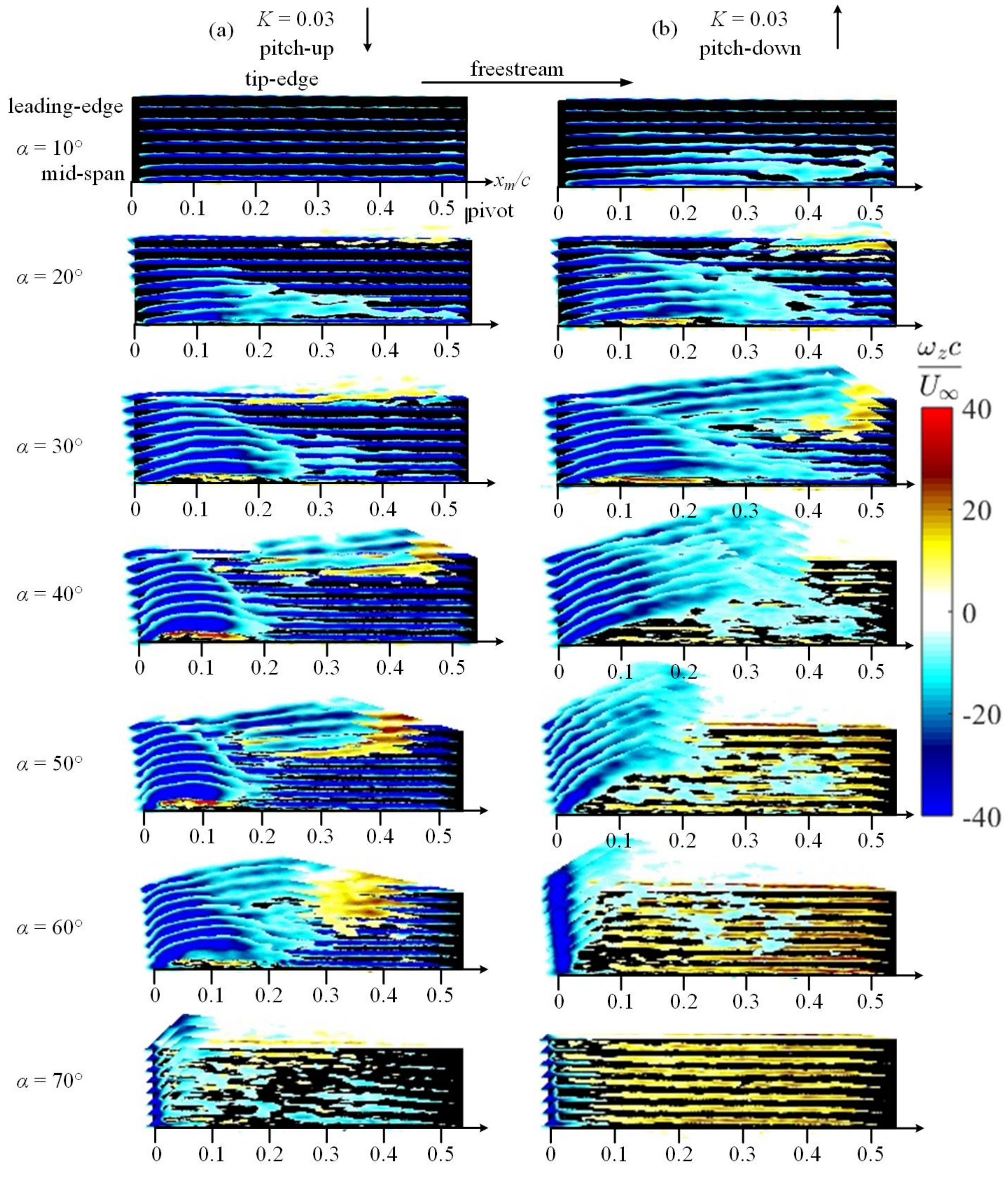

Figure 5.14: The phase-averaged normalised spanwise vorticity ($\omega_z c/U_\infty$) along the span versus AoA for the pitch-up and pitch-down wing at $K = 0.03$. The colour bar on the right side applies to all plots.

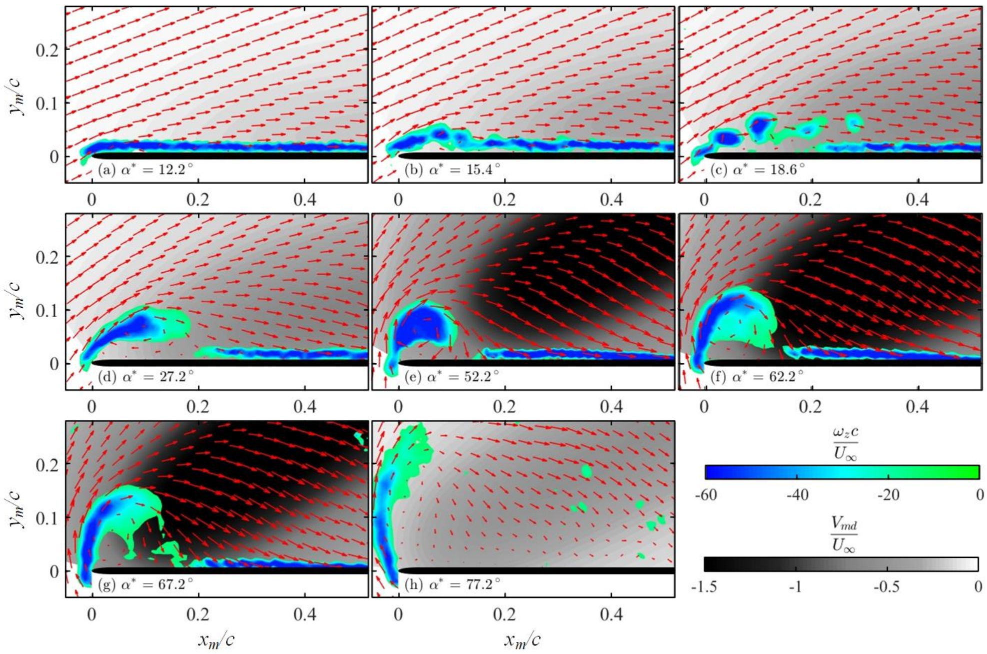

Figure 5.15: Progressive development of the normalised spanwise vorticity $\omega_z c/U_\infty$ superimposed on the velocity vectors and estimated downwash V_{md} at the mid-span of the very low AR wing pitching at $K = 0.08$ as a function of α^*.

bubble. A small positive secondary vorticity region is also seen beneath the LEV, which is due to recirculating flow within the separation bubble. Here, the wallward velocity vectors near the trailing edge of the laminar separation bubble seem to be interacting with the separation bubble to help reattach it to the wing surface. With a further increase in the AoA to $\alpha^* = 52.2°$, the LEV increases its strength while the reattachment points shift upstream, as shown in Fig. 5.15e. Here again, we can observe a strong wallward velocity immediately downstream of the LEV. The shear layer is then lifted up at $\alpha^* = 62.2°$ and finally the flow completely separates from the wing surface at $\alpha^* = 77.2°$, see Fig. 5.15h. The results shown in Fig. 5.15 suggest that the flow over the very low AR wing goes through four distinct stages under the pitching motion. They are: attachment, vortex shedding, reattachment and separation, all of which seem to be affected by the wall-normal velocity. To investigate if the strong wallward velocity as shown in Fig. 5.15 is due to the downwash of the TV, we estimate the

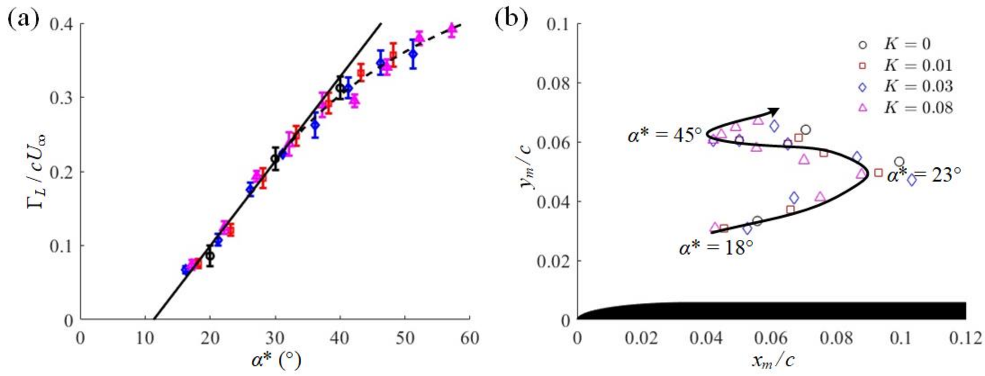

Figure 5.16: (a) The normalised circulation of the LEV versus α^* at the mid-span with different K, (b) the locus of the LEV centroid throughout the pitching motion.

induced velocity using the Biot-Savart law based on the inviscid flow assumption. Here, the TV is modelled by a straight semi-infinite line vortex originating from the tip of the leading edge ($x_m/c = 0$, $z_m/s = 1$). The measured location and the circulation of the TV used for this calculation are given in Fig. 5.8. Where the TV circulation is increasing (see Fig. 5.8a), the line vortex is divided into several vortex elements with a constant circulation before applying the Biot-Savart law. It should be noted that the assumption of a line vortex is no longer valid after the TV breakdown. Therefore, the results should be treated with caution. Nevertheless, the result demonstrates that the estimated downwash (shown in the grey scale map) in Fig. 5.15 corresponds to the measured velocity field very well, confirming that the TV has a strong influence on the LEV behaviour, as discussed above.

The development of the non-dimensional circulation (Γ_L/cU_∞) of the LEV at the mid-span during the pitch-up motion is shown in Fig. 5.16a as a function of α^*, showing that the LEV is not formed at the early stage of pitching. With an increase in the AoA, the circulation of the LEV increases linearly until it reaches to $\alpha^* = 32°$, which can be expressed by $\Gamma_L/cU_\infty = 0.653\alpha^* - 0.129$ when α^* is expressed in radians. However, the

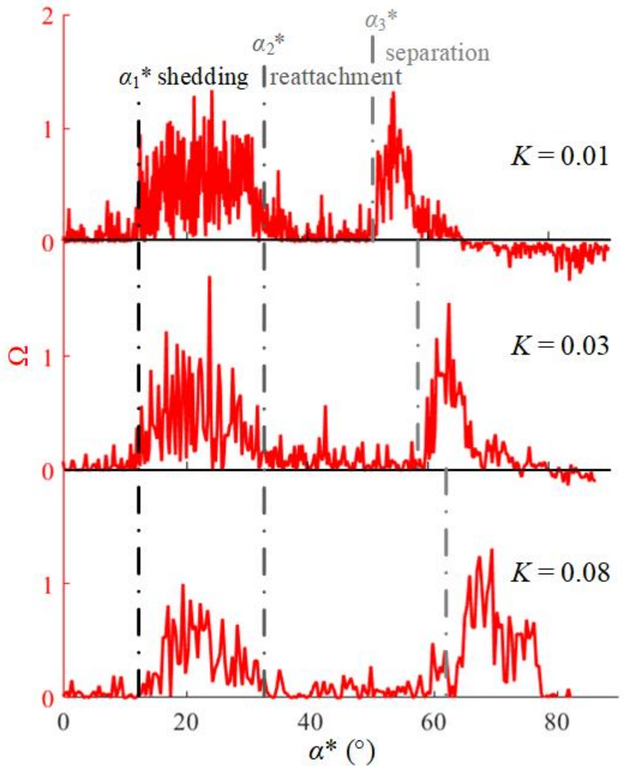

Figure 5.17: Non-dimensional vorticity flux Ω at the mid-span versus α^* when the wing is pitching at $K = 0.01, 0.03$ and 0.08.

growth rate of the circulation of the LEV reduces with a further increase in the AoA due to the TV breakdown. Figure 5.16b shows the locus of the LEV centroid during the pitch-up motion at different pitch rates. The LEV is formed at $\alpha^* = 18°$, and gradually moves away from the wing surface with an increase in the AoA. The chordwise movement of the LEV centroid is rather complicated, however. Initially, the LEV moves downstream until $\alpha^* = 23°$ and then moves back upstream. At $\alpha^* = 45°$, the LEV centroid starts to move downstream again due to the lift-off of the separated shear layer at the leading edge. Overall, the LEV over a very low AR pitching wing stays very close to the leading edge of the wing ($x_m/c = 0 \sim 0.1$ and $y_m/c = 0 \sim 0.08$) until flow starts to separate.

To further examine the behaviour of the separating shear layer and the associated spanwise vorticity development of the LEV, the non-dimensional

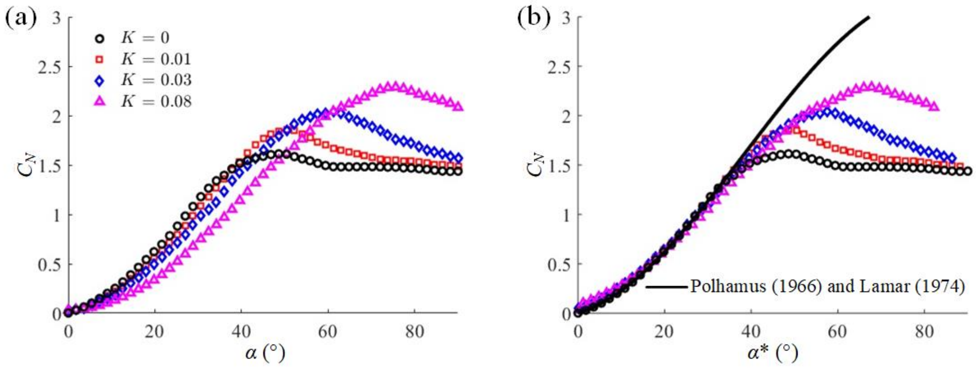

Figure 5.18: The normal force coefficient C_N over a very low AR wing: (a) versus α and (b) versus α^*.

vorticity flux $\Omega = -\int \omega_z U_m \mathrm{d}y_m / U_\infty^2$ at the mid-span of the wing at $x_m = 0.17c$ is shown in Fig. 5.17. This x_m position corresponds to the most downstream location of the LEV before flow separation takes place over the wing, see Fig. 5.15. The vorticity flux is obtained along the path normal to the wing from $y_m = 0.015c$ to $y_m = 0.15c$, excluding the secondary vorticity within the separation bubble. There is a significant rise in the vorticity flux at $\alpha_1^* = 12.6°$, which is due to the vortex shedding from the laminar separation bubble, see Fig. 5.15c. The vortex shedding stage lasts until $\alpha_2^* = 33°$, which is followed by the reattachment stage. Here, the vortex flux remains nearly zero until the start of the flow separation at α_3^*. The separation stage continues until the end of the pitching motion, see Fig. 5.15h. The angles α_1^* and α_2^* are independent of the pitch rate K, as shown in Fig. 5.17. However, the initiation angle for flow separation α_3^* increases with an increase in the K value, indicating a monotonic increase in the stall angle with K.

5.6 Normal forces

The normal force coefficient C_N for a stationary ($K = 0$), very low AR thin plate is presented in Fig. 5.18a, showing that C_N increases slowly at small AoAs. With a further increase in the AoA, however, the normal force coefficient increases sharply to attain the maximum value of $C_N = 1.6$ at $\alpha = 48°$. The normal force coefficient reduces slightly after the maximum C_N until $\alpha = 90°$. With pitching motion on a wing, the maximum C_N and the maximum C_N angle are both increased. For example, the maximum C_N is increased by up to 44% with $K = 0.08$ while the maximum C_N angle is increased from 48° to 75°. Such behaviour of C_N is not surprising, however, since the normal force coefficient C_N is related to C_L and C_D through an equation given by $C_N = C_L \cos\alpha + C_D \sin\alpha$. In other words, C_N behaves like C_L for small α, while it behaves like C_D for large α, see Fig. 5.1a.

The shift of C_N curve to the right (towards the larger α) with increasing pitch rate K, as observed in Fig. 5.18a, is due to the phase lag in the development of TV and LEV over a pitching wing. By replotting Fig. 5.18a in terms of α^* after removing the effect of the phase lag due to the pitch motion, all experimental results lie on a single curve, as shown in Fig. 5.18b. The curve drawn in Fig. 5.18b is given by an equation $C_N = k_p \sin\alpha^* \cos\alpha^* + k_v \sin 2\alpha^*$, as suggested by Polhamus (1966) and Lamar (1974). Here, k_p and k_v were obtained through a curve fitting to our experimental data. This results in $k_v = \pi$ and a slightly larger value of $k_p = 0.77$ than suggested by Lamar (1974), which may be due to the elliptical leading edge.

Chapter 6

Plasma flow control of a very low AR wing

6.1 Introduction

Previously, we have studied the interaction between the TV and the LEV over a stationary and pitching very low AR wing, where the influence of the TV on the development of the LEV was demonstrated (Dong et al., 2020). Building on the understanding of the vortex interactions gained from these studies, a flow control study of a very low AR wing is carried out using DBD plasma actuators. By controlling the TVs using the plasma jet at the wing tip, we are able to influence the aerodynamic forces of the wing. The influence of the plasma actuators on the TVs is analysed by documenting the vortex locus as well as velocity and vorticity distributions around the vortex core to understand the mechanism of plasma control of a very low AR wing.

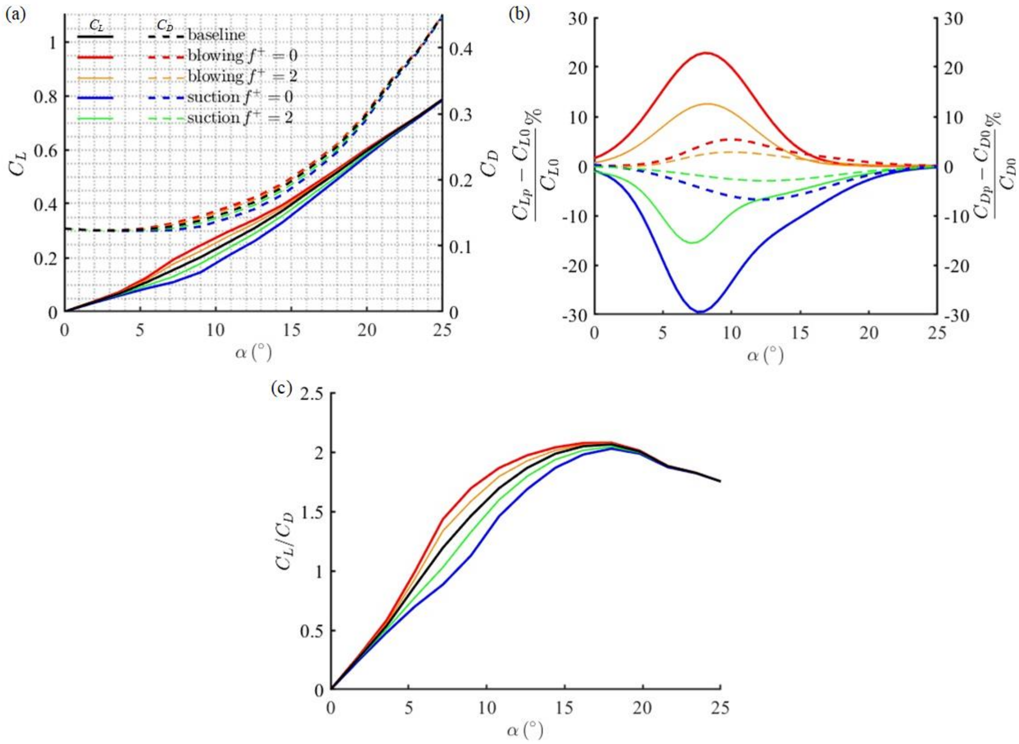

Figure 6.1: Effect of the plasma actuators on the aerodynamic forces on a flat-plate wing of the aspect ratio of 0.277 with an elliptic leading edge: (a) C_L and C_D, (b) the increment or decrement of C_L and C_D, (c) lift-to-drag ratio.

6.2 Aerodynamic forces on the very low AR wing with plasma control

The results for lift and drag coefficients with blowing and suction plasma actuators are compared with those of the baseline (plasma off) as shown in Fig. 6.1a. Here, it should be noted that the aerodynamic forces as well as the flow field around the two baselines, one for the blowing plasma and the other for the suction plasma, were identical within the experimental uncertainties. This clearly shows that the aerodynamic forces are modified by the plasma actuators, where C_L is significantly increased by the blowing plasma actuator, but is reduced by the suction plasma actuator between $\alpha = 4^\circ$ and $\alpha = 20^\circ$. Compared to the lift coefficient, the change of the drag coefficient is relatively small with the plasma actuator, which is less than 10% for all cases. The percentage changes in C_L and C_D due to the plasma actuators are shown in Fig. 6.1b, where the plasma data are indicated by C_{Lp} and C_{Dp}, while the baseline data are given by C_{L0} and C_{D0}, respectively. The most effective control is found at $f^+ = 0$ (steady mode) for both types of plasma actuators. Here, the maximum reduction in C_{L0} can reach 30% by the suction plasma, while the blowing plasma actuator produces an enhancement of C_{L0} by 23%. With a pulsed mode of plasma actuation, the control effect is reduced, where only 16% reduction and 13% enhancement in the lift coefficient are achieved by the suction and blowing plasma at $f^+ = 2$, respectively. This is due to the fact that the plasma momentum coefficient of the steady mode of actuation is about twice that of the pulsed mode of plasma actuation which is operating at 50% of the duty cycle. It is also observed that the most effective control of the plasma on the C_L occurs at around $\alpha = 8°$ for all cases. With a further increase in the AoA, the influence of the plasma actuators gradually vanishes. Figure 6.1c shows the lift-to-drag ratio of the very low AR wing, which takes the maximum value of $C_L/C_D = 2$ at $\alpha = 18°$. The changes in C_L/C_D as shown in Fig. 6.1c indicate that the aerodynamic efficiency of the wing can be manipulated by controlling the TV using the plasma actuator. To understand the underlying mechanism of the change in the aerodynamic forces due to plasma control, the behaviour of the TV with plasma at $\alpha = 10°$ and 15° will be demonstrated in the following section.

6.3 Plasma effect on the TV

The effect of the plasma actuators on the time-averaged, normalised streamwise vorticity ($\omega_x c/U_\infty$) is shown in Fig. 6.2, where ω_x is the streamwise vorticity, c is the chord length of the wing and $U_\infty$is the free-stream ve-

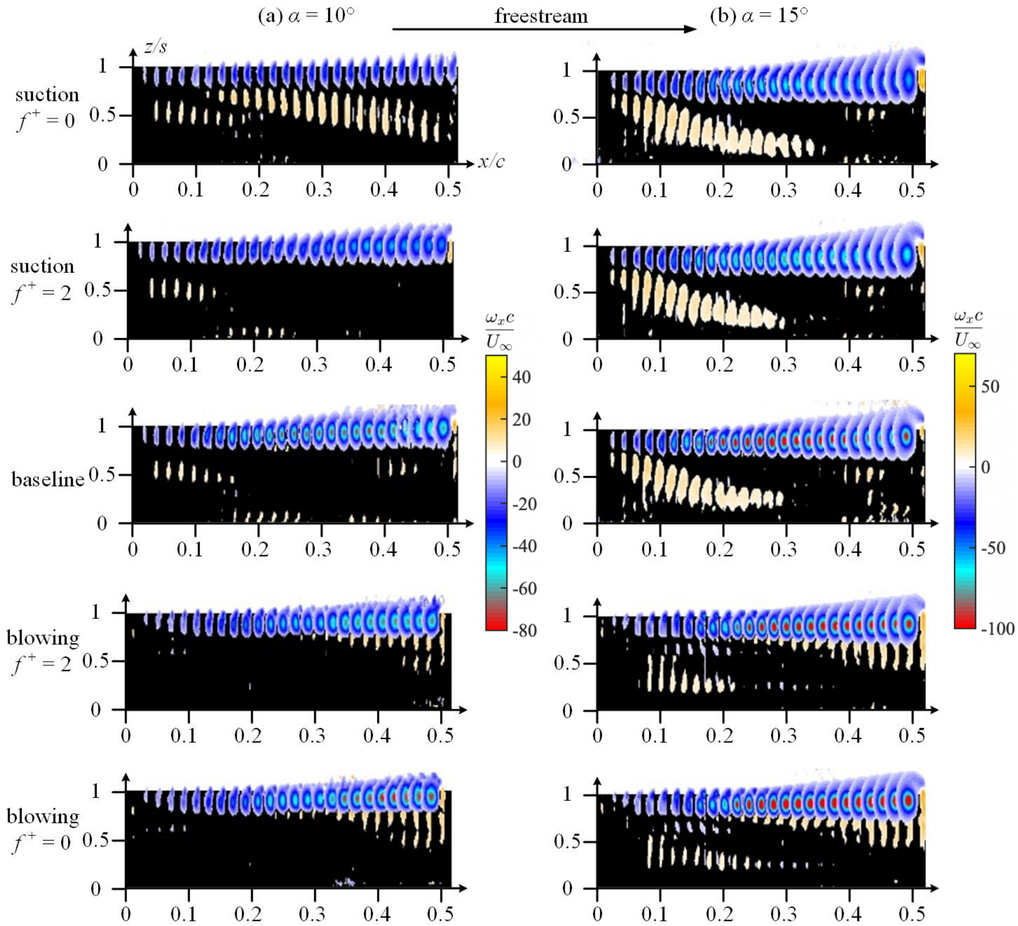

Figure 6.2: Side view of the time-averaged, normalised streamwise vorticity ($\omega_x c/U_\infty$) under the influence of the plasma actuators at $\alpha = 10°$ and $15°$ compared with that of the baseline case.

locity. This figure consists of the slices of separate PIV measurements in the y-z planes. Here, the separated flow at the wing tip wraps around from the pressure side to the suction side of the wing, forming a conical-shaped TV stretching along the wing chord. The size and strength of the TV increase downstream with an increase in the AoA. However, there is no sign of the TV breakdown in this figure at least for $0 < x/c < 0.52$ at $\alpha \leq 15°$. A weak, positive vorticity distribution near the leading edge ($x/c < 0.2$) is resulted from the interaction of the TV with the LEV, see Yilmaz and Rockwell (2012) at $Re = 1 \times 10^4$ and Dong et al. (2020) at $Re = 2 \times 10^5$. Applying the plasma actuators, the streamwise vorticity within the TV core becomes weaker with the suction control and stronger with the blowing control. The diameter of the TV remains unchanged by the plasma control, except for suction plasma control ($f^+ = 0$) at $\alpha = 10°$ where a reduction of the TV diameter is clearly seen.

To further examine the influence of the plasma actuators on the TV, the time-averaged vorticity field together with the turbulent intensity and the Reynolds stress distributions at the mid-chord are shown for $\alpha = 10°$ and $15°$ in Figs. 6.3 and 6.4, respectively. Here, the vortex cores, which are indicated by pink circles, are identified by the λ_2-criterion (Jeong and Hussain, 1995), where the corresponding centroids, shown in green dots, are found at the location of the minimum negative value of λ_2. Other vortex identification techniques, including Q-criterion (Chong et al., 1990) and Γ_1–criterion (Graftieaux et al., 2001), give similar results. The TV forms at the wing tip ($z/s = 1$) close to the wing surface, where a weak secondary vorticity is generated, see Fig. 6.3. The maximum turbulent intensity can be observed in the vortex core around the vortex centroid. The Reynolds stress of the TV exhibits a bi-modal two-lobed, axisymmetric distribution.

With suction plasma control at $\alpha = 10°$, see Fig. 6.3a, the shear layer

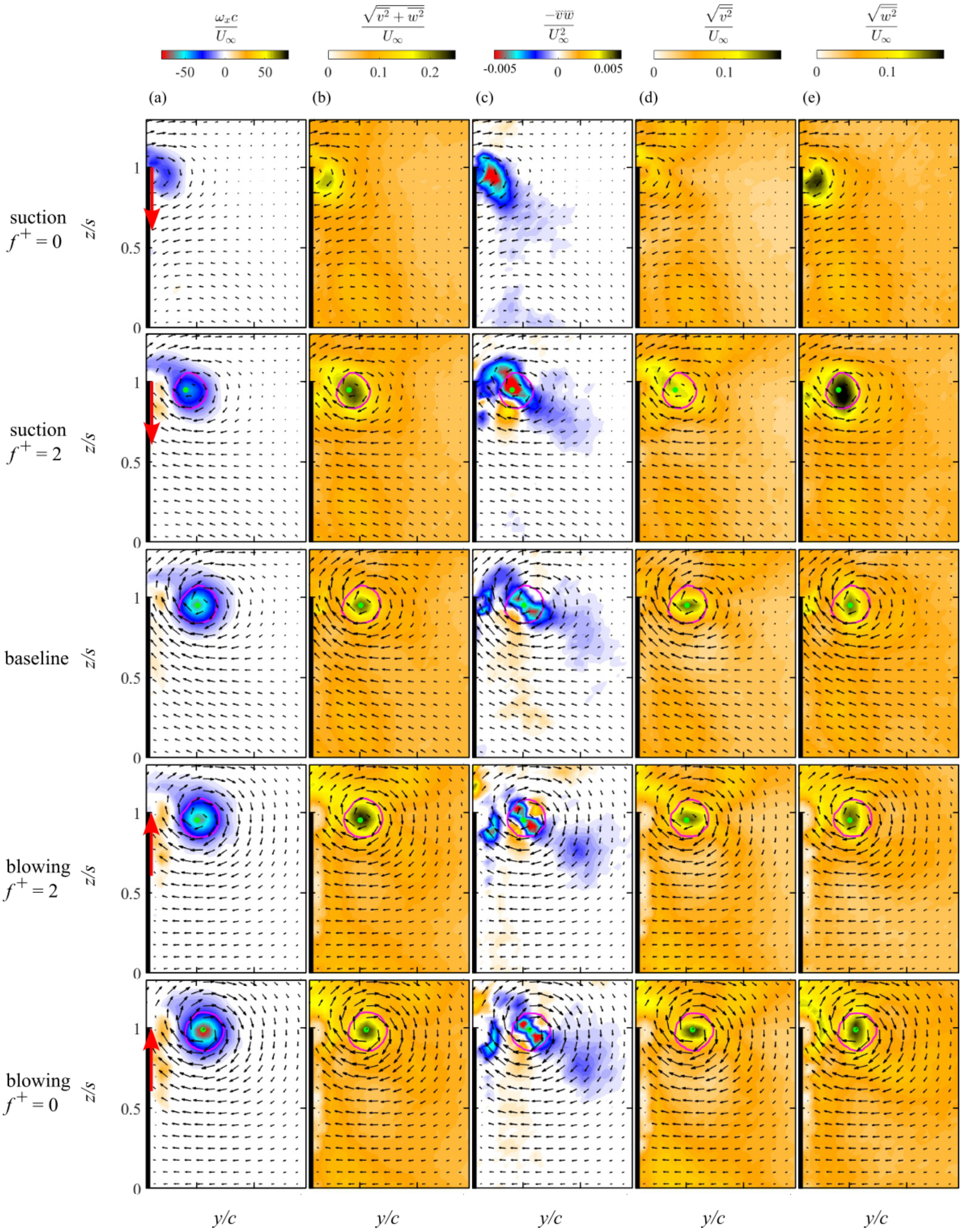

Figure 6.3: Influence of the plasma actuator on the TV compared to the baseline case at $\alpha = 10°$ at the mid-chord: (a) the vorticity field, (b) the turbulent intensity, (c) the Reynolds stress, (d) V-component turbulent intensity and (e) W-component turbulent intensity. Red arrows indicate the location and direction of the plasma jets.

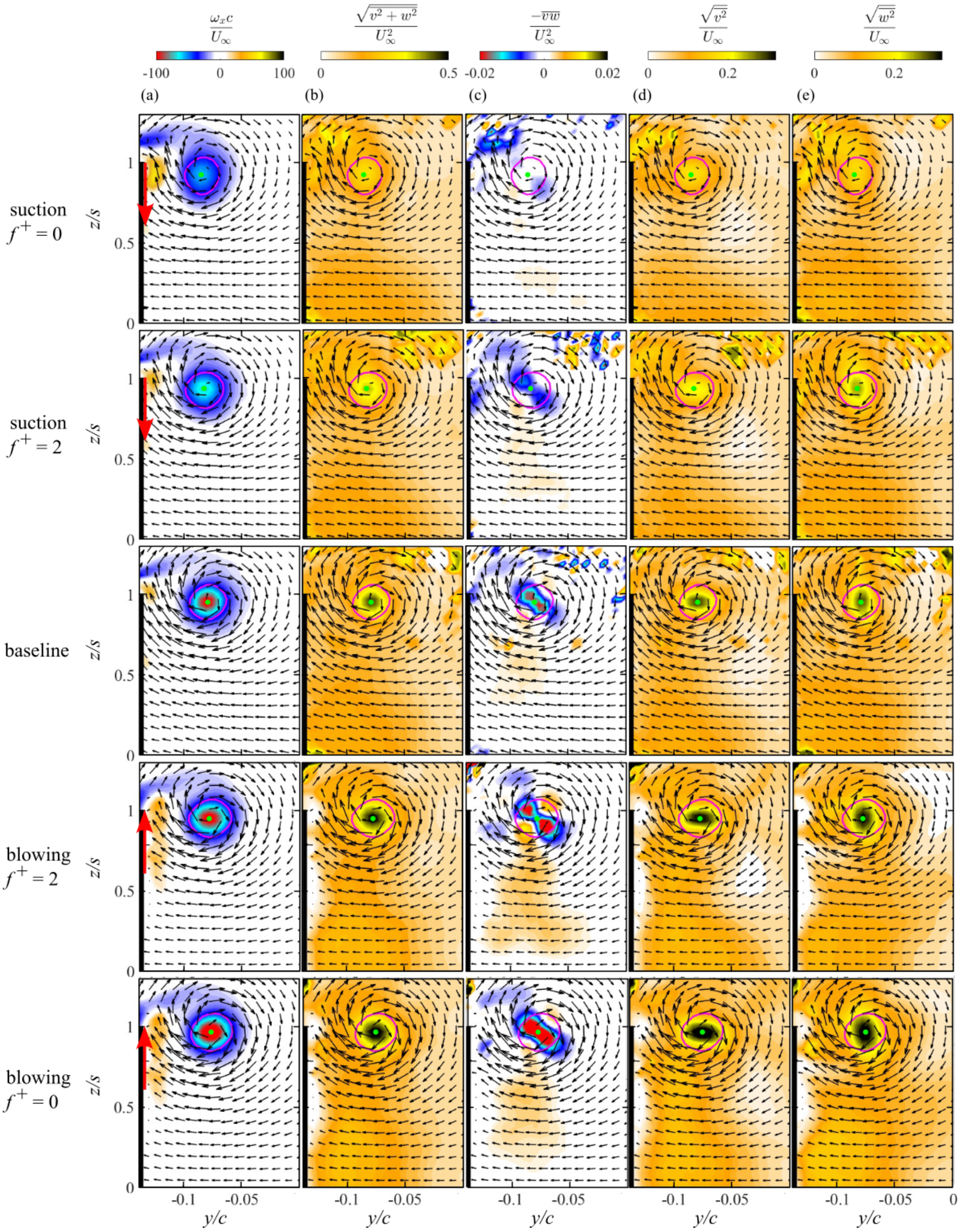

Figure 6.4: Same as Fig. 6.3 but at $\alpha = 15°$.

is forced to move around the wing wall, reducing the flow separation at the wing tip. Particularly when the suction plasma is operated at a steady mode ($f^+ = 0$), the shear layer is reattached to the suction side of the wing surface, creating a small separation bubble. This makes the TV weaker with low vorticity. It is interesting to observe that the turbulent intensity (Fig. 6.3b) and the Reynolds stress (Fig. 6.3c) here are increased with the suction plasma. The distribution of the Reynolds stress in the vortex core is no longer bi-modal two-lobed. The strong Reynolds stress appears at the junction of the separated shear layer and the TV, suggesting an enhanced turbulent mixing there. This is due to a large increase in the W-component turbulent intensity, since the V-component turbulent intensity is reduced by the suction plasma. For the blowing control, there is no evident movement of the shear layer but the vorticity, turbulent intensity and the Reynolds stress within the TV core are all increased. Here, the increase in the vorticity inside the TV is partly attributed to the added momentum by the blowing plasma jet, which increased the strength of the separated shear layer at the wing tip. In addition, the plasma jet velocity is in the same direction as the TV circulation, which increases the vorticity as well as the turbulence intensities and the Reynolds stress.

At $\alpha = 15°$ (Fig. 6.4), the blowing control shows similar results as those at $\alpha = 10°$, by increasing the vorticity, the turbulent intensity and the Reynolds stress within and around the TV core. For the suction control, however, the turbulent intensity and the Reynolds stress are reduced, since both V- and W-component turbulence intensities are reduced at the same time. We note that the wall-ward movement of the shear layer due to suction is much weaker at $\alpha = 15°$ as compared to the suction control results at $\alpha = 10°$. However, a small separation bubble is still observed near the wing tip with the suction plasma. The suction plasma jet is

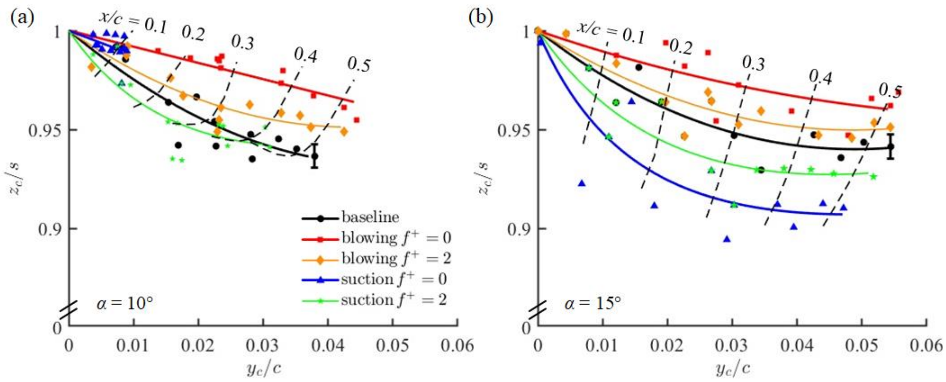

Figure 6.5: Change of the vortex locus under the influence of plasma actuators: (a) $\alpha = 10°$ and (b) $\alpha = 15°$.

directed in an opposite direction to the TV circulation, reducing the TV vorticity as well as the turbulence intensities and the Reynolds stress.

Figure 6.5 shows the locus of the vortex core during the downstream development of the TV in the (y_c/c, z_c/s) plane, where y_c/c and z_c/s are the local non-dimensional coordinates for the vortex core measured from the wing surface and the mid-span, respectively. At $\alpha = 10°$, the locus of the TV core with a steady suction plasma ($f^+ = 0$) remains within $0 < y_c/c < 0.01$ and $0.99 < z_c/s < 1$ (Fig. 6.5a), as the TV is pulled towards the wing surface to form a separation bubble as shown in Fig. 6.3a. The TV locus is also shifted towards the wing surface ($y_c/c = 0$) with a pulsed suction plasma ($f^+ = 2$), although a separation bubble is not observed in this case. On the other hand, the vortex core is shifted away from the wing surface and the mid-span by blowing plasma control ($f^+ = 0$ and 2). A similar plasma control behaviour can be observed at $\alpha = 15°$, although the vortex core does not stay near the wing surface with a suction plasma at this AoA.

The influence of the plasma actuators on the TV circulation along the wing chord is shown by an integral of the vorticity inside the TV core identified by the λ_2-criterion, see Fig. 6.6. Note that the result for the steady suction

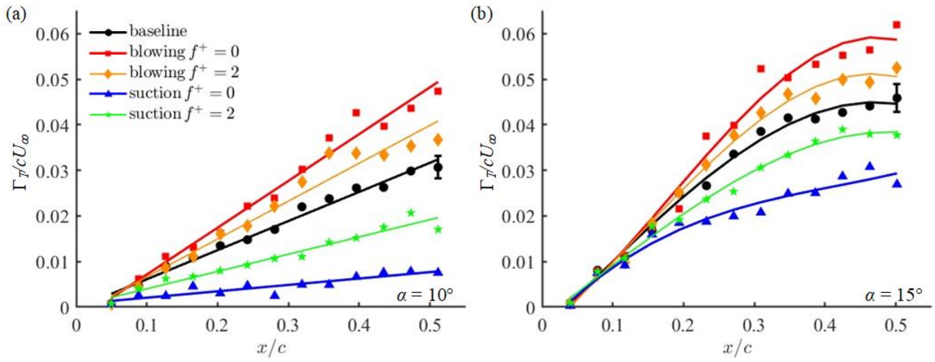

Figure 6.6: Effect of the plasma actuators on the TV circulation along the chord at $\alpha = 10°$ and $\alpha = 15°$.

plasma actuator has a large uncertainty due to the difficulty in identifying the TV core near the wing surface, see Fig. 6.3. The circulation of the TV increases nearly linearly with x/c at $\alpha = 10°$, while the linear circulation growth is limited to $x/c < 0.35$ at $\alpha = 15°$. These results are in good agreement with DeVoria and Mohseni (2017a) at $Re = 8 \times 10^4$ and Dong et al. (2020) $Re = 2 \times 10^5$. As demonstrated in Figs. 6.3 and 6.4, the circulation of the TV is reduced by the suction plasma and increased by the blowing plasma. Indeed, suction plasma control of the TV is very effective at $\alpha = 10°$, where the TV circulation is reduced by 75% and 39% at $f^+ = 0$ and 2, respectively, see Fig. 6.6a. Meanwhile, the increase in the TV circulation by blowing plasma control is 53% and 26% by $f^+ = 0$ and 2, respectively. Increasing AoA to $\alpha = 15°$, the effectiveness of the suction and blowing plasma becomes less but similar to each other with a 33% change (reduction or increase) at $f^+ = 0$ and a 14% change at $f^+ = 2$. A reduction in the control effectiveness of the plasma actuators at $\alpha = 15°$ is due to the reduced velocity ratio of the plasma jet to the W-velocity component of the separated shear layer at the wing tip. While the plasma jet velocity remains constant, the W-velocity component of the separated shear layer is increased with an increase in the AoA.

To qualify how the plasma actuator affects the vorticity transport, the

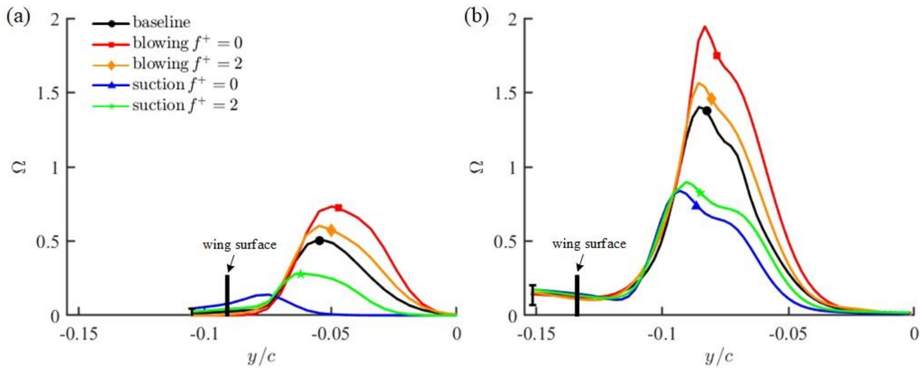

Figure 6.7: The vorticity flux Ω between $z/s = 0.75$ and 1.25 at the mid-chord ($x/c = 0.5$) at $\alpha = 10°$ (a) and $\alpha = 15°$ (b). Solid symbols on each line indicate the location of the vortex centroid.

time-averaged vorticity flux at the mid-chord ($x/c = 0.5$) is shown in Fig. 6.7 as a function of y/c. Here, the vorticity flux Ω is defined by $\Omega = -\int \omega_x \sqrt{V^2 + W^2} \mathrm{d}z/U_\infty^2$, where the integral of the streamwise vorticity times the local velocity magnitude is performed excluding the contribution of the secondary vorticity between $z/s = 0.75$ and 1.25. A steady suction plasma ($f^+ = 0$) increases the vorticity flux close to the wing surface ($y/c < -0.075$) at $\alpha = 10°$, see Fig. 6.7a. However, there are only small changes in the vorticity flux due to a pulsed suction plasma ($f^+ = 2$) or the blowing plasma ($f^+ = 0$ and 2) in this region. Away from the wing surface ($y/c > -0.075$), the vorticity flux is reduced by the suction plasma, while it is increased by the blowing plasma. Here, the peak as well as the maximum changes of the vortex flux due to plasma control are found at the centre of the vortex core ($y/c \cong -0.05$). With an increase in the AoA ($\alpha = 15°$), the vorticity flux is increased due to an increase in the streamwise vorticity generated in the separated shear layer as well as the increases in the V- and W-component velocities. Here, there are no appreciable changes in the vorticity flux near the wing surface ($y/c < -0.09$) due to plasma control. Away from the wing surface ($y/c > -0.09$), vortex flux is reduced by the suction plasma ($f^+ = 0$ and 2), while it is increased by the blowing plasma ($f^+ = 0$ and 2). Again, the peak as well as the

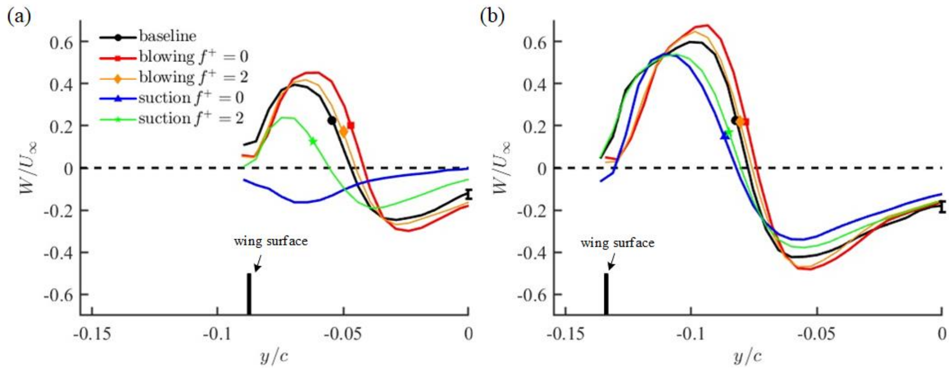

Figure 6.8: Effect of the plasma actuators on the W-component velocity of the TV from the wing surface across the vortex centroid at the mid-chord ($x/c = 0.5$): (a) $\alpha = 10°$ and (b) $\alpha = 15°$. Solid symbols on each line indicate the location of the vortex centroid.

maximum changes of the vortex flux due to plasma control are found at the centre of the vortex core, which is at $y/c \cong -0.08$ at $\alpha = 15°$.

The W-component velocity distributions across the vortex centroid at the mid-chord ($x/c = 0.5$) are shown in Fig. 6.8. Considering that the TV core is located at $y/c \cong -0.05$ and $y/c \cong -0.08$ for $\alpha = 10°$ and $\alpha = 15°$, respectively, the W-component velocity in Fig. 6.8 represents the circumferential velocity of the TV around the vortex core. With plasma control, the near-wall side of the W-component velocity is increased by the blowing plasma, while it is reduced by the suction plasma. As a result, the TV circulation is increased by blowing control, while it is reduced by suction control. In other words, the blowing plasma increases the TV circulation by co-flowing with the TV, while the TV circulation is reduced by the counter-flowing suction plasma. This suggests that the plasma jet-flow direction relative to the TV circulation is critical in controlling the TVs over a very low AR wing. This seems to be the mechanism of TV circulation control using plasma actuators, which in turn affects the aerodynamic forces of a very low AR wing (Fig. 6.1). Since the changes in the vorticity flux are only seen away from the wall (Fig. 6.7), the separated shear layer is not affected by the plasma actuators except for the steady suction plasma ($f^+ = 0$),

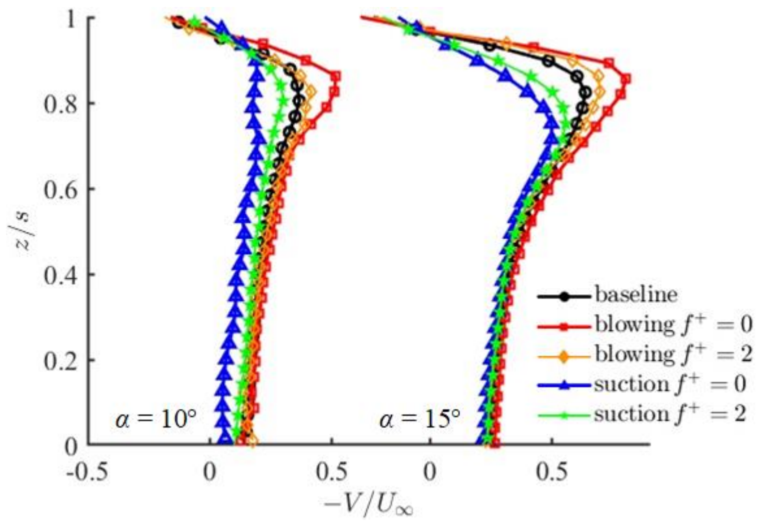

Figure 6.9: Effect of the plasma actuators on the V-component velocity from the wing tip across the vortex centroid to the mid-span at the mid-chord ($x/c = 0.5$) with different AoAs.

where the shear layer is bent over the wing tip to form a separation bubble, see Fig. 6.3a.

The V-component velocity profiles across the vortex centroid are plotted from the wing tip to the mid-span in Fig. 6.9, showing the circumferential velocity of the TV. Similar to the W-component velocity which also shows the circumferential velocity of the TV (Fig. 6.8), the magnitude of the V-component velocity is reduced by suction plasma control, while it is increased by blowing plasma control. It should be noted that the circumferential velocity distribution extends to the mid-span ($z/s = 0$). Here, the effect of plasma control is seen not only around the vortex core, but also near the mid-span ($z/s = 0$). In other words, the plasma control can influence the entire flow domain over the wing. It is also noted that the V-component velocity reaches its maximum value closer to the wing tip with the blowing control and to the mid-span with the suction control. The shift of the peak velocity location is due to the movement of the vortex core by plasma control, as demonstrated in Fig. 6.5.

Figure 6.10 shows the influence of plasma control on the U-component ve-

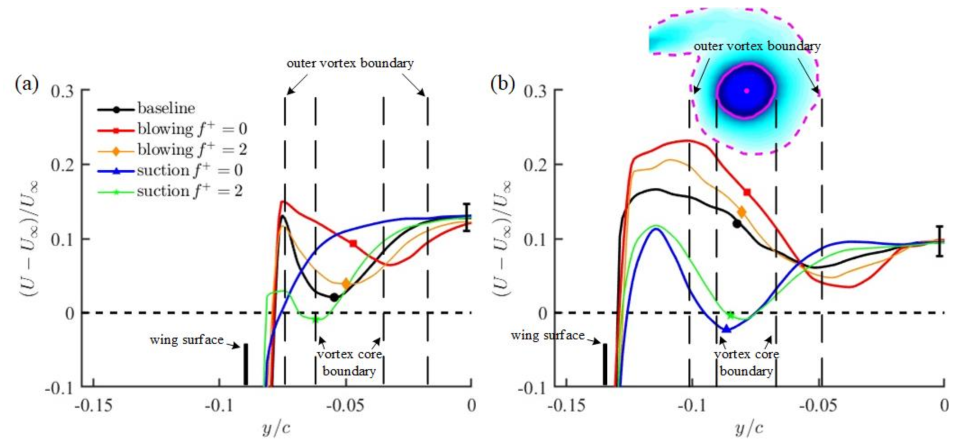

Figure 6.10: Effect of the plasma actuators on the U-component velocity of the TV from the wing surface across the vortex centroid at the mid-chord: (a) $\alpha = 10°$ and (b) $\alpha = 15°$. The vortex shown is for the baseline, where outer vortex boundary corresponds to $\omega_x c/U_\infty = -5$. Solid symbols on each line indicate the location of the vortex centroid.

locity of the TV at $\alpha = 10°$ and $\alpha = 15°$, where the TV centroid and core boundary are marked based on the λ_2-criterion as discussed previously. The vorticity of the TV extends to the outer vortex boundary (Skinner et al., 2020), although the majority is found within the vortex core. Here, the boundary of the outer vortex is defined by the non-dimensional vorticity at $\omega_x c/U_\infty = -5$. The U-component velocity increases sharply from the wing surface and peaks somewhere before entering the outer vortex boundary, which probably is due to the flow acceleration around the wing tip. Thereafter, the U-component velocity reduces inside the TV, followed by a gradual increase, eventually reaching a final value of around $1.1U_\infty$ outside the outer vortex. When the TV is controlled by a steady suction plasma ($f^+ = 0$) at $\alpha = 10°$, the axial velocity increases monotonically, which is due to the reattachment of the separated shear layer as shown in Fig. 6.3. The other plasma control cases give a similar velocity profile as the baseline, although the U-component velocity is reduced by the suction plasma and increased by the blowing plasma up to the far-side vortex core boundary at $y/c = -0.05$ at $\alpha = 10°$ and $y/c = -0.056$ at $\alpha = 15°$. Outside the far-side vortex core boundary, the U-component velocity is increased by the suction plasma, while it is reduced by the blowing plasma. The jet-like U-component velocity profiles shown in Fig. 6.10 seem to suggest that vortex breakdown is not yet taking place at these AoAs. Noteworthy is that the U-component velocity inside the vortex core nearly becomes wake-like by the suction plasma. These results show a possibility that the plasma actuator can also be used to trigger or delay the TV breakdown.

Chapter 7

Conclusions

The aerodynamics and vortical structures of a very low aspect ratio (AR = 0.277) wing are investigated in a wind tunnel at the effective Reynolds number of 3×10^6, which is quite different from the large AR and 2D wings. We find that the circulation of the leading-edge vortex increases with an increase in the AoA. The contribution of the leading-edge vortex on the total lift is approximately 30% at $\alpha = 20.7°$ to $40.5°$. The behaviour of the LEV is studied in the light of the downwash induced by the TV. At a small AoA, the flow over the wing is fully attached. With an increase in the AoA, the separated shear layer starts to roll up forming the LEV, whose reattachment point moves downstream. Afterward, the LEV is pushed upstream due to the downwash of the TV, increasing the circulation of the LEV at the same time. At a very large AoA, the downwash velocity close to the wing surface starts to decrease, reverting the movement of the LEV downstream with a further increase in the AoA. These results clearly show that the TV over a very low AR wing induces strong downwash to influence the development of the LEV to delay flow separation. Vortex interactions are found near the leading-edge, corresponding to the intense turbulent mixing indicated by high Reynolds stress. The circulation, core position and diameter of the tip-vortex are obtained and expressed in terms of the AoA and the distance from the leading-edge. Meanwhile, The vortex wandering phenomenon of the tip vortex is observed, affecting the stability of the low aspect-ratio thin wing.

The effect of pitching motion on a very low AR wing is also different as compared with that on the large AR and 2D wings. When applying pitch-up motion, with pivots at the mid-chord, the maximum lift angle is increased with an increase in the non-dimensional pitch rate K, but the maximum lift coefficient is slightly reduced. This result contradicts the finding of Granlund et al. (2013), who showed that the lift coefficient C_L of a pitching wing was proportional to $(0.75 - x_p)K$, where x_p is the non-dimensional pivot position along the chord. This suggests that different flow physics are at play in the aerodynamics of a very low AR pitching wing, where the induced velocity of the TV helps reattach the separated flow and maintains the LEV.

Detailed PIV measurements of the flow over a pitching wing show that there is a phase lag in the TV development, which increases with an increase in the pitch rate K. Here, the phase lag is defined as the difference in the pitch angle between the stationary wing and the pitch-up wing to reach the same circulation. It is also observed that the phase lag of the LEV is nearly identical to that of the TV, confirming that the dynamic of the LEV is strongly influenced by the TV. After the phase lag is taken into account, we observe a similarity in the development of the TV and LEV over a very low AR wing between the stationary and pitching conditions.

Vortex breakdown of the TV takes place at the phase-lag adjusted AoA of $\alpha^* = 32^\circ$ at the mid-chord. During the vortex breakdown, the diameter of the TV increases rapidly, where the vorticity distribution at the periphery of the TV shows wavy edges typical of the vortex instability. The axial velocity of the TV is greater than the freestream velocity before the vortex breakdown, forming a jet-like vortex core. After the vortex breakdown, however, this changes to a wake-like core with velocity deficit. The location of the vortex breakdown shifts upstream nearly linearly along the wing chord with an increase in the AoA.

Flow control of the TVs over a very low AR wing is carried out using the DBD plasma actuators, where the steady and pulsed blowing and suction plasma are examined. The results indicate a large change in the aerodynamic forces by plasma flow control, where the lift coefficient is increased by the steady blowing plasma by 23% at the AoA of 8°, while it is reduced by the steady suction plasma by 30%. With a pulsed mode of plasma actuation, the control effect is reduced, where only a 13% increase and a 16% reduction in the lift coefficient are achieved by the blowing and suction plasma, respectively. This is due to the fact that the plasma momentum coefficient of the steady mode of actuation is about twice that of the pulsed mode of plasma actuation, which is operating at 50% of the duty cycle. Compared to the lift coefficient, the change of the drag coefficient is less than 10% for all cases with the plasma actuator. The changes in the aerodynamic forces observed in the present investigation are mainly due to the changes in the vortex lift as a result of the plasma control on the TV circulation. Effect of the plasma actuators on the interaction between LEV and TV is too small to detect since the TV stays very close to the wing tip at the angles of attack being investigated here.

With the blowing plasma the TV moves outboard away from the wing tip, increasing the streamwise vorticity and the turbulence intensities as well as the Reynolds stress. With the suction plasma, the TV is shifted inboard closer to the wing tip. With a steady suction control at $\alpha = 10°$, the separated shear layer is bent around the wing tip, reattaching to the suction side of the wing surface to create a separation bubble. Indeed, the suction plasma is very effective in controlling the TV, reducing the TV circulation by up to 75% at $\alpha = 10°$. Meanwhile, the blowing plasma increased the TV circulation by up to 53%. At $\alpha = 15°$, the effectiveness of the suction and blowing plasma is reduced, which is due to the reduced velocity ratio of the plasma jet to the W-velocity component of the separated shear layer at the wing tip. Co-flowing with the TV, the blowing plasma increases the TV circulation, while it is reduced by the counter-flowing suction plasma. This suggests that the plasma jet-flow direction relative to the TV circulation is critical in controlling the TVs over a very low AR wing. Observed changes in the U-component velocity by plasma control suggest an interesting possibility that the TV breakdown can be manipulated to influence the aerodynamic characteristics.

The main objective of this study is to investigate the TV behaviour in the presence of the plasma actuators and to understand the associated flow control mechanism. This was achieved by dealing with the TV at only one side of the wing. The results indicate that the control effect is isolated to the close vicinity of the wind tip. Therefore, a significant interaction between the two TVs on either side of the wing is unlikely at least at the angles of attack being investigated here. We, therefore, expect that the effect of plasma actuators on the aerodynamic forces on a very low AR wing would be nearly doubled if both wing tips are simultaneously controlled. Although plasma control is carried out on the TVs over a very low AR wing, a similar plasma control strategy can be applied to the leading-edge vortices over delta wings.

References

Agrawal, S., Barnett, R. M., and Robinson, B. A. (1992). Numerical investigation of vortex breakdown on a delta wing. *AIAA J.*, 30(3):584–591.

Akkala, J. M. and Buchholz, J. H. J. (2017). Vorticity transport mechanisms governing the development of leading-edge vortices. *J. Fluid Mech.*, 829:512–537.

Amiralaei, M., Alighanbari, H., and Hashemi, S. (2010). An investigation into the effects of unsteady parameters on the aerodynamics of a low Reynolds number pitching airfoil. *J. Fluids Struct.*, 26(6):979–993.

Anderson Jr, J. D. (2010). *Fundamentals of aerodynamics*. Tata McGraw-Hill Education.

Asghar, A. and Jumper, E. (2003). Phase synchronization of vortex shedding from multiple cylinders using plasma actuators. In *41st Aerospace Sciences Meeting and Exhibit*.

Ashpis, D. E. and Thurman, D. R. (2019). Dielectric barrier discharge (DBD) plasma actuators for flow control in turbine engines: Simulation of flight conditions in the laboratory by density matching. *Int. J. Turbo. Jet. Engines*, 36(2):157–173.

Ashraf, M., Young, J., and Lai, J. (2009). Effect of airfoil thickness, camber and Reynolds number on plunging airfoil propulsion. In *47th AIAA*

Aerospace Sciences Meeting Including the New Horizons Forum and Aerospace Exposition.

Baik, Y. S., Bernal, L. P., Granlund, K., and Ol, M. V. (2012). Unsteady force generation and vortex dynamics of pitching and plunging aerofoils. *J. Fluid Mech.*, 709:37–68.

Bailey, S. and Tavoularis, S. (2008). Measurements of the velocity field of a wing-tip vortex, wandering in grid turbulence. *J. Fluid Mech.*, 601:281–315.

Bailey, S. C. C., Tavoularis, S., and Lee, B. H. K. (2006). Effects of freestream turbulence on wing-tip vortex formation and near field. *J. Aircr.*, 43(5):1282–1291.

Batchelor, G. K. (1964). Axial flow in trailing line vortices. *J. Fluid Mech.*, 20(4):645–658.

Billant, P., Chomaz, J.-M., and Huerre, P. (1998). Experimental study of vortex breakdown in swirling jets. *J. Fluid Mech.*, 376:183–219.

Birch, D. and Lee, T. (2005). Investigation of the near-field tip vortex behind an oscillating wing. *J. Fluid Mech.*, 544:201–241.

Birnbaum, W. (1924). Das ebene problem des schlagenden flügels. *Z. Angew. Math. Mech.*, 4(4):277–292.

Boesch, G., Vo, H. D., Savard, B., Wanko-Tchatchouang, C., and Mureithi, N. W. (2010). Flight control using wing-tip plasma actuation. *J. Aircr.*, 47(6):1836–1846.

Bohl, D. G. and Koochesfahani, M. M. (2009). MTV measurements of the vortical field in the wake of an airfoil oscillating at high reduced frequency. *J. Fluid Mech.*, 620:63–88.

Boiko, A. V., Dovgal, A. V., Grek, G. R., and Kozlov, V. V. (2011). *Physics of Transitional Shear Flows: Instability and Laminar–Turbulent Transition in Incompressible Near-Wall Shear Layers*. Springer Science.

Bross, M., Ozen, C., and Rockwell, D. (2013). Flow structure on a rotating wing: effect of steady incident flow. *Phys. Fluids*, 25(8):081901.

Buchholz, J. H. and Smits, A. J. (2006). On the evolution of the wake structure produced by a low-aspect-ratio pitching panel. *J. Fluid Mech.*, 546:433–443.

Buchholz, J. H. and Smits, A. J. (2008). The wake structure and thrust performance of a rigid low-aspect-ratio pitching panel. *J. Fluid Mech.*, 603:331–365.

Cattafesta III, L. N. and Sheplak, M. (2011). Actuators for active flow control. *Annu. Rev. Fluid Mech.*, 43:247–272.

Chandrsuda, C. and Bradshaw, P. (1981). Turbulence structure of a reattaching mixing layer. *J. Fluid Mech.*, 110:171–194.

Chappell, S. and Angland, D. (2012). Active control of a wing tip vortex with a dielectric barrier discharge plasma actuator. In *6th AIAA Flow Control Conference*.

Chigier, N. A. (1974). Vortexes in aircraft wakes. *Sci. Am.*, 230(3):76–83.

Chong, M. S., Perry, A. E., and Cantwell, B. J. (1990). A general classification of three-dimensional flow fields. *Phys. Fluids*, 2(5):765–777.

Choudhuri, P. G. and Knight, D. (1996). Effects of compressibility, pitch rate, and Reynolds number on unsteady incipient leading-edge boundary layer separation over a pitching airfoil. *J. Fluid Mech.*, 308:195–217.

Cloupeau, M., Devillers, J., and Devezeaux, D. (1979). Direct measurements of instantaneous lift in desert locust; comparison with jensen's experiments on detached wings. *J. Exp. Biol.*, 80(1):1–15.

Corke, T., Jumper, E., Post, M., Orlov, D., and McLaughlin, T. (2002). Application of weakly-ionized plasmas as wing flow-control devices. In *40th AIAA Aerospace Sciences Meeting and Exhibit*.

Corke, T. C., Enloe, C. L., and Wilkinson, S. P. (2010). Dielectric barrier discharge plasma actuators for flow control. *Annu. Rev. Fluid Mech.*, 42:505–529.

Corsiglia, V., Schwind, R., and Chigier, N. (1973). Rapid scanning, three-dimensional hot-wire anemometersurveys of wing-tip vortices. *J. Aircr.*, 10(12):752–757.

Das, A., Shukla, R. K., and Govardhan, R. N. (2016). Existence of a sharp transition in the peak propulsive efficiency of a low-pitching foil. *J. Fluid Mech.*, 800:307–326.

Deng, J., Caulfield, C., and Shao, X. (2014). Effect of aspect ratio on the energy extraction efficiency of three-dimensional flapping foils. *Phys. Fluids*, 26(4):043102.

Deparday, J. and Mulleners, K. (2019). Modeling the interplay between the shear layer and leading edge suction during dynamic stall. *Phys. Fluids*, 31(10):107104.

DeVoria, A. C. and Mohseni, K. (2017a). On the mechanism of high-incidence lift generation for steadily translating low-aspect-ratio wings. *J.Fluid Mech.*, 813:110–126.

DeVoria, A. C. and Mohseni, K. (2017b). A vortex model for forces and moments on low-aspect-ratio wings in side-slip with experimental validation. *Proc. R. Soc. A.*, 473:20160760.

Doligalski, T., Smith, C., and Walker, J. (1994). Vortex interactions with walls. *Annu. Rev. Fluid Mech.*, 26(1):573–616.

Dong, H. and Liang, Z. (2010). Effects of ipsilateral wing-wing interactions on aerodynamic performance of flapping wings. In *48th AIAA Aerospace Sciences Meeting Including the New Horizons Forum and Aerospace Exposition*.

Dong, L., Choi, K.-S., and Mao, X. R. (2020). Interplay of the leading-edge vortex and the tip vortex of a low-aspect-ratio thin wing. *Exp. Fluids*, 61(9):1–15.

Dong, L., Gao, G., Peng, K., Wei, W., Li, C., and Wu, G. (2017). Effects of surface dielectric barrier discharge on aerodynamic characteristic of train. *AIP Adv.*, 7(7):075112.

Eldredge, J. D., Toomey, J., and Medina, A. (2010). On the roles of chordwise flexibility in a flapping wing with hovering kinematics. *J. Fluid Mech.*, 659:94–115.

Ellington, C. P., Van Den Berg, C., Willmott, A. P., and Thomas, A. L. (1996). Leading-edge vortices in insect flight. *Nature*, 384(6610):626–630.

Eppler, R. (1990). Airfoil data. In *Airfoil Design and Data*, pages 163–512. Springer.

Feng, L.-H., Choi, K.-S., and Wang, J.-J. (2015). Flow control over an airfoil using virtual gurney flaps. *J. Fluid Mech.*, 767:595–626.

Forte, M., Jolibois, J., Pons, J., Moreau, E., Touchard, G., and Cazalens, M. (2007). Optimization of a dielectric barrier discharge actuator by stationary and non-stationary measurements of the induced flow velocity: application to airflow control. *Expe. Fluids*, 43(6):917–928.

Freymuth, P., Finaish, F., and Bank, W. (1987). Further visualization of combined wing tip and starting vortex systems. *AIAA J.*, 25(9):1153–1159.

Gaster, M. (1967). *The structure and behaviour of laminar separation bubbles*. Citeseer.

Gault, D. E. (1957). A correlation of low-speed, airfoil-section stalling characteristics with Reynolds number and airfoil geometry. *NACA TN 3963*.

Gendrich, C. P. (1999). *Dynamic stall of rapidly pitching airfoils: MTV experiments and Navier-Stokes simulations*. Michigan State University.

Gerrard, J. (1966). The mechanics of the formation region of vortices behind bluff bodies. *J. Fluid Mech.*, 25(2):401–413.

Gharali, K. and Johnson, D. A. (2014). PIV-based load investigation in dynamic stall for different reduced frequencies. *Exp. Fluids*, 55(8):1–12.

Giuni, M. (2013). *Formation and early development of wingtip vortices*. PhD thesis, University of Glasgow.

Gkiolas, D., Yiasemides, D., and Mathioulakis, D. (2018). Experimental study of a pitching and plunging wing. *Aircr. Eng. Aerosp. Tec.*

Gordnier, R. E. and Visbal, M. R. (1994). Unsteady vortex structure over a delta wing. *J. Aircr.*, 31(1):243–248.

Graftieaux, L., Michard, M., and Grosjean, N. (2001). Combining PIV, POD and vortex identification algorithms for the study of unsteady turbulent swirling flows. *Meas. Sci. Technol.*, 12(9):1422.

Granlund, K. O., Ol, M. V., and Bernal, L. P. (2013). Unsteady pitching flat plates. *J. Fluid Mech.*, 733.

Green, S. I. (1995). Wing tip vortices. In *Fluid vortices*, pages 427–469. Springer.

Greenblatt, D., Kastantin, Y., Nayeri, C., and Paschereit, C. (2008). Delta-wing flow control using dielectric barrier discharge actuators. *AIAA J.*, 46(6):1554–1560.

Greenblatt, D., Schneider, T., and Schüle, C. Y. (2012). Mechanism of flow separation control using plasma actuation. *Phys. Fluids*, 24(7):077102.

Greenblatt, D. and Wygnanski, I. J. (2000). The control of flow separation by periodic excitation. *Prog. Aerosp. Sci.*, 36(7):487–545.

Grundmann, S. and Tropea, C. (2007). Experimental transition delay using glow-discharge plasma actuators. *Exp. Fluids*, 42(4):653–657.

Gupta, R. and Ansell, P. J. (2019). Unsteady flow physics of airfoil dynamic stall. *AIAA J.*, 57(1):165–175.

Gursul, I. (2004). Recent developments in delta wing aerodynamics. *Aeronaut. J.*, 108(1087):437–452.

Gursul, I., Gordnier, R., and Visbal, M. (2005). Unsteady aerodynamics of nonslender delta wings. *Prog. Aerosp. Sci.*, 41(7):515–557.

Hasebe, H., Naka, Y., and Fukagata, K. (2011). An attempt for suppression of wing-tip vortex using plasma actuators. *J. Fluid Sci. Technol.*, 6(6):976–988.

He, C., Corke, T. C., and Patel, M. P. (2009). Plasma flaps and slats: an application of weakly ionized plasma actuators. *J. Aircr.*, 46(3):864–873.

Henderson, W. P. and Holmes, B. J. (1989). Induced drag-historical perspective. Technical report, SAE Technical Paper.

Hoffmann, E. R. and Joubert, P. N. (1963). Turbulent line vortices. *J. Fluid Mech.*, 16(3):395–411.

Hosseinverdi, S. and Fasel, H. F. (2019). Numerical investigation of laminar–turbulent transition in laminar separation bubbles: the effect of free-stream turbulence. *J. Fluid Mech.*, 858:714–759.

Istvan, M. S. and Yarusevych, S. (2018). Effects of free-stream turbulence intensity on transition in a laminar separation bubble formed over an airfoil. *Exp. Fluids*, 59(3):1–21.

Jacquin, L., Fabre, D., Geffroy, P., and Coustols, E. (2001). The properties of a transport aircraft wake in the extended near field-an experimental study. In *39th Aerospace Sciences Meeting and Exhibit*.

Jeong, J. and Hussain, F. (1995). On the identification of a vortex. *J. Fluid Mech.*, 285:69–94.

Jian, T. and Ke-Qin, Z. (2004). Numerical and experimental study of flow structure of low-aspect-ratio wing. *J. Aircr.*, 41(5):1196–1201.

Jiang, M., Machiraju, R., and Thompson, D. (2005). Detection and visualization of vortices. *The visualization handbook*, 295.

Jones, L., Sandberg, R., and Sandham, N. (2010). Stability and receptivity characteristics of a laminar separation bubble on an aerofoil. *J. Fluid Mech.*, 648:257–296.

Jukes, T., Choi, K.-S., Johnson, G., and Scott, S. (2006). Turbulent drag reduction by surface plasma through spanwise flow oscillation. In *Collection of Technical Papers - 3rd AIAA Flow Control Conference*, volume 3.

Jukes, T. N. and Choi, K.-S. (2009). Flow control around a circular cylinder using pulsed dielectric barrier discharge surface plasma. *Phys. Fluids*, 21(8):084103.

Jukes, T. N. and Choi, K.-S. (2013). On the formation of streamwise vortices by plasma vortex generators. *J. Fluid Mech.*, 733:370–393.

Kasagi, N. and Matsunaga, A. (1995). Three-dimensional particle-tracking velocimetry measurement of turbulence statistics and energy budget in a backward-facing step flow. *Int. J. Heat Fluid Flow*, 16(6):477–485.

Kim, D., Strom, B., Mandre, S., and Breuer, K. (2017). Energy harvesting performance and flow structure of an oscillating hydrofoil with finite span. *J. Fluids Struct.*, 70:314–326.

Kim, D.-H. and Chang, J.-W. (2010). Unsteady boundary layer for a pitching airfoil at low Reynolds numbers. *J. Mech. Sci*, 24(1):429–440.

Kinsey, T. and Dumas, G. (2008). Parametric study of an oscillating airfoil in a power-extraction regime. *AIAA J.*, 46(6):1318–1330.

Kline, S. and McClintock, F. (1953). Describing uncertainties in single-sample experiments. *Mech. Eng.*, 75:3–8.

Kogelschatz, U. (2003). Dielectric-barrier discharges: their history, discharge physics, and industrial applications. *Plasma Chem. Plasma Process.*, 23(1):1–46.

Kunihiko, T. and Colonius, T. (2009). Three-dimensional flows around low-aspect-ratio flat-plate wings at low Reynolds numbers. *J. Fluid Mech.*, 623:187–207.

Lamar, J. E. (1974). Extension of leading-edge-suction analogy to wings with separated flow around the side edges at subsonic speeds. *NASA TR R-428*.

Lambourne, N. and Bryer, D. (1961). The bursting of leading-edge vortices-some observations and discussion of the phenomenon. *Aero. Res. Counc.*

Lee, H., Kim, J.-H., and Kim, B.-S. (2002). PIV analysis of a delta wing flow with or without LEX (leading edge extension). In *Proc. of 11th Int. Symp. of Application of Laser Techniques to Fluid Mechanics*, pages 4–5.

Lee, T. and Gerontakos, P. (2004). Investigation of flow over an oscillating airfoil. *J. Fluid Mech.*, 512:313–341.

Leibovich, S. (1978). The structure of vortex breakdown. *Annu. Rev. Fluid Mech.*, 10(1):221–246.

Leishman, G. J. (2006). *Principles of helicopter aerodynamics*. Cambridge University Press.

Li, X., Feng, L.-H., and Li, Z.-Y. (2019). Flow mechanism for the effect of pivot point on the aerodynamic characteristics of a pitching airfoil and its manipulation. *Phys. Fluids*, 31(8):087108.

Little, J., Nishihara, M., Adamovich, I., and Samimy, M. (2010). High-lift airfoil trailing edge separation control using a single dielectric barrier discharge plasma actuator. *Exp. Fluids*, 48(3):521–537.

Lua, K.-B., Lai, K., Lim, T., and Yeo, K. (2010). On the aerodynamic characteristics of hovering rigid and flexible hawkmoth-like wings. *Exp. Fluids*, 49(6):1263–1291.

Ma, B.-F., Wang, Z., and Gursul, I. (2017). Symmetry breaking and instabilities of conical vortex pairs over slender delta wings. *J. Fluid Mech.*, 832:41–72.

Mackowski, A. and Williamson, C. (2017). Effect of pivot location and passive heave on propulsion from a pitching airfoil. *Phys. Rev. Fluids*, 2(1):013101.

Madnia, C. K. (2010). Review of "fundamentals of aerodynamics". *AIAA J.*, 48(12):2983–2983.

Marxen, O., Lang, M., Rist, U., and Wagner, S. (2003). A combined experimental/numerical study of unsteady phenomena in a laminar separation bubble. *Flow Turbul. Combust.*, 71(1):133–146.

Mary, I. (2003). Large eddy simulation of vortex breakdown behind a delta wing. *Int. J. Heat Fluid Flow*, 24(4):596–605.

McLaughlin, T., Munska, M., Vaeth, J., Dauwalter, T., Goode, J., and Siegel, S. (2004). Plasma-based actuators for cylinder wake vortex control. In *2nd AIAA flow Control Conference*.

Menke, M. and Gursul, I. (1997). Unsteady nature of leading edge vortices. *Phys. Fluids*, 9(10):2960–2966.

Michard, M., Graftieaux, L., Lollini, L., and Grosjean, N. (1997). Identification of vortical structures by a non local criterion- application to PIV measurements and DNS-LES results of turbulent rotating flows. In *Symposium on Turbulent Shear Flows, 11 th, Grenoble, France*, pages 28–25.

Mitchell, A. M. and Délery, J. (2001). Research into vortex breakdown control. *Prog. Aerosp. Sci.*, 37(4):385–418.

Moreau, E. (2007). Airflow control by non-thermal plasma actuators. *J. Phys. D: Appl. Phys.*, 40(3):605.

Mueller, T. J. and Batill, S. M. (1982). Experimental studies of separation on a two-dimensional airfoil at low Reynolds numbers. *AIAA J.*, 20(4):457–463.

Mueller, T. J. and DeLaurier, J. D. (2003). Aerodynamics of small vehicles. *Annu. Rev. Fluid Mech.*, 35(1):89–111.

Nabhan, M. B. (2018). Study of theoretical and numerical fluid characteristics of plain wing with winglets. In *IOP Conference Series: Materials Science and Engineering*, volume 370. IOP Publishing.

Ohmi, K., Coutanceau, M., Daube, O., and Loc, T. P. (1991). Further experiments on vortex formation around an oscillating and translating airfoil at large incidences. *J. Fluid Mech.*, 225:607–630.

Ohmi, K., Coutanceau, M., Loc, T. P., and Dulieu, A. (1990). Vortex formation around an oscillating and translating airfoil at large incidences. *J. Fluid Mech.*, 211:37–60.

Ol, M., Dong, H., and Webb, C. (2008). Motion kinematics vs. angle of attack effects in high-frequency airfoil pitch/plunge. In *38th Fluid Dynamics Conference and Exhibit*.

Ol, M. V., Bernal, L., Kang, C.-K., and Shyy, W. (2010). Shallow and deep dynamic stall for flapping low Reynolds number airfoils. In *Animal Locomotion*, pages 321–339. Springer.

Olson, D. A., Katz, A. W., Naguib, A. M., Koochesfahani, M. M., Rizzetta, D. P., and Visbal, M. R. (2013). On the challenges in experimental characterization of flow separation over airfoils at low Reynolds number. *Exp. Fluids*, 54(2):1–11.

Onoue, K. and Breuer, K. S. (2016). Vortex formation and shedding from a cyber-physical pitching plate. *J. Fluid Mech.*, 793:229–247.

Opaits, D., Roupassov, D., Starikovskaia, S., Starikovskii, A., Zavialov, I., and Saddoughi, S. (2005). Plasma control of boundary layer using low-temperature non-equilibrium plasma of gas discharge. In *43rd AIAA Aerospace Sciences Meeting and Exhibit*.

Owen, P. and Klanfer, L. (1953). On the laminar boundary layer separation from the leading edge of a thin aerofoil. Technical report, Aeronautical Research Council London (United Kingdom).

Ozen, C. A. and Rockwell, D. (2012). Three-dimensional vortex structure on a rotating wing. *J. Fluid Mech.*, 707:541–550.

Pelletier, A. and Mueller, T. J. (2000). Low Reynolds number aerodynamics of low-aspect-ratio, thin/flat/cambered-plate wings. *J. Aircr.*, 37(5):825–832.

Phillips, W. R. C. (1981). The turbulent trailing vortex during roll-up. *J. Fluid Mech.*, 105(451).

Polhamus, E. C. (1966). A concept of the vortex lift of sharp-edge delta wings based on a leading-edge-suction analogy. Technical report.

Polhamus, E. C. (1996). A survey of Reynolds number and wing geometry effects on lift characteristics in the low speed stall region. Technical report.

Post, M. L. and Corke, T. C. (2004). Separation control on high angle of attack airfoil using plasma actuators. *AIAA J.*, 42(11):2177–2184.

Ramasamy, M., Lee, T. E., and Leishman, J. G. (2007). Flowfield of a rotating-wing micro air vehicle. *J. Aircr.*, 44(4):1236–1244.

Robinson, M. and Wissler, J. (1988). Pitch rate and Reynolds number effects on a pitching rectangular wing. In *6th Applied Aerodynamics Conference*.

Rossow, V. J. (1978). Lift enhancement by an externally trapped vortex. *J. Aircr.*, 15(9):618–625.

Roth, J. R. (1995). Industrial plasma engineering. *IOP Publishing*, 1:366–367.

Roth, J. R. (2003). Aerodynamic flow acceleration using paraelectric and peristaltic electrohydrodynamic effects of a one atmosphere uniform glow discharge plasma. *Phys. Plasmas*, 10(5):2117–2126.

Roth, J. R. and Dai, X. (2006). Optimization of the aerodynamic plasma actuator as an electrohydrodynamic (ehd) electrical device. In *44th AIAA Aerospace Sciences Meeting and Exhibit*.

Saffman, P. G. (1995). *Vortex dynamics*. Cambridge University Press.

Santhanakrishnan, A., Jacob, J., and Suzen, Y. (2006). Flow control using plasma actuators and linear/annular plasma synthetic jet actuators. In *3rd AIAA Flow Control Conference*.

Saric, W. S., Reed, H. L., and Kerschen, E. J. (2002). Boundary-layer receptivity to freestream disturbances. *Annu. Rev. Fluid Mech.*, 34(1):291–319.

Sato, M., Nonomura, T., Okada, K., Asada, K., Aono, H., Yakeno, A., Abe, Y., and Fujii, K. (2015). Mechanisms for laminar separated-flow control using dielectric-barrier-discharge plasma actuator at low Reynolds number. *Phys. Fluids*, 27(11):117101.

Schlichting, H. (1955). *Boundary Layer Theory*. McGraw Hill.

Schreck, S. and Robinson, M. (2002). Rotational augmentation of horizontal axis wind turbine blade aerodynamic response. *Wind Energy*, 5(2-3):133–150.

Schreck, S. J. and Hellin, H. E. (1994). Unsteady vortex dynamics and surface pressure topologies on a finite pitching wing. *J. Aircr.*, 31(4):899–907.

Shah, P. N., Atsavapranee, P., Hsu, T. Y., Wei, T., and McHugh, J. (1999). Turbulent transport in the core of a trailing half-delta-wing vortex. *J. Fluid Mech.*, 387:151–175.

Shen, L. and Wen, C.-y. (2017). Leading edge vortex control on a delta wing with dielectric barrier discharge plasma actuators. *Appl. Phys. Lett.*, 110(25):251904.

Sidorenko, A. A., Budovskiy, A. D., Maslov, A. A., Postnikov, B. V., Zanin, B. Y., Zverkov, I. D., and Kozlov, V. V. (2013). Plasma control of vortex flow on a delta wing at high angles of attack. *Exp. Fluids*, 54(8):1–12.

Siemens, W. (1857). Ueber die elektrostatische induction und die verzögerung des stroms in flaschendrähten. *Ann. Phys.*, 178(9):66–122.

Simoni, D., Lengani, D., Ubaldi, M., Zunino, P., and Dellacasagrande, M. (2017). Inspection of the dynamic properties of laminar separation bubbles: free-stream turbulence intensity effects for different Reynolds numbers. *Exp. Fluids*, 58(6):1–14.

Simpson, B. J., Hover, F. S., and Triantafyllou, M. S. (2008). Experiments in direct energy extraction through flapping foils. In *The Eighteenth International Offshore and Polar Engineering Conference*.

Simpson, R. L. (1989). Turbulent boundary-layer separation. *Annu. Rev. Fluid Mech.*, 21(1):205–232.

Sinha, J., Lua, K. B., and Dash, S. M. (2021). Influence of the pivot location on the thrust and propulsive efficiency performance of a two-dimensional flapping elliptic airfoil in a forward flight. *Phys. Fluids*, 33(8):081912.

Skinner, S. N., Green, R. B., and Zare-Behtash, H. (2020). Wingtip vortex structure in the near-field of swept-tapered wings. *Phys. Fluids*, 32(9):095102.

Smith, L. R. and Jones, A. R. (2020). Vortex formation on a pitching aerofoil at high surging amplitudes. *J. Fluid Mech.*, 905.

Spalart, P. R. (1998). Airplane trailing vortices. *Annu. Rev. Fluid Mech.*, 30(1):107–138.

Storms, B. L. and Jang, C. S. (1994). Lift enhancement of an airfoil using a gurney flap and vortex generators. *J. Aircr.*, 31(3):542–547.

Strickland, J. H. and Graham, G. M. (1986). Dynamic stall inception correlation for airfoils undergoing constant pitch rate motions. *AIAA J.*, 24(4):678–680.

Sunada, S., Kawachi, K., Matsumoto, A., and Sakaguchi, A. (2001). Unsteady forces on a two-dimensional wing in plunging and pitching motions. *AIAA J.*, 39(7):1230–1239.

Taira, K. and Colonius, T. (2009). Three-dimensional flows around low-aspect-ratio flat-plate wings at low Reynolds numbers. *J. Fluid Mech.*, 623:187–207.

Tian, W., Bodling, A., Liu, H., Wu, J. C., He, G., and Hu, H. (2016). An experimental study of the effects of pitch-pivot-point location on the propulsion performance of a pitching airfoil. *J. Fluids Struct.*, 60:130–142.

Torres, G. E. and Mueller, T. (2004). Low-aspect-ratio wing aerodynamics at low Reynolds number. *AIAA J.*, 42(5):865–873.

Traub, L. W. (1997). Prediction of delta wing leading-edge vortex circulation and lift-curve slope. *J. Aircr.*, 34(3):450–452.

Triantafyllou, M. S., Triantafyllou, G., and Yue, D. (2000). Hydrodynamics of fishlike swimming. *Annu. Rev. Fluid Mech.*, 32(1):33–53.

Van den Berg, B. (1981). Role of laminar separation bubbles in airfoil leading-edge stalls. *AIAA J.*, 19(5):553–556.

Visbal, M. R. (2011). Numerical investigation of deep dynamic stall of a plunging airfoil. *AIAA J.*, 49(10):2152–2170.

Visbal, M. R. (2017). Unsteady flow structure and loading of a pitching low-aspect-ratio wing. *Phys. Rev. Fluids*, 2(2):024703.

Visbal, M. R. and Garmann, D. J. (2019a). Dynamic stall of a finite-aspect-ratio wing. *AIAA J.*, 57(3):962–977.

Visbal, M. R. and Garmann, D. J. (2019b). Effect of sweep on dynamic stall of a pitching finite-aspect-ratio wing. *AIAA J.*, 57(8):3274–3289.

Visser, K. and Nelson, R. (1993). Measurements of circulation and vorticity in the leading-edge vortexof a delta wing. *AIAA J.*, 31(1):104–111.

Von Ellenrieder, K. D., Parker, K., and Soria, J. (2003). Flow structures behind a heaving and pitching finite-span wing. *J. Fluid Mech.*, 490:129–138.

Vorobiev, A. N., Rennie, R. M., Jumper, E. J., and McLaughlin, T. E. (2008). Experimental investigation of lift enhancement and roll control using plasma actuators. *J. Aircr.*, 45(4):1315–1321.

Wang, C.-C., Durscher, R., and Roy, S. (2011). Three-dimensional effects of curved plasma actuators in quiescent air. *J. Appl. Phys.*, 109(8):083305.

Wang, J.-J., Choi, K.-S., Feng, L.-H., Jukes, T. N., and Whalley, R. D. (2013). Recent developments in DBD plasma flow control. *Prog. Aerosp. Sci.*, 62:52–78.

Wang, S., Zhou, Y., Alam, M. M., and Yang, H. X. (2014). Turbulent intensity and Reynolds number effects on an airfoil at low Reynolds numbers. *Phys. Fluids*, 26(11):115107.

Wang, Z. J. (2005). Dissecting insect flight. *Annu. Rev. Fluid Mech.*, 37:183–210.

Westerweel, J. (1997). Fundamentals of digital particle image velocimetry. *Meas. Sci. Technol.*, 8(12):1379.

Westerweel, J. and Scarano, F. (2005). Universal outlier detection for PIV data. *Exp. Fluids*, 39(6):1096–1100.

Whalley, R. D. and Choi, K.-S. (2011). Turbulent boundary-layer control with spanwise travelling waves. In *J. Phys. Conf. Ser.*, volume 318. IOP Publishing.

Whalley, R. D. and Choi, K.-S. (2012). The starting vortex in quiescent air induced by dielectric-barrier-discharge plasma. *J. Fluid Mech.*, 703:192–203.

Widmann, A. and Tropea, C. (2015). Parameters influencing vortex growth and detachment on unsteady aerodynamic profiles. *J. Fluid Mech.*, 773:432–459.

Williams, D. R., An, X., Iliev, S., King, R., and Reißner, F. (2015). Dynamic hysteresis control of lift on a pitching wing. *Exp. Fluids*, 56(5):1–12.

Winkelman, A. E. and Barlow, J. B. (1980). Flowfield model for a rectangular planform wing beyond stall. *AIAA J.*, 18(8):1006–1008.

Winter, H. (1936). Flow phenomena on plates and airfoils of short span. *NACA-TM-798*.

Wu, X., Zhang, X., Tian, X., Li, X., and Lu, W. (2020). A review on fluid dynamics of flapping foils. *Ocean Eng.*, 195:106712.

Yilmaz, T. O. and Rockwell, D. (2012). Flow structure on finite-span wings due to pitch-up motion. *J. Fluid Mech.*, 691:518–545.

Yu, H.-T. and Bernal, L. P. (2017). Effects of pivot location and reduced pitch rate on pitching rectangular flat plates. *AIAA J.*, 55(3):702–718.

Zhang, K., Hayostek, S., Amitay, M., He, W., Theofilis, V., and Taira, K. (2020). On the formation of three-dimensional separated flows over wings under tip effects. *J. Fluid Mech.*, 895.

Zhu, Q. (2011). Optimal frequency for flow energy harvesting of a flapping foil. *J. Fluid Mech.*, 675:495–517.

Zong, H., van Pelt, T., and Kotsonis, M. (2018). Airfoil flow separation control with plasma synthetic jets at moderate Reynolds number. *Exp. Fluids*, 59(11):1–19.

Appendix

Appendix A

Virtual instruments for equipment synchronisation and data acquisition

In order to achieve the control of the stepper motor, data acquisition and synchronisation among different measurement systems, some VIs are designed for the CompactRIO. Figure A.1 shows the program for the stepper motor control while the program of the data acquisition synchronised with the stepper motion is shown in Fig. A.2.

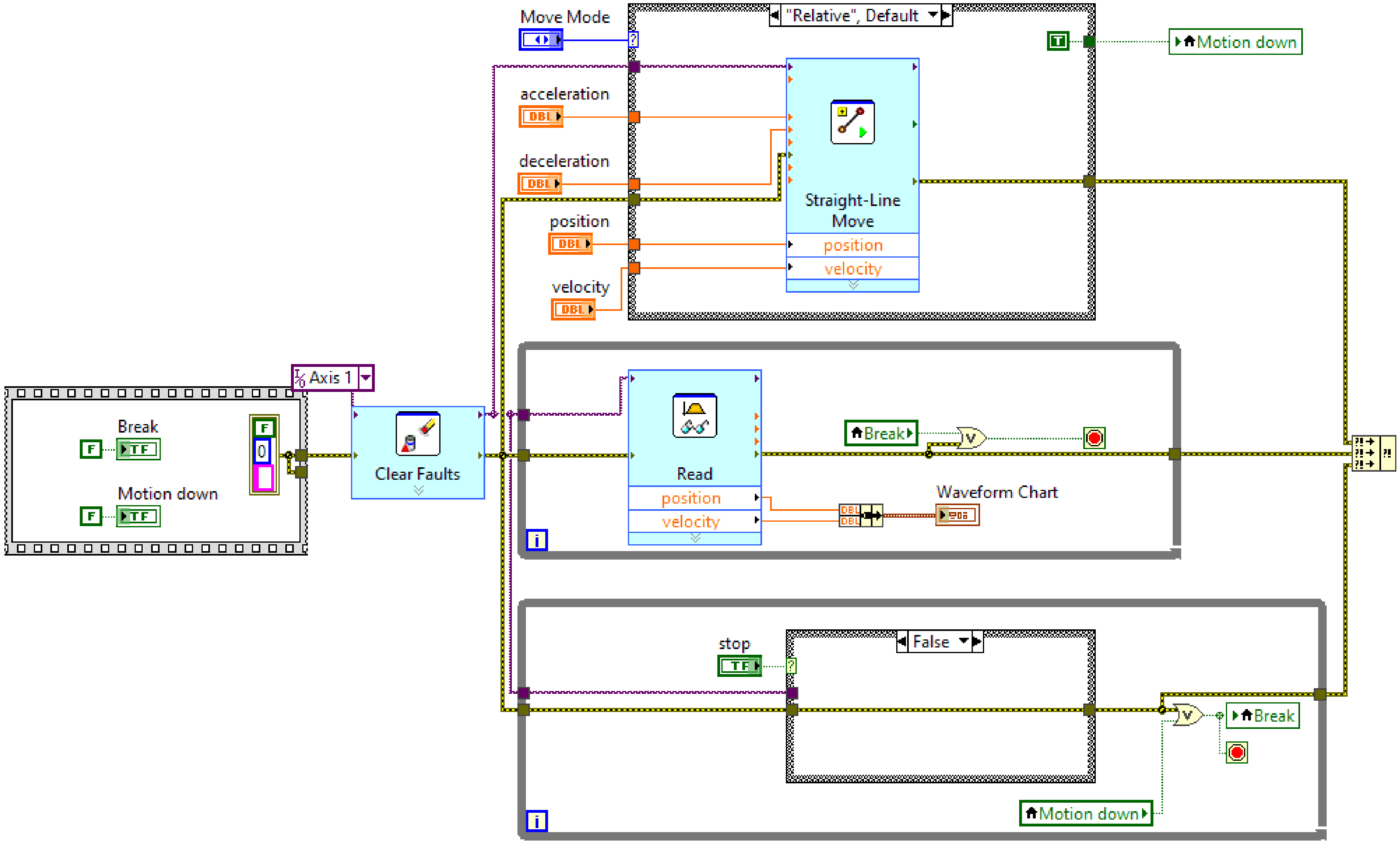

Figure A.1: Step control of the motor.

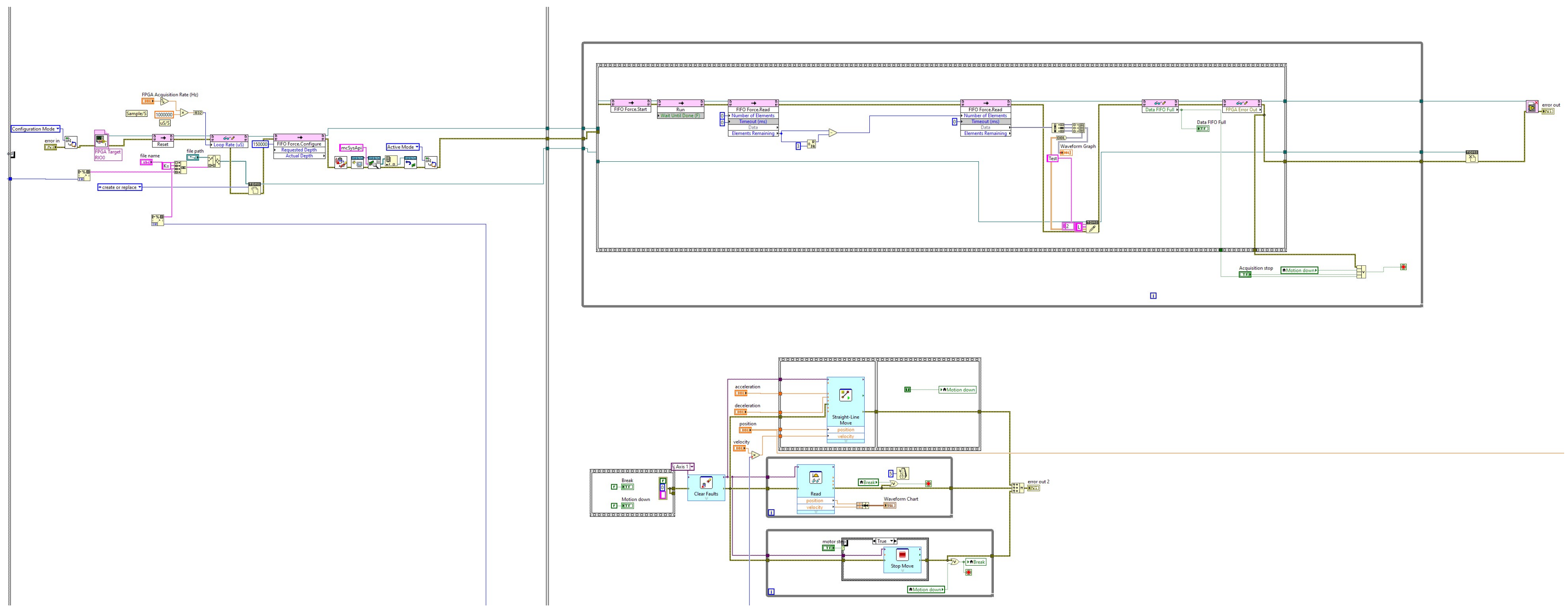

Figure A.2: Synchronisation of the stepper motor control and data acquisition.